

Dissertation
submitted to the
Combined Faculties of the Natural Sciences and Mathematics
of the
Ruperto-Carola University of Heidelberg, Germany
for the degree of
Doctor of Natural Sciences

Put forward by
Hemkumar Srinivas
born in Chennai(India)
Oral examination : 18 April 2023

XUV-IR pump-probe measurements on Argon, Krypton and
Nitrogen

Referees :

Priv.-Doz. Dr. Robert Moshammer

Priv.-Doz. Dr. Holger Kreckel

Zusammenfassung:

In dieser Arbeit wird die Photoionisationsdynamik von atomarem Krypton, Argon-Dimeren und molekularem Stickstoff werden in einer Reihe von Experimenten mit Attosekunden-Zeitauflösung untersucht. Die zeitliche Auflösung im Attosekundenbereich wird durch eine Messtechnik erreicht, bei der eine Reihe von extrem ultravioletten Impulsen verwendet. Diese Experimente wurden mit einer Attosekunden-Beamline mit hoher Wiederholrate (50 KHz, 75KHz, 150 KHz) und einem dreidimensionalen Ionen-/Elektronenimpuls-Abbildungsgerät, dem so genannten Reaktionsmikroskop (REMI), durchgeführt. Mit der hohen Wiederholrate Laser und den Koinzidenznachweisfähigkeiten des REMI wurden mehrere faszinierende Phänomene im Zusammenhang mit mit atomarer und molekularer Photoionisation verbunden sind, untersucht worden. Dazu gehören die Rolle von Spin-Orbit-Wechselwirkungen bei der Photoionisation von Atomen, der Einfluss von Van-der-Waals-Kräften auf die Photoionisation von Argondimeren und schließlich verschiedene Dissoziationsprozesse in molekularem Stickstoff.

Abstract:

In this work, the photoionization dynamics of atomic krypton, argon dimers and molecular nitrogen are investigated through a series of experiments with attosecond time resolution. The attosecond time resolution is provided by a measurement technique that uses a train of extreme-ultraviolet pulses. These experiments were performed with a high-repetition rate (50 KHz, 75KHz, 150 KHz) attosecond beamline and a 3-Dimensional Ion/electron momentum imaging device known as a Reaction Microscope (REMI). Using the high-repetition rate laser along with the coincidence detection capabilities of the REMI, several intriguing phenomena associated with atomic and molecular photoionization have been studied. These include the role of spin-orbit interactions in atomic photoionization, the influence of Van der Waals forces on the photoionization of argon dimers and finally various dissociation processes in molecular nitrogen.

List of Publications

Some of the work presented here is also a part of the following publication :

- Hemkumar Srinivas, Farshad Shobeiry, Divya Bharti, Thomas Pfeifer, Robert Moshammer, and Anne Harth - "High-repetition rate attosecond beamline for multi-particle coincidence experiments" Opt. Express 30, 13630-13646 (2022)

Additional Publications with own contributions:

- D Bharti, H Srinivas, F Shobeiry, K R Hamilton, R Moshammer, T Pfeifer, K Bartschat and A Harth - "Multi-sideband interference structures observed via high-order photon-induced continuum-continuum transitions in argon" - Phys. Rev. A 107, 022801
- Farshad Shobeiry, Patrick Fross, Hemkumar Srinivas, Thomas Pfeifer, Robert Moshammer, Anne Harth - " Sub-femtosecond optical control of entangled states" (arXiv:2110.06668) under review - Communications Physics (Nature journals group)
- S. Mandal, R. Gopal, H. Srinivas, A. D'Elia, A. Sen, S. Sen, R. Richter, M. Coreno, B. Bapat, M. Mudrich, V. Sharma and S. R. Krishnan - "Coincident angle-resolved state-selective photoelectron spectroscopy of acetylene molecules: a candidate system for timeresolved dynamics" - Faraday Discuss., 2021, 228, 242
- S. Mandal, R. Gopal, M. Shcherbinin, A. D'Elia, H. Srinivas, R. Richter, M. Coreno, B. Bapat, M. Mudrich, S. R. Krishnan and V. Sharma - "Penning spectroscopy and structure of acetylene oligomers in He nanodroplets" - Phys. Chem. Chem. Phys., 2020, 22, 10149

Contents

Introduction	7
1 Theoretical Background	9
1.1 Photoionization of atoms and generation of Extreme Ultraviolet (XUV) radiation	9
1.1.1 Photoionization at low intensities	10
1.1.2 Photoionization at high intensities	13
1.1.3 High-Harmonic Generation	15
1.1.4 Photoionization with XUV pulses	20
1.2 Photoionization of Diatomic molecules	21
1.2.1 The Born-Oppenheimer Approximation	21
1.2.2 Arrangement of electrons in diatomic molecules	23
1.2.3 Selection rules for the ionization of molecules	25
2 The RABBIT Technique	28
2.1 Sideband Oscillations	29
2.2 Attochirp, Wigner and Continuum-Continuum Delays	31
2.3 Phase Extraction	33
2.4 Attosecond Pulse Reconstruction	37
3 Experimental Details	40
3.1 The Laser	40
3.2 Interferometric Setup for Pump-Probe experiments	42
3.3 Reaction Microscope	44
3.3.1 Target	45
3.3.2 Spectrometer and Detector	45
3.3.3 Momentum Calculation	48
3.3.4 Acceptance and Resolution of the spectrometer	52
4 Interferometer Drift Stabilization	54
4.1 Setup	55
4.2 Stabilization Method	56
4.2.1 Tests with Drift Stabilization	60
4.3 RABBIT with Active Stabilization	63
4.3.1 Short Duration measurements	63
4.3.2 Long Duration Measurements	65

5	Angle-resolved RABBIT measurements on Krypton	68
5.1	Spin-Orbit splitting in XUV ionization of Krypton	68
5.2	RABBIT measurements on Krypton	69
5.2.1	Experiment and Data Analysis	69
5.3	Angle-averaged Results	72
5.4	Angle-resolved time delays in Krypton	75
5.4.1	Analysis of β parameters	76
5.4.2	Angle dependent spin-orbit delays	79
6	RABBIT measurements on Argon dimers	82
6.1	Formation of dimers	82
6.2	Direct Ionization of dimers	83
6.2.1	Comparing photoelectron spectra	84
6.2.2	Comparing photoionization delays	85
6.3	Dissociation of Dimers	90
7	XUV-IR measurements on Nitrogen	97
7.1	Ionization of Nitrogen by XUV	97
7.1.1	Direct ionization	99
7.1.2	Dissociation	101
7.2	Ionization of Nitrogen by XUV+IR	105
	Conclusion and Outlook	113
A	Beta parameter estimation	115
B	Ellipse Fit test data	117
C	Atomic Units	119
D	Lists	120
D.1	List of Figures	120
E	Bibliography	128

Introduction

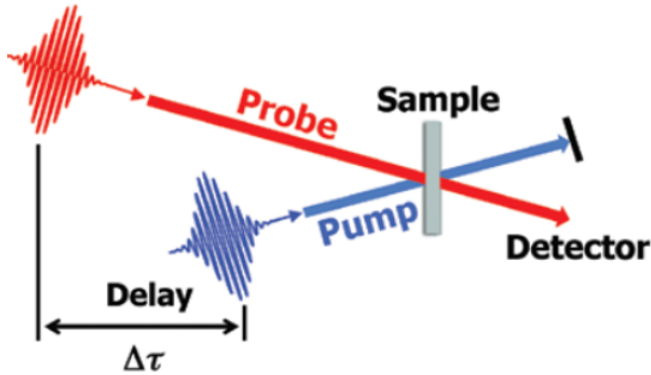
Till 19th Century, light was conveniently understood as "corpuscles" using Isaac Newton's formalism. Later, after significant contributions by Thomas Young (through his famous Double-Slit Experiment), Christian Huygens and the formulation thereafter by Maxwell, there was a clearer understanding of the wave nature of light. Moving forward a couple of decades, Max-Planck came up with the concept of quantization of light and revolutionized the understanding of light. Then came by Albert Einstein with his work on the photoelectric effect [1] and what subsequently followed was the birth of Quantum mechanics.

The birth of quantum mechanics not only resulted in a drastically different way of looking at the microcosmos, it also led to two inventions which would drastically change the course of human history - the **transistor** and the **LASER**. These two inventions together put humanity on a fast track.

From transistors come modern computers, which in turn accelerates the development of other technology. The lasers too have evolved by leaps and bounds over the years and have become increasingly important in the production of ever smaller transistors. As processors inside computers are getting smaller and smaller, it is inevitable that individual atoms will have to be used as transistors used in the future. Naturally, this makes it extremely important to have a complete understanding of processes occurring inside atoms and molecules.

One of the main challenges to observe and understand the details of atomic and molecular processes is their timescale. Molecular dynamics such as vibrations happen on the femtosecond timescale (10^{-15} seconds) while electronic motion in atoms is in the attosecond timescale (10^{-18} seconds). To be able to observe these processes in real-time, we need a "camera" which has a shutter speed to match the timescale of these motions. Till date, no camera has been able to reach these speeds.

However, about thirty years ago, lasers which produced pulses less than a picosecond (10^{-12} seconds) lead to a Nobel-prize winning experiment by Ahmed Zewail[2]. The ultrashort laser pulses were used like a camera to capture molecular dynamics in real time. The technique utilized in this experiment is famously known as the "Pump-Probe" method, where the two laser pulses at precise intervals of time can be used to make a movie of atomic or molecular processes. Almost all pump-probe measurements use the phenomenon of interference of two coherent waves, in one way or the other.



Schematic of a pump-probe measurement. Figure adapted from [3]

Over the last two decades, Extreme Ultraviolet (XUV) pulses lasting only a few tens of attoseconds have also made it possible to study some of the fundamental processes such as electronic motion in atoms and molecules[4]. For these measurements too, the pump-probe technique is utilized where XUV pulses act as the "Pump" and ionize the atom or molecule, followed by "Probe" infrared pulses which last only a few femtoseconds, map the phase of the outgoing electron wavepacket.

All the experiments presented here are based on such pump-probe measurements with XUV and IR pulses. For these experiments, a novel laser system that produced infrared pulses lasting only 40 femtoseconds and with high-repetition rates (50, 75 and 150 KHz) was successfully used to generate XUV photons with energies upto 40 eV. The XUV source was then combined to a spectrometer that provides 3 dimensional momentum information for electrons as well as ions. To perform pump-probe experiments, a Mach-Zehnder interferometer[5] combining the XUV source was used.

The contents of this thesis are organized as follows: theoretical concepts that are necessary to understand all the experimental results are discussed in the beginning. Following this, the RABBIT technique, which is an XUV-IR pump-probe technique is discussed. The experimental details are presented after this. After this, the results of measurements on Krypton atoms, Argon dimers and Nitrogen molecules will be covered. The measurements on Krypton were performed to study the role of spin-orbit interaction in photoionization, while the measurement on argon dimers was done to look for the role of Van der Waals interactions in photoionization. The measurements on nitrogen were aimed at observing the various dissociation pathways.

1 Theoretical Background

In this chapter, all the theoretical concepts essential to understand the experimental results will be discussed. It begins with an overview of the atomic photoionization after which there is a brief explanation of the method that is used to generate Extreme Ultraviolet radiation. Following this, the fundamentals of molecular photoionization is also covered.

1.1 Photoionization of atoms and generation of Extreme Ultraviolet (XUV) radiation

The concept of photoionization is a very simple one. To remove an electron out of a neutral atom, the energy needs to be supplied externally. The energy required to remove an electron from the ground state of a neutral atom is called the ionization threshold. When photons having energy greater than the ionization threshold strike an atom, an electron is ejected and a positively charged ion is left behind. This process is called photoionization.

Photoionization is one of the most direct ways to study the structure of an atom or molecule. Through photoionization measurements, the electronic energy levels can be measured. This technique has been used for more than half a century to study the structure and dynamics of electrons inside atoms and molecules. Electromagnetic radiation in the extreme ultraviolet(XUV) to soft X-rays are commonly used to study photoionization. The threshold for valence electrons are typically between 10 to 25 eV for atoms, while energies of several 100 eVs are needed to remove the inner shell electrons. The required XUV and X-ray radiation can be obtained from table-top sources through High-Harmonic Generation(HHG)[6] as well as synchrotrons[7] all around the world.

The intensity of the electromagnetic radiation influences the pathway of ionization. At intensities of less than 10^{12} W/cm², the atom or molecule ionizes upon absorbing only one photon. At higher intensities, the atom can absorb multiple photons for ionization. This is typically observed with high intensity light sources such as femtosecond lasers and Free-Electron lasers[8].

Since photoionization is at the heart of the work presented here, this chapter covers the theoretical concepts related to photoionization both at low and high intensities. Following this will be a brief explanation of the nonlinear process of High-Harmonic generation and how the ionization of atoms with XUV looks like in an experiment.

1.1.1 Photoionization at low intensities

The interaction of light with atoms usually requires using a rigorous formalism using quantum electro dynamics (QED). In this method, the field is quantized, as photons with frequency ν . However, considering the photon energy ($h\nu$) being used in the photoionization experiments presented here, even for modest intensities ($\leq 10^{10} \text{ W/cm}^2$), the number of photons is so large that it can be treated as a continuous variable. This means that the field is considered to be an electromagnetic wave obeying Maxwell's equations. The result of this is a semi-classical formalism where the electric field is treated classically and the atomic system is looked at from a quantum mechanical perspective. The mathematical treatment presented here is therefore a brief summary of the semi-classical treatment presented in Ref.[9]. The reader is directed to this reference for a detailed explanation.

We begin by considering the electric field \vec{E} and the magnetic field \vec{B} , which satisfy Maxwell's equations. The scalar and vector potentials ϕ and \vec{A} corresponding to these fields are then given by :

$$\vec{E}(\vec{r}, t) = -\nabla\phi - \frac{1}{c}\frac{\partial\vec{A}}{\partial t} \quad (1.1)$$

$$\vec{B}(\vec{r}, t) = \nabla \times \vec{A} \quad (1.2)$$

where \vec{r} is the position vector and t is time. Since these definitions of the fields are invariant to gauge transformations, a variety of different potentials can be used to describe the same field. In order to simplify the analysis, the Coulomb gauge is chosen, where :

$$\vec{\nabla} \cdot \vec{A} = 0 \quad (1.3)$$

Upon taking $\phi = 0$ since there are no potential sources, the vector potential \vec{A} satisfies the wave equation and can be expressed as a monochromatic plane wave with frequency ω :

$$\vec{A}(\vec{r}, t) = A_0(\omega)\hat{\epsilon}\cos(\vec{k} \cdot \vec{r} - \omega t + \delta_w) \quad (1.4)$$

The quantities \vec{k} , $\hat{\epsilon}$ and δ_w are the wave vector, polarization vector and constant phase respectively and \vec{A} is therefore the form of the electric field that would interact with a charged particle.

For a charged particle with mass m and charge q interacting with the electromagnetic field, the Hamiltonian can be written as :

$$H = \frac{1}{2}\left(\vec{p} + \frac{\vec{A}}{c}\right)^2 + \phi \quad (1.5)$$

Expanding this expression and using the Hermitian nature of the Hamiltonian H results in :

$$H = \frac{\vec{p}^2}{2m} - \frac{q}{2m}(\vec{A} \cdot \vec{p} + \vec{p} \cdot \vec{A}) + \frac{q^2}{2m}\vec{A}^2 + q\phi \quad (1.6)$$

Subsituting for $\vec{p} = -i\hbar\nabla$, the time dependent Schrödinger equation can be written as :

$$i\hbar \frac{\partial}{\partial t} \Psi(\vec{r}, t) = \left[\frac{-\hbar^2}{2m} \nabla^2 + i\hbar \frac{q}{2m} (\vec{A} \cdot \vec{\nabla} + \vec{\nabla} \cdot \vec{A}) + \frac{q^2}{2m} \vec{A}^2 + q\phi \right] \Psi(\vec{r}, t)$$

With the Coulomb gauge, $\nabla \cdot (\vec{A}\Psi) = \vec{A} \cdot (\nabla\Psi) + (\nabla \cdot \vec{A})\Psi = \vec{A} \cdot (\nabla\Psi)$ and hence the above equation can be rewritten as :

$$i\hbar \frac{\partial}{\partial t} \Psi(\vec{r}, t) = \left[\frac{-\hbar^2}{2m} \nabla^2 + i\hbar \frac{q}{m} (\vec{A} \cdot \vec{\nabla}) + \frac{q^2}{2m} \vec{A}^2 + q\phi \right] \Psi(\vec{r}, t)$$

In a hydrogenic system, the electrostatic Coulomb potential between the electron and nucleus is given by $\frac{-Ze^2}{4\pi\epsilon_0 r}$. The Hamiltonian then can be expressed as :

$$H(t) = \frac{-\hbar^2}{2m} \nabla^2 - \frac{Ze^2}{(4\pi\epsilon_0)r} - i\hbar \frac{e}{m} \vec{A} \cdot \nabla + \frac{e^2}{2m} \vec{A}^2 \quad (1.9)$$

The Hamiltonian can thus be expressed as $H = H_0 + H_{int}(t)$, where

$$H_0 = \frac{-\hbar^2}{2m} \nabla^2 - \frac{Ze^2}{(4\pi\epsilon_0)r} \quad (1.10)$$

is the time-independent part and

$$H_{int}(t) = -i\hbar \frac{e}{m} \vec{A} \cdot \nabla + \frac{e^2}{2m} \vec{A}^2 \quad (1.11)$$

describes the interaction of the atom with the field. In the scenario where there is only single ionization taking place, the electromagnetic field is very weak and \vec{A}^2 is negligible. Hence the interaction term of the Hamiltonian can be considered as a small perturbation to the system, given by $H'(t) = -i\hbar \frac{e}{m} \vec{A} \cdot \nabla$.

The perturbation on the atom by an electromagnetic field can result in processes such as photoionization and stimulated emission. Thus, from perturbation theory, a lot of meaningful information about the light-atom interaction can be extracted, particularly with the calculation of transition probabilities for various states. To do this, we begin with the solution to the Schrödinger equation. The normalized general solution is given by:

$$\Psi = \sum_k c_k(t) \psi_k(\vec{r}) e^{-iE_k t/\hbar} \quad (1.12)$$

When the atom is perturbed by an external electromagnetic field, the system transitions from an initial state Ψ_i to a final state Ψ_f . In other words,

$$H'_{fi}(t) = \langle \psi_f | H'(t) | \psi_i \rangle \quad (1.13)$$

This transition is possible only when $\hbar\omega_{fi} = (E_f - E_i)$, E_f and E_i are the energies of the final and initial states respectively. From this, we can define the transition matrix to be :

$$M_{fi} = \langle \psi_f | \vec{A} \cdot \vec{\nabla} | \psi_i \rangle = \langle \psi_f | e^{i\vec{k} \cdot \vec{r}} \hat{\epsilon} \cdot \nabla | \psi_i \rangle = \int \psi_f(\vec{r}) e^{i\vec{k} \cdot \vec{r}} \hat{\epsilon} \cdot \nabla \psi_i(\vec{r}) d\vec{r} \quad (1.14)$$

The expression for the transition matrix can be simplified by expanding the exponential term through a Taylor series expansion, given by:

$$e^{i\vec{k} \cdot \vec{r}} = 1 + i(\vec{k} \cdot \vec{r}) + \frac{1}{2!}(i\vec{k} \cdot \vec{r})^2 + \dots \quad (1.15)$$

For most photoionization experiments, the incident field has a wavelength in the order of a few 100 nanometers or even less. This would mean that $kr \ll 1\text{\AA}$. Therefore, the exponential term can be approximated as $\exp(i\vec{k} \cdot \vec{r}) \approx 1$ and this is known as the dipole approximation. With this, we have:

$$\mathbf{M}_{fi} = \hat{\epsilon} \cdot \langle \psi_f | \nabla | \psi_i \rangle = \hat{\epsilon} \cdot \frac{im}{\hbar} \langle \psi_f | \dot{\vec{r}} | \psi_i \rangle \quad (1.16)$$

With the Heisenberg equation of motion, this can be rewritten as $\langle \psi_f | \dot{\vec{r}} | \psi_i \rangle = \frac{1}{i\hbar} (E_i - E_f) \langle \psi_f | \vec{r} | \psi_i \rangle$ and using $\vec{r}_{fi} = \langle \Psi_f | \vec{r} | \Psi_i \rangle$, we arrive at the final expression

$$M_{fi} = \frac{-m\omega_{fi}}{\hbar} \hat{\epsilon} \cdot \vec{r}_{fi} \quad (1.17)$$

At this juncture, it is appropriate to introduce the Dipole operator, given by : $\vec{D} = -e\vec{r}$, with its matrix element $D_{fi} = -er_{fi}$ and the above equation can be expressed alternatively as :

$$M_{fi} = \frac{m\omega_{fi}}{\hbar e} \hat{\epsilon} \cdot \vec{D}_{fi} \quad (1.18)$$

From the product $\hat{\epsilon} \cdot \vec{D}_{fi}$, it can be determined if a transition is electric dipole allowed or forbidden. A non-vanishing D_{fi} would mean an allowed transition, while the matrix elements become zero for those perpendicular to the polarization axis and are hence forbidden. Thus, Eq. 1.18 is one of the most important quantities calculated to understand light-atom interactions, particularly direct photoionization at low field intensities. At higher field intensities, the higher terms in the series expansion in eq. 1.15 begin to have non-vanishing contributions and hence results in additional transitions which are dipole forbidden. Hence there are two other ionization methods at higher intensities, namely: above-threshold/multiphoton ionization and tunneling ionization. These would be discussed in the following section.

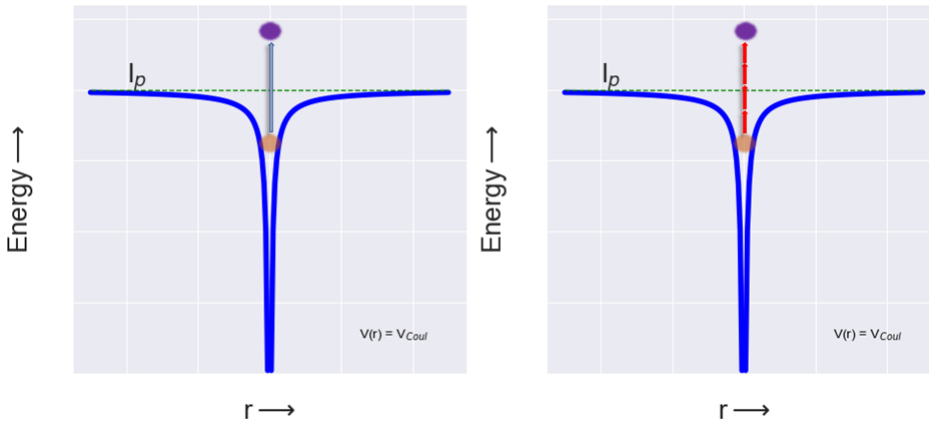


Figure 1.1: Left : Schematic of the removal of a valence electron by absorbing a single XUV photon, Right: Schematic of Multi-Photon Ionization, by absorption of multiple IR photons

1.1.2 Photoionization at high intensities

Modern light sources such as femtosecond lasers and X-Ray Free electron lasers have made it possible to reach extremely high field intensities. With the help of these sources, intensities of 10^{16} W/cm^2 or even higher are routinely achieved. Even as field intensities of about 10^{12} W/cm^2 are reached, there are additional ionization pathways that are possible. A mathematical treatment of ionization at high intensities would require going beyond the perturbation theory approach and using the strong-field approximation (SFA)[10, 11]. A discussion of the SFA is beyond the scope of this work and is discussed in detail in reference [12]. However, the processes can be explained in a simplified manner as follows. The first pathway that is possible already at intensities between 10^{12} W/cm^2 to 10^{14} W/cm^2 is called Multi-Photon ionization[13]. In this, when a high number of photons are available, the atom absorbs multiple photons, so that the electron transitions from a valence state to a continuum state. This happens by absorbing one photon at a time and passing through virtual states which are extremely short lived. When the atom absorbs more photons than necessary for photoionization it results in above-threshold ionization (ATI)[14].

The photoelectron kinetic energy spectrum for such a process exhibits peaks (see Fig. 1.2) which are separated by an energy corresponding to the frequency of the driving field ($E_e = n\omega - I_p$). The matrix elements for this transition is calculated by using the Lowest order peturbation theory and the ionization probability scales with the intensity as $M_{fi} \propto I^n$. So, as the intensity increases, the more the number of photons absorbed resulting in ATI peaks in the electron spectrum. At intensities of 10^{14} W/cm^2 or higher, a very interesting phenomenon occurs. The electric field strength in this case is comparable to the Coulomb potential of an atom. This effectively means that the Coulomb potential of the atom can be deformed in the

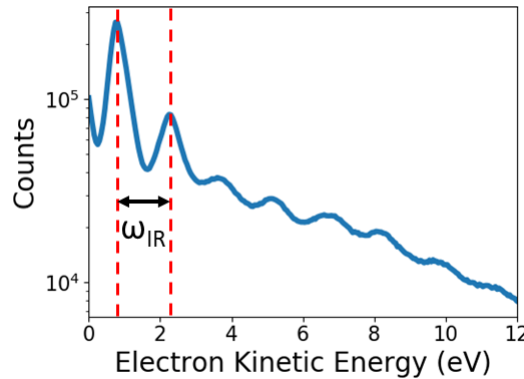


Figure 1.2: Experimentally measured ATI Photoelectron spectrum obtained by ionizing Argon with femtosecond IR pulses

presence of a strong field and this results in tunneling of the valence electron through the barrier. This process is also called Tunnel ionization.

It is pertinent to introduce a term associated with strong-field ionization over here. This is called the ponderomotive energy (U_p), which is the energy acquired from an oscillating field by an electron that becomes "free" after tunneling. It is expressed as:

$$U_p = \frac{I}{4\omega^2} \quad (1.19)$$

where I and ω are the intensity and frequency of the field respectively.

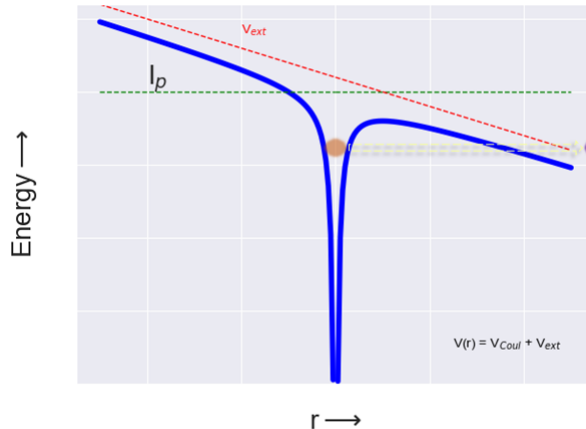


Figure 1.3: Schematic of tunnel ionization

Since both multiphoton ionization and tunneling ionization are possible at high intensities, it is very useful to introduce a parameter to determine the mode of ionization at a given intensity. The Keldysh parameter[15, 16] helps us determine

which will be the dominant mode of ionization and is defined by :

$$\gamma = \sqrt{\frac{I_P}{2U_P}} \quad (1.20)$$

With the help of the Keldysh parameter, the most likely ionization pathway can be determined. Tunneling occurs when $\gamma < 1$, while multiphoton ionization happens when $\gamma \gg 1$, at relatively lower intensities. Both multi-photon ionization and tunneling ionization reveal intriguing aspects of the atomic potential and have been the central subject of several experiments performed with femtosecond lasers over the last two decades.

The phenomenon of tunnel ionization in particular is the starting point of High-Harmonic generation, which is used to generate XUV light from IR femtosecond pulses. This will be explained in the next section.

1.1.3 High-Harmonic Generation

The three-step model

The nonlinear process of HHG, that produces XUV radiation can be understood with the help of a simple Three-Step model[6] (Fig. 1.4). During the first step, the electron tunnels out of the barrier, since the barrier is suppressed by the external laser field. The second step involves the acceleration of the quasi-free electron by the field. The acceleration continues until the field changes direction. When the field changes direction due to its periodic nature, the electron is accelerated once again in the reverse direction. In the third step, the electron recollides with the parent ion after the acceleration. When it does, it emits the excess energy in the form of XUV photons.

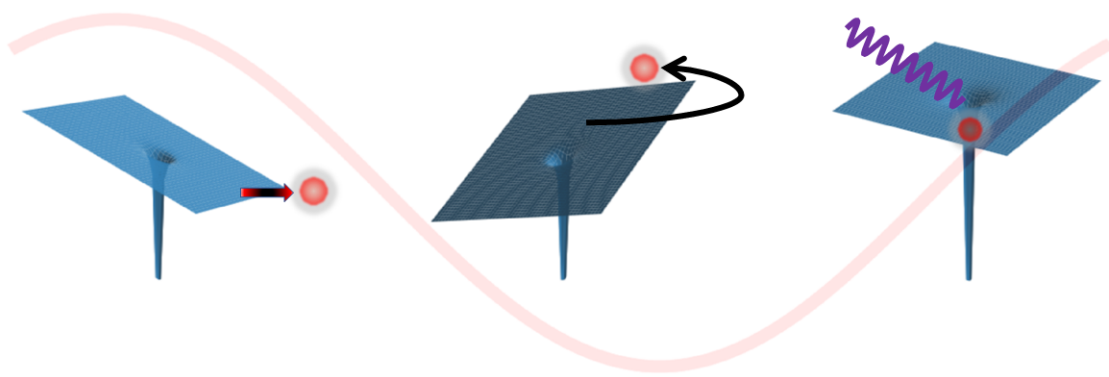


Figure 1.4: Schematic of the Three-Step model for high-harmonic generation. The three steps are: tunneling, acceleration and recollision

This process repeats every half cycle of the oscillating external field. Depending on when the electron was released with respect to the phase of the external field,

the electrons take many possible trajectories and thereby the XUV photons could have a wide range of energies. Since the entire cycle from tunnelling to recollision is periodic and occurs every half cycle, the emitted XUV spectrum also exhibits a periodic structure, in the form of a frequency comb. The spacing between each peak in the frequency comb is twice the frequency of the driving field. When an inverse Fourier transform of the XUV spectrum is performed, in the time domain this results in a train of pulses. Likewise, with few-cycle broadband IR pulses, isolated attosecond pulses can be obtained[17, 18].

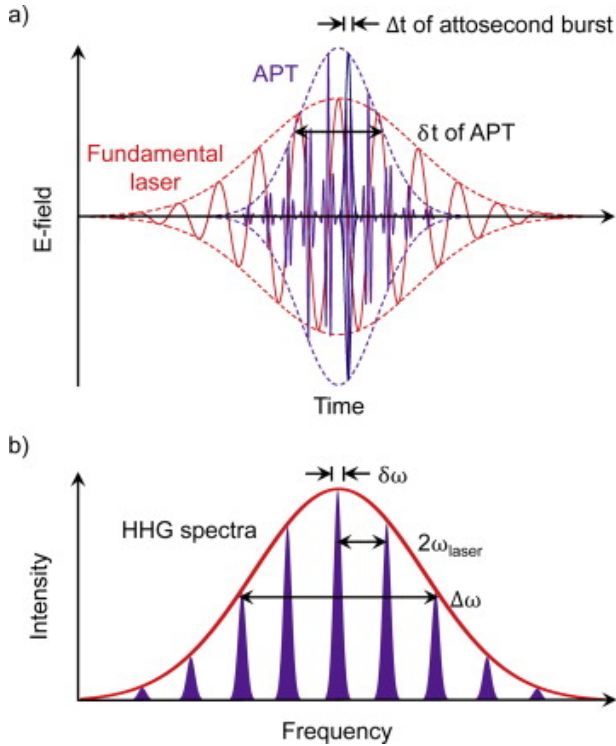


Figure 1.5: Top: A Train of attosecond pulses produced in the time domain by a long IR pulse. Bottom : XUV Frequency comb obtained from the Fourier transform of an attosecond pulse train. Figure taken from [19]

In order to generate XUV through HHG, IR laser pulses lasting few tens of femtoseconds are usually used. Since the laser field is of finite duration, the XUV pulses produced also are finite and are in the form of a bunch of pulses. Each of these pulses in the bunch last typically a few hundred attoseconds. The envelope of the IR pulse affects the envelope of the XUV burst. In the ideal scenario, a femtosecond IR laser has a Gaussian envelope, with no chirp. The ideal attosecond pulse train then will also have a gaussian envelope and the duration of each pulse in the train is only determined by the bandwidth of the IR pulses. There is also no variation of the spectral phase for the various harmonics.

The three-step model relies on a semi-classical treatment of the interaction of the laser with the atom. The acceleration of the electron after tunneling is calcu-

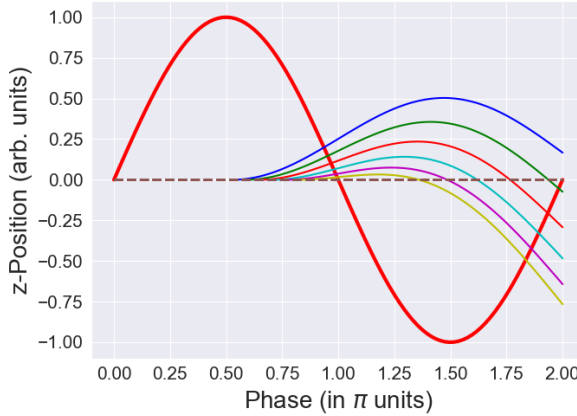


Figure 1.6: Classical trajectories for the electron in an oscillating field, calculated using eq. 1.21

lated by using the classical equations of motion. By calculating the trajectories of the electron motion, the maximum photon energy achievable through HHG in an atom at a given laser intensity can be estimated. The details of this calculation can be found elsewhere in reference [16]. This calculation can be summarized as follows: Since the motion of the electron is much faster than the rate at which the field changes, the laser field can be considered to be a monochromatic oscillating electric field $\vec{E} = E_0 \cos(\omega t)$ propagating along the z-axis, with an amplitude E_0 and frequency ω and time t . Let the electron escape the barrier at an instant t_i . The one dimensional trajectory for the electron would be :

$$z(t) = \frac{eE_0}{m_e\omega^2} [\sin(\omega t) - \sin(\omega t_i) - \omega(t - t_i)\cos(\omega t_i)] \quad (1.21)$$

where e is the charge of the electron and m_e is the mass of the electron. The kinetic energy can be further calculated by $E_e = \frac{m_e|v(t)|^2}{2}$, where v is the velocity of the electron. Obtaining the expression for velocity from eq. 1.21 and using eq. 1.19, the electron kinetic energy can be expressed in terms of ponderomotive energy as:

$$E_e = 2U_p[\cos(\omega t) - \cos(\omega t_i)]^2 \quad (1.22)$$

By calculating the trajectories from eq. 1.21, it can be seen that only those electrons that are released at a phase of $\frac{\pi}{4}(0.25 T_{cycle})$ and $\frac{\pi}{2}(0.5 T_{cycle})$ radians of the field, have a chance of recombining with the parent ion at a zero crossing (Fig. 1.6). The maximum energy is emitted by the electrons that are emitted at $t_i = 0.299T_{cycle}$ [20, 21]. The maximum electron kinetic energy reached is $3.17U_p$. The final energy of the harmonics is a sum of the ionization potential of the atom

and the kinetic energy acquired due to acceleration by the driving field. The highest energy achieved therefore through HHG, also called the cutoff energy is given by:

$$E_{cutoff} = 3.17U_p + I_p \quad (1.23)$$

A high cutoff energy for the harmonics can be achieved through two ways. One is to use a gas with a very high ionization threshold such as Helium or Neon. Another is to increase the ponderomotive energy by either increasing the laser intensity through tight focusing or by using extremely short pulses or by increasing the driving wavelength of the laser. In the recent years, advances in laser technologies, particularly in the mid-infrared range have made it possible to easily reach photon energies of 100 eV and more, reaching well into the soft X-Ray region[22]. HHG sources in combination with a monochromator arrangement[23, 24] have also been used in the recent years to replicate some of the synchrotron measurements on a table-top scale.

Real-world HHG

The three step model explains the process of generating high order harmonics from interaction of a single atom with an intense laser pulse. However, in a real experimental setup, an ensemble of atoms in the form of either a gas jet/cell or solid targets are used. The XUV produced therefore depends on a few ensemble effects.

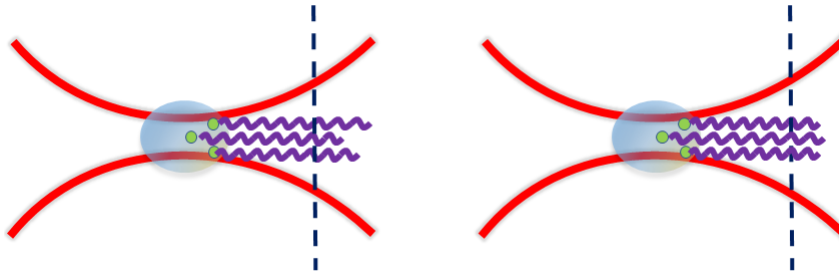


Figure 1.7: A visualization of the XUV emission at the focus of an intense laser beam. Left : Improper phase matching ($\Delta K \neq 0$) of the XUV from single atom emitters, Right : Optimal phase matching ($\Delta K = 0$) between the various XUV photons emitted from each atomic emitter.

If we consider the XUV emission from multiple atomic emitters, the maximum XUV intensity is achieved when there is perfect constructive interference due to a coherent addition of the XUV fields. This condition is also commonly called *phase matching*. However, due to a variety of factors, when atoms in an ensemble are driven by an IR pulse they do not exhibit a perfect degree of phase matching. To quantify the level of phase matching, it is useful to define a parameter $\Delta K =$

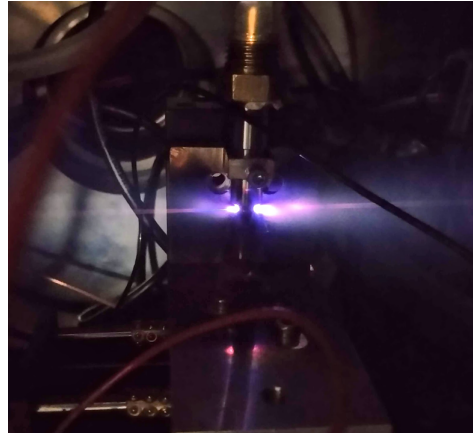


Figure 1.8: A photograph of the plasma created while generating XUV by focusing femtosecond IR pulses onto a gas cell.

$nK_{ir} - K_n$ [25, 26], where K_{ir} is the wavevector of the driving laser field and K_n is the wavevector of the n^{th} harmonic. If ΔK is zero, then a perfect phase matching condition is achieved. However, ΔK is non-zero, there is a phase mismatch and this results in only a weak XUV spectrum. There are four key factors that cause this mismatch and thus ΔK can be alternatively expressed as :

$$\Delta K = \Delta K_{gouy} + \Delta K_{nd} + \Delta K_{pd} + \Delta K_{atom} \quad (1.24)$$

Each term can be understood as follows:

- ΔK_{gouy} - refers to the Gouy phase variation, as the laser beam passes through the focus[27]. As the beam travels through the focus, it undergoes a phase variation of π radians and hence the atomic emitters from the two ends of the focal volume can have significant differences in phase.
- ΔK_{nd} & ΔK_{pd} - are together the dispersion introduced by the neutral atoms in the ensemble and the plasma created as a consequence of the high field intensities
- ΔK_{atom} - refers to the atomic dipole phase mismatch caused by the movement of the electron in the laser field. The value of ΔK_{atom} changes from negative to positive, as the atoms move through the focus.

Generating XUV in a laboratory through HHG therefore involves a constant optimization of parameters such as pressure, focal length and even the profile of the laser beam. Tweaking these parameters can not only ensure that an optimal flux is achieved, but also an optimal spectrum. By using a combination of these parameters, it is also possible to selectively enhance the strength of one particular harmonic (see for example [28]). In combination with a monochromator arrangement, such a source can provide a spectral resolution and flux comparable to a synchrotron.

In order to obtain a stable XUV source, it is extremely important therefore to have a stable target density (eg. constant gas pressure), stable pulse energy and pulse duration for the driving laser and excellent beam pointing stability to prevent effects introduced by a shifting focus.

1.1.4 Photoionization with XUV pulses

The photoelectron spectrum obtained by ionizing atoms provides intriguing insights about the spectral content of the photons, apart from revealing important information associated with the electron energy levels. When monochromatic radiation ionizes an atom , the resulting photoelectron spectrum displays a distribution having a bandwidth which is a convolution of the instrument response and the bandwidth associated with the state. When a pulse lasting only a few femtoseconds or lesser is used, the bandwidth is large and this reflects in the width of the photoelectron spectrum as well. If a comb of frequencies is used to ionize an atom, the photoelectron spectrum exhibits a comb structure. The typical electron spectrum obtained through ionization by HHG has a comb structure and the strength of each peak is determined by the intensity of the respective harmonic and the ionization cross-section of the atom at that energy.

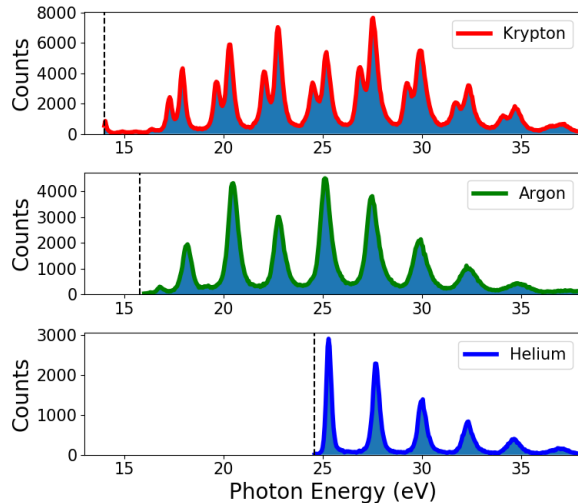


Figure 1.9: Experimentally measured electron spectrum obtained by the XUV ionization of noble gases. The double peak structure seen in Krypton is due to the spin-orbit splitting (discussed in Chapter 5). The dashed vertical lines indicate the respective ionization thresholds.

Fig. 1.9 shows the photoelectron spectrum obtained by ionizing krypton, argon and helium. By adding the ionization potential to the electron kinetic energy, it is possible to get a rough estimate of the cut-off energy of the harmonics and thereby the bandwidth of the harmonics. With additional information such as

the ionization cross section, filter transmission (if any filters are used to isolate a set of frequencies) and detection efficiency as a function of electron kinetic energy, it is possible to reconstruct the entire photon spectrum using the photoelectron spectrum (Fig. 1.10). This method gives information equivalent to that of a conventional XUV grating spectrometer, provided that the electron spectrometer's resolution is lesser than the bandwidth of each peak in the XUV frequency comb.

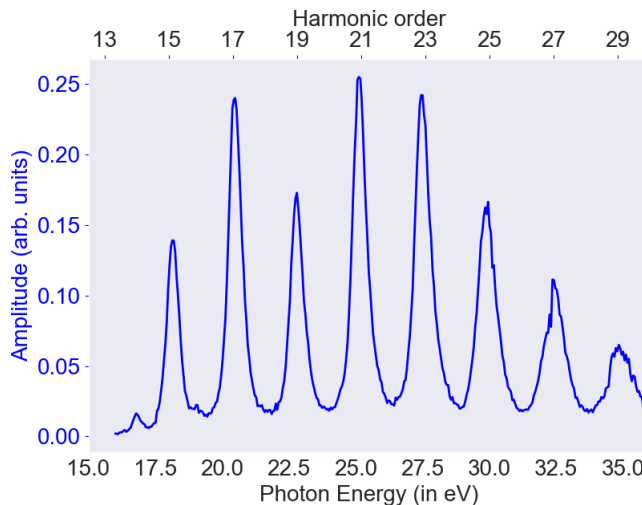


Figure 1.10: Reconstructed photon spectrum obtained from the photoelectron spectrum of Argon

1.2 Photoionization of Diatomic molecules

1.2.1 The Born-Oppenheimer Approximation

Diatom molecules are formed when two atoms share electrons through a covalent bond. A stable diatomic molecule is the next simplest unit of all matter after atoms. When atoms associate to form molecules, the inner valence electrons are unaffected and continue to be localized around the nucleus, just like in an individual atom. The valence electrons on the other hand are distributed throughout the molecule and provides the binding force. Since the molecule has two atoms bound together, there are additional degrees of freedom namely rotation and vibration, which are not present in atoms. A mathematical description of the molecular structure is therefore more complicated than that of individual atoms.

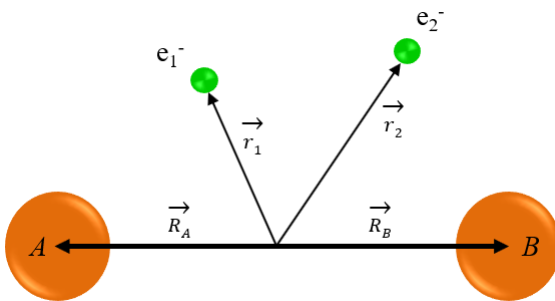


Figure 1.11: Coordinate system for a diatomic molecule

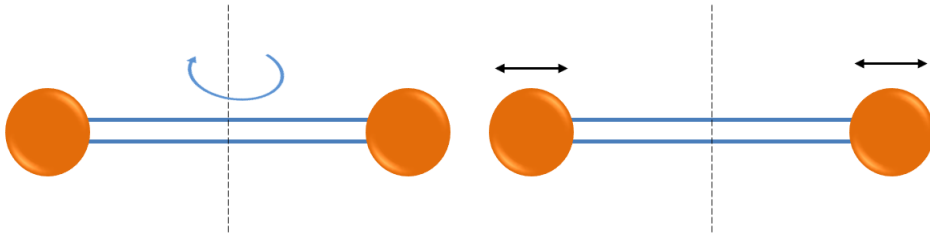


Figure 1.12: Visualization of the rotation and vibration degrees of freedom for a diatomic molecule

However, the problem can be greatly simplified by the fact that the mass of electrons is much smaller than the mass of nuclei. As a consequence, the timescales of electronic and nuclear motion are very different. This can be understood with the help of uncertainty principle. Consider the electron kinetic energy. It can be very simplistically expressed $E_e \approx \frac{\hbar^2}{m_e a^2}$, where a is the average internuclear distance and m_e electronic mass. Assuming $a \approx 1$ Angström, the kinetic energy is typically in the order of a few electron volts. Likewise, when we consider the molecular vibration, the molecular potential energy increases by a factor of $M_n \omega^2 a^2 / 2$, where M_n is the nuclear mass and ω is the oscillation frequency. The vibrational energy can be roughly expressed as $E_v = \sqrt{\frac{m_e}{M_n}} E_e$. Since the mass of the nucleus is typically 1000 times higher than that of an electron, the vibrational energies are much smaller. Since energy and time are inversely related through the uncertainty principle, the electron motion is about 100- 1000 times faster than nuclear motion.

Therefore, the nuclei can be considered to be stationary while considering the motion of electrons in a molecule. This is famously known as the *Born-Oppenheimer approximation*[29]. This approximation is extremely helpful in solving the Schrödinger equation for molecules, since it allows us to calculate the electron kinetic energies independent of the nuclear motion. This means that the total wavefunction $\Psi(\mathbf{R}_A, \mathbf{R}_B; r_1, r_2, \dots, r_N)$ of the diatomic molecule can be separated as a purely electronic wavefunction $\phi(r, \mathbf{R})$ and nuclear wavefunction $\psi(r; \mathbf{R})$. In other words,

$$\Psi(r_1, r_2, \dots, r_N, \mathbf{R}) = \phi(r_1, r_2, \dots, r_N; \mathbf{R})\psi(R) \quad (1.25)$$

Using this, the electronic wave equation can first be solved to obtain the electronic energies $E(R)$ at various internuclear distances R . The nuclear wave equation can then be solved in which the $E(R)$ acts a potential. When the $E(R)$ is plotted, we obtain what is called a *Potential Energy Curve* or PEC(Fig.1.13). With $R \rightarrow 0$, the potential is repulsive, while with $R \rightarrow \infty$, $E(R)$ tends to a constant energy, which is a sum of the energies of two isolated atoms. $E(R)$ also exhibits a minimum at a separation R_0 which is called the equilibrium distance. The amount of energy required to fragment a diatomic molecule is called the dissociation energy and is given by $D_e = E(\infty) - E(R_0)$. There are in addition, certain electronic configurations in a molecule which do not overlap and these are called the anti-bonding states, which too leads to the dissociation of a molecule.

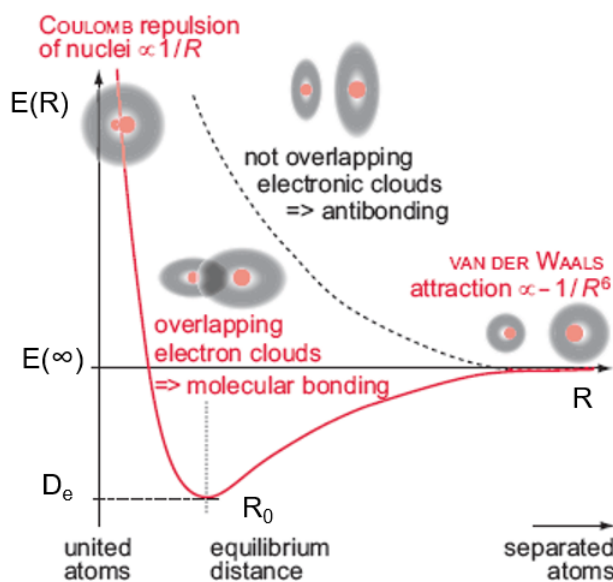


Figure 1.13: Schematic of a molecular potential as a function of internuclear distance. Figure adapted from [30]

1.2.2 Arrangement of electrons in diatomic molecules

In the case of atoms, there exists a spherical symmetry which is used extensively while calculating the electronic wavefunctions. With molecules however, this is not the case. The internuclear axis of a molecule fixes a reference direction for the molecule. If the internuclear axis is taken as the Z axis of the coordinate space, the Hamiltonian is invariant for rotations along this direction, while rotations are

not invariant along the X and Y axes. This is because, the operator for orbital angular momentum along the Z direction L_z commutes with the Hamiltonian, while the other components L_y, L_z and even \mathbf{L}^2 do not commute. Since the total orbital angular momentum \mathbf{L} operator does not commute with the Hamiltonian, the corresponding quantum number l is not a good quantum number. Therefore the electronic eigenfunctions in diatomic molecules are constructed as simultaneous eigenfunctions of electronic Hamiltonian H_e and L_z . This means

$$L_z\Phi = M_L \hbar \Phi, M_L = 0, \pm 1, \pm 2 \dots \quad (1.26)$$

$$L_z\Phi = \pm \Lambda \hbar \Phi, \Lambda = 0, 1, 2 \dots \quad (1.27)$$

where $\Lambda = |M_L|$ is the absolute value of the total electronic angular momentum's projection on the internuclear axis. In atomic spectroscopy, we have the notation **S,P,D,F** to denote the various total angular momentum values. Likewise, the notation for molecular spectroscopy uses letters from the Greek alphabet, given by:

$$\Lambda = 0, 1, 2, 3 \dots \rightarrow \Sigma, \Pi, \Delta, \Phi \dots \quad (1.28)$$

For individual electrons in molecules, the notation $\lambda = |m_l|$ is used. Similarly, the notation is given by:

$$\lambda = 0, 1, 2, 3 \dots \rightarrow \sigma, \pi, \delta, \phi \dots \quad (1.29)$$

For diatomic molecules, there is a center of symmetry at the midpoint of the internuclear axis, where the Hamiltonian is invariant under a reflection operation ($\mathbf{r}_i \rightarrow -\mathbf{r}_i$). The reflection operation also commutes with the L_z operator. Therefore, electronic wavefunctions can also be assigned a parity for a given Λ .

If the wavefunction changes its sign after reflection, it is said to have odd parity and is termed as an *ungerade* state, denoted by the letter *u*. On the other hand, if the wavefunction does not change its sign after reflection, the wavefunction is said to have even parity and is termed as a *gerade* state, denoted by the letter *g*. Furthermore, an additional label is given to distinguish the molecular wavefunction, as to whether it is a ground state or an excited state. This is done using the letters from the Roman alphabet X, A, B, C, D etc, to denote the ground state, first excited state, second excited state and so on. Therefore molecular states are denoted using the notation

$$X^{2S+1}\Lambda_{g,u} \quad (1.30)$$

where S refers to the total electronic spin.

1.2.3 Selection rules for the ionization of molecules

Since the XUV radiation used in all the experiments presented here, is of sufficiently low intensity ($< 10^9 \text{ W/cm}^2$), the ionization of molecules too can be analyzed under the framework of the dipole approximation. The dipole selection rules for molecular photoionization are however more complex and involves the use of Group theory[30]. Nonetheless, symmetry considerations greatly simplify the deduction of the selection rules. One key factor is that the transition probability is a scalar quantity and hence the dipole operator connecting the initial and final states should preserve the overall symmetry.

If the electric field inducing the transition is linearly polarized, then the dipole operator is given by $\mu z = -Ez$ and transitions can occur through two directions. One is along the polarization axis of the XUV pulse and the other is the internuclear axis. The molecules from a gas jet in the REMI are all isotropic and the molecular axis is randomly oriented with respect to the XUV polarization axis. If the transition dipole moment is aligned along the molecular axis, it is referred to as a *Parallel* transition. If the transition dipole moment is orthogonal to the internuclear axis, it is a *Perpendicular* transition.

For *Parallel* transitions, the selection rule is $\Delta\Lambda = 0$. The selection rule for *Perpendicular* transitions is $\Delta\Lambda = \pm 1$. For both transitions which involve only the electronic excitation by the XUV light, the inversion symmetry needs to change. Therefore, for excitation processes, transitions from an *ungerade* state are only allowed to a *gerade* state and vice versa. The detailed derivation of selection rules can be found in reference [31]. They are summarized in the table below for a quick reference.

	Σ_g^+	Σ_g^-	Σ_u^+	Σ_u^-	Π_g	Π_u	Δ_g	Δ_u
Σ_g^+	x	x		x	x	⊥	x	x
Σ_g^-		x		x	⊥	x		x
Σ_u^+		x	x	⊥	x	x		x
Σ_u^-			x	⊥	x	x		x
Π_g				x		x		⊥
Π_u					x	⊥	x	
Δ_g						x		
Δ_u							x	

Figure 1.14: Table of dipole transitions in homonuclear diatomic molecules. || and \perp show allowed parallel and perpendicular transitions, while x indicates forbidden transitions. Adapted from [32, 20]

Franck-Condon Principle

The above mentioned selection rules govern the transitions between various electronic states. The vibrational transitions are much slower and occur when the nuclei are stationary during an electronic transition. The vibrational transitions hence follow the *Franck-Condon Principle* [33, 34], which states that electronic transitions take place in a timescale that are very short compared to the time required for the nuclei to move significantly. The vibrational transitions can therefore be visualized by a vertical arrow at one fixed internuclear distance in the potential curves (Fig.1.15). The Franck-Condon principle greatly simplifies the identification of vibrational transitions. The transitions between the various vibrational levels do not occur with equal probability. Transitions having a large overlap of vibrational wavefunctions before and after the transitions are preferred over the rest. This fact is used to calculate the Franck-Condon coefficients, which further help to predict the vibrational spectra.

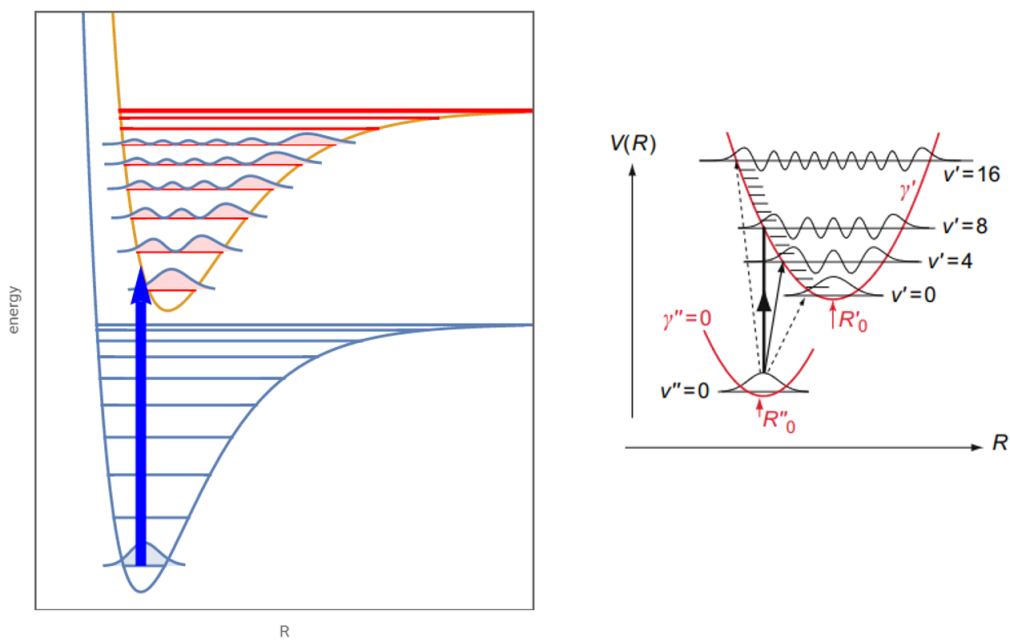


Figure 1.15: Left: Schematic of transitions between molecular vibrational levels, governed by the Franck-Condon principle. Figure adapted from [35]. Right : The bold line shows the strongest transition allowed by the Franck-Condon principle. Figure adapted from [30].

To better understand all that has been discussed so far, we take the example of an experimentally obtained photoelectron spectrum for the ionization of nitrogen (Fig. 1.16). The ground state of a neutral nitrogen molecule has a configuration of $X^1\Sigma_g^+$. The three lowest ionic states of nitrogen are the $X^2\Sigma_g^+$, $A^2\Pi_u^+$ and $B^2\Sigma_u^+$ states respectively and to reach these states, photons of energy greater than

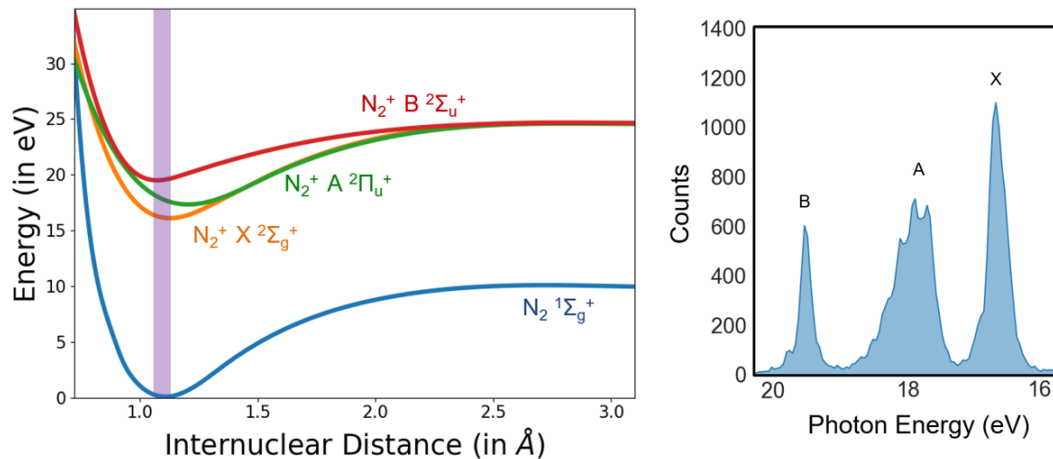


Figure 1.16: Left: Calculated potential energy curves for molecular nitrogen, with a vertical bar showing the Franck-Condon allowed region. Data for PECs taken from [36]. Right : Experimentally obtained photoelectron spectrum after ionizing N₂ by a XUV harmonic.

16 eV are required. In fig.1.16, the rectangular region shaded purple shows the area where there is maximum overlap between vibrational wavefunctions of the ground and ionic states. Hence, this is the Franck-Condon allowed region. Combining this information with the other selection rules, with sufficient XUV photon energy neutral nitrogen molecules can be ionized to reach the three ionic states X, A and B respectively. If only one harmonic in the XUV frequency comb ionizes the molecule, the resulting photoelectron spectrum then would feature three peaks, corresponding to each of the ionic states. The width of the distributions for each state is determined by the number of vibrational levels present and thereby the depth of the potential.

Having discussed briefly the fundamentals of photoionization in atoms and molecules, we will now move on to discuss the experimental setup that was used to perform all the measurements.

2 The RABBIT Technique

The ionization of atoms by XUV results in a series of peaks in the photoelectron spectrum, as discussed in section 1.1.4. An inverse Fourier transform of the XUV frequency comb into the time domain results in a train of pulses, each lasting a few hundred attoseconds. The pulses produced through HHG are some of the shortest man-made events and direct measurement methods for these pulses do not exist till date. To characterize such short pulses, typically an autocorrelation or a cross-correlation scheme is used. In an autocorrelation measurement[37, 38], two copies of a pulse are overlapped interferometrically and the intensity is measured as a function of delay between the two. The envelope of the resulting intensity distribution reveals the pulse duration. Autocorrelation is one of the easiest methods to measure the intensity profiles of pulses lasting picoseconds or shorter. Processing the signal in the frequency domain [39, 40, 41, 42] and combining it with reconstruction algorithms provides other key pulse parameters such as chirp and carrier-envelope phase.

In cross-correlation measurements, a previously characterised pulse is temporally overlapped with the pulse to be examined. Since the two different frequencies cannot interfere, usually a nonlinear effect such as photoionization is used to characterize the pulse. The photoelectron spectrum obtained through a cross-correlation between XUV and IR pulses is commonly used to determine the pulse duration of XUV and is also used to study photoionization in a time-resolved manner. These features make XUV-IR cross-correlation measurements an indispensable tool in attosecond physics.

Two most commonly used XUV-IR cross-correlation methods are RABBIT[43] and attosecond streaking [44]. The former is used to characterize a train of attosecond pulses while the latter is used to characterize isolated attosecond pulses. Although the theoretical framework dealing with both techniques are largely the same, the two have distinctive applications. RABBIT has a larger scope due to the better spectral resolution it offers in comparison to the streaking technique. A detailed comparison between the two methods can be found in reference [45]. In this chapter, the RABBIT technique will be discussed in detail, with details about the attosecond pulse reconstruction and the insights it provides into the dynamics of photoionization.

2.1 Sideband Oscillations

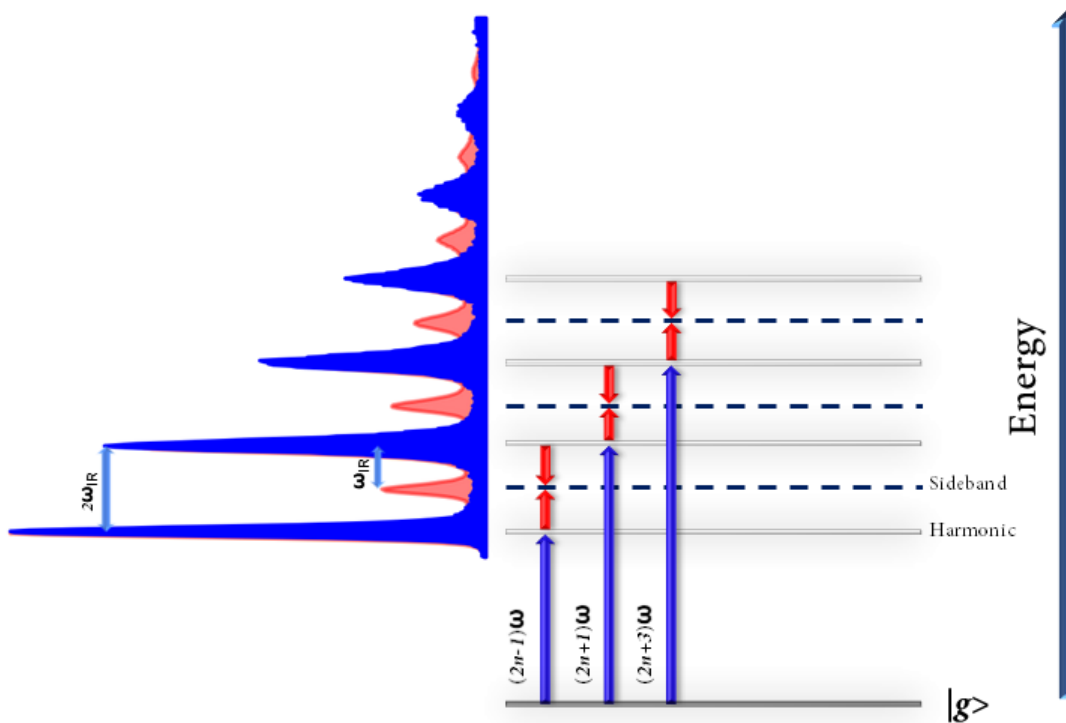


Figure 2.1: Schematic of the formation of sidebands and the corresponding photoelectron spectrum obtained from an experiment

The spacing between two peaks in the photoelectron spectrum obtained by the ionization of XUV is twice the photon energy of the IR pulse used for HHG. These peaks are also referred to as "harmonics". Upon ionization, the electron transitions from a bound state to a continuum state. When a phase-locked weak IR pulse($\leq 10^{11} W/cm^2$ [46]) is used along with the XUV, the electron could either absorb or emit an IR photon in the continuum and reach a state in between the harmonics. These states are called "sidebands" and are at a spacing of one IR photon energy from two of its neighbour harmonics, thereby an even multiple of the IR photon energy.

Each sideband state in the continuum can be reached by two pathways involving neighbouring harmonic states, as shown in Fig. 2.1. When there are two possible pathways to reach the same final state, there is a quantum interference. This interference is controlled by the relative phase between XUV and IR pulses. Varying the phase between XUV and IR pulses translates to a time delay variation. The strength of each sideband peak therefore varies as a function of the timing between XUV and IR pulses and are also called the "sideband oscillations". These oscillations have a frequency of $2\omega_{IR}$, since two IR photons are required to reach a sideband state.

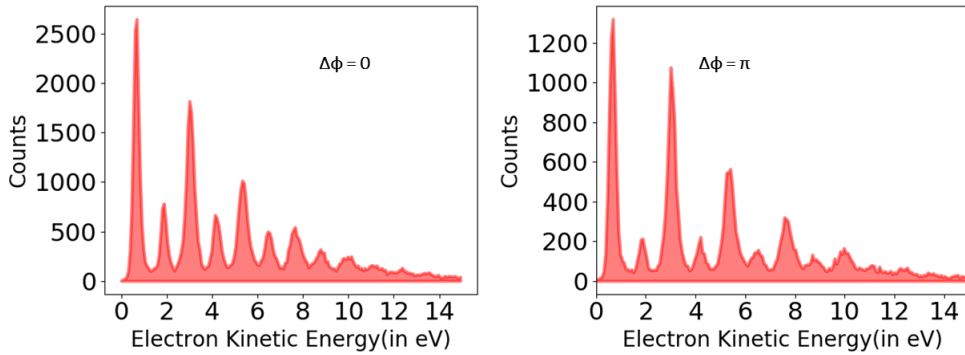


Figure 2.2: Variation of sideband intensity as a function of the phase between XUV and IR pulses

Performing delay scans back and forth and recording the photoelectron spectrum results in a 2-D histogram like the one seen in figure 2.3 below. These sideband oscillations are at the core of the RABBIT technique, which stands for ***Reconstruction of Attosecond Beating By Interference of Two-photon transitions***.

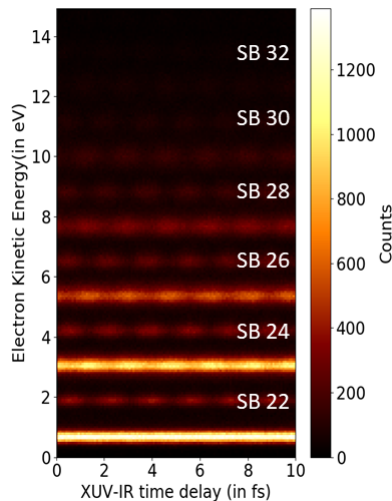


Figure 2.3: Experimentally recorded RABBIT trace for electrons from the ionization of helium atoms

The RABBIT technique was initially used only for attosecond pulse metrology[47]. Over the last decade however, a variety of measurements have expanded the scope of this technique to include probing attosecond electron dynamics in atoms and molecules (eg. [48, 49, 50, 51]). The oscillation phases vary as a function of electron kinetic energy, resulting from a combination of XUV spectral phase and a contribution from the photoionization process itself. The sideband oscillations are

expressed by a cosine function of the form[52] :

$$I_{SB}(t) = \alpha + \beta \cos(2\omega_{IR}\tau + \Delta\phi_{XUV} + \Delta\phi_{atomic}) \quad (2.1)$$

where α is an offset parameter, β is the amplitude, τ is the XUV-IR time delay, $\Delta\phi_{XUV}$ is the phase related to XUV harmonics, $\Delta\phi_{atomic}$ is the phase associated with the ionization process itself. By using the expression $\tau = \frac{\Delta\phi}{2\omega_{IR}}$, the phase can be converted to time. The significance of various phase components will be explained in a little more detail in the forthcoming section.

2.2 Attochirp, Wigner and Continuum-Continuum Delays

The three phase components in eq. 6.2 can be understood as follows. When the sideband oscillations are treated simply as a cosine function, they have a frequency of $2\omega_{IR}$ and phase is obtained by multiplying the frequency with the time, in this case the XUV-IR delay τ . The sidebands however are formed due to a two photon process involving ionization by XUV followed by IR induced transitions in the continuum. These processes impart additional phase shifts to the oscillations and are accounted for by the other two terms.

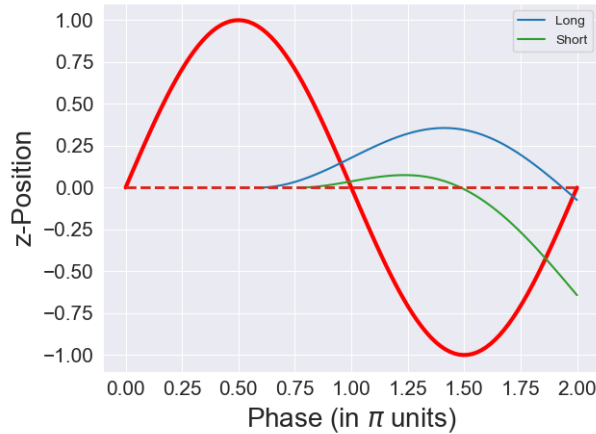


Figure 2.4: Examples of long and short trajectories in HHG

The $\Delta\phi_{XUV}$ term or *Attochirp* originates from the high-harmonic generation process and is the group delay between each harmonic. From the three-step model for HHG (Sec. 1.1.3) and the classical expression for the trajectory of a quasi-free electron in the laser field (Eq. 1.21), there are two types of trajectories the electron could take, depending on the instant of release. These are the *short* and *long* trajectories (Fig. 2.4). The energy released when the electron recollides with the parent ion depends on the trajectory. The kinetic energy gained by the electrons released at various instants will be proportional to the square of the slope difference between the two trajectories during recombination (detailed mathematical

analysis in [53]). This energy dependence on the trajectories results in a varying spectral phase for each harmonic. Together, the entire comb of frequencies therefore exhibits a group delay, which influences the phase of the outgoing electron wavepacket upon ionization. The $\Delta\phi_{XUV}$ is usually converted to time and is expressed in units of as/eV. In most RABBIT measurements with atoms, a value of few hundred attoseconds over four or five consecutive sidebands is measured.

The other phase quantity $\Delta\phi_{atomic}$ is called the atomic phase and contains all the information related to the photoionization process. The atomic phase expression takes into account the contribution from direct ionization by XUV as well as the phase shift of the quasi-free electron in the continuum. The atomic phase can be converted to time delay and taking into account the two components, we have[52]:

$$\tau_{atomic} = \tau_{Wigner} + \tau_{CC} \quad (2.2)$$

The *Wigner* term arises from the transition of an electron from a bound state to a continuum state, after ionization by XUV. The concept, originally introduced by Eugene Wigner[54] in 1955, is the phase shift an electron wavepacket acquires as it passes through a short range attractive potential and is given by

$$\tau_{Wigner} = \hbar \frac{\partial \delta(E)}{\partial E} \quad (2.3)$$

where $\delta(E)$ is the energy dependent scattering phase acquired by the electron wavepacket.

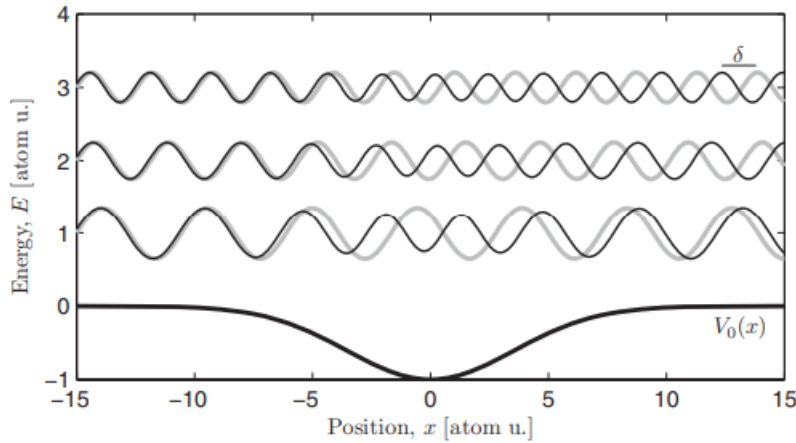


Figure 2.5: Propagation of electron wavepackets with various kinetic energies in the vicinity of a Coulomb potential (black lines) in comparison to a freely propagating electron having the same kinetic energy (gray lines). Figure taken from [52].

To understand this, we consider an electron with kinetic energy E and picture two cases - one where it propagates in the vicinity of an attractive potential and in

the other case, it propagates as a free electron. Due to scattering by the potential, the electron wavepacket is phase shifted in comparison to its freely propagating counterpart. This phase shift can be converted into a delay and depending on the sign of the phase shift, the wavepacket is said to be advanced or retarded. In the case of photoionization, the phase shift calculated for a given kinetic energy needs to be halved, since photoionization is a half-scattering process where the electron appears in the continuum at the center of the potential and then propagates[52, 55].

The *CC-term* or the continuum-continuum delay is a measurement induced delay and arises from the interaction of an electron in the continuum with an IR pulse. For weak IR pulses that are linearly polarized, the electrons in the continuum undergo transitions following the selection rule $\Delta l = \pm 1$, which ultimately leads to the formation of sidebands. This transition in the continuum occurs in the long-range Coulomb tail[52] and results in a non-trivial phase shift to the outgoing wavepacket. The continuum-continuum phases are usually calculated from an above-threshold ionization perspective since the electron is already free when it exchanges the second photon. The continuum-continuum delay is therefore a convolution of phase-shifts arising from various pathways dependent on the angular momentum of the intermediate state (ie state after XUV ionization).

The probability of continuum-continuum transitions increases with electron kinetic energy, which in turn increases the importance of the τ_{CC} term at higher energies[46, 52]. The τ_{Wigner} on the other hand is dominant at lower kinetic energies. In any XUV-IR pump-probe measurement, the IR pulse acts as a clock to measure the phase of the electron wavepacket and hence it is extremely important to estimate the τ_{CC} accurately to be able to estimate the τ_{Wigner} .

2.3 Phase Extraction

Having discussed the various contributions to sideband oscillation phases, we will briefly look at how to retrieve the phase from an experimental dataset.

Fitting a cosine function

The easiest way to extract phases from the sideband oscillations is by using a cosine fit (Fig. 2.6). In order to do this, a projection of the sideband oscillations along the delay axis is taken. A delay range over which the amplitude is almost constant is then chosen and is fitted with a function similar to eq. 6.2, given by :

$$I_{SB} = A \cos(2\omega_{IR}\tau + \phi) + B \quad (2.4)$$

The amplitude A, offset B and phase ϕ are the free parameters in the fit, while the $2\omega_{IR}\tau$ term is kept a constant, for consistent fitting over all sidebands. Using a least-squares optimization function based on the Levenberg-Marquardt algorithm

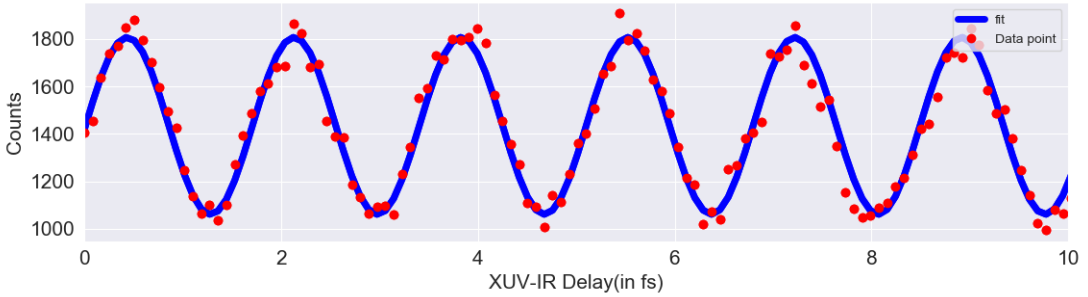


Figure 2.6: Projection of Sideband 24 in Helium (integrated over electron KE 4.0 - 4.5 eV in Fig.2.3) and the cosine fit for the oscillations

¹ [56, 57], the amplitude and phase of the oscillations can be determined. Uncertainties in the amplitude and phase are obtained from the covariance matrix, which is given by:

$$C(A, B, \phi) = \begin{bmatrix} \sigma_A^2 & \sigma_A\sigma_B & \sigma_A\sigma_\phi \\ \sigma_B\sigma_A & \sigma_B^2 & \sigma_B\sigma_\phi \\ \sigma_\phi\sigma_A & \sigma_\phi\sigma_B & \sigma_\phi^2 \end{bmatrix} \quad (2.5)$$

The terms $\sigma_A^2, \sigma_B^2, \sigma_\phi^2$ are the respective variances. By taking the square root of the diagonal elements in the covariance matrix, the standard-error for each parameter is obtained. The fit is hence a very popular method to extract the amplitude and phase due to its simplicity but has a few sources of error which need to be taken into account.

Firstly, an assumption needs to be made with regard to the frequency of oscillation. The fit function defined above works only for two-photon transitions to reach the final state and hence has only one oscillation frequency. If the IR intensity is high enough to result in 4-photon or 6-photon transitions in the continuum, this would result in sideband oscillations at higher frequencies(ie. $4\omega_{IR}$, $6\omega_{IR}$ etc.)[58]. The presence of higher frequencies reduces the contrast of oscillations and thereby the accuracy of the fit. Therefore, the higher order transitions need to be accounted for and additional frequency terms are required in the fit function.

Second, the fit is also sensitive to amplitude variations and hence the phase retrieved is sensitive to the time-delay window selected. Although the accuracy of the fit increases with the number of cycles, sideband oscillations have a constant amplitude and frequency only close to the center of XUV-IR temporal overlap. A sliding window analysis (as explained in [59]) can help identify the optimal delay range. For most RABBIT measurements presented in this thesis, a delay window covering 6 cycles(≈ 10 fs) is chosen for an optimal fit.

Finally, the energy window over which the sideband signal is integrated also needs to be chosen carefully. For energies where the harmonics and sidebands

¹Implemented using the `scipy.optimize.least_squares` function in **Python**

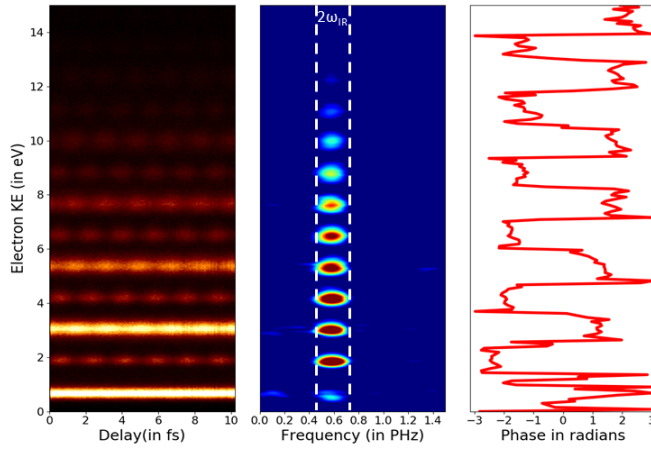


Figure 2.7: Left: RABBIT trace from Fig. 2.3, Center : Linewise FFT showing the presence of only $2\omega_{IR}$ component in the sideband oscillations, Right: Phase retrieved from the FFT for each energy bin. The harmonics and sidebands oscillate almost π radians out of phase w.r.t each other.

overlap, there is a phase jump of π radians, which when included in the sideband projection, influences the phase significantly. In addition, the phase can vary over the sideband energies due to resonances as shown in ref. [60].

To minimize these errors, the fit could therefore be augmented with a linewise Fast-Fourier transform(FFT) of the RABBIT trace (Figs. 2.7, 2.8). With the help of a linewise FFT, higher frequencies can be identified and taken into account. Moreover, energies in each sideband having no influence from the neighbouring harmonics can also be identified.

Extracting individual contributions

The phases retrieved from the fit are a combination of the two components explained in the previous section. There are methods however to get the contribution of the XUV and atomic components individually.

To get the $\Delta\phi_{XUV}$ term, the phases for each sideband are taken and plotted. For a low to moderate IR probe intensity, the phases can be assumed to vary linearly with energy. The slope of a linear fit to these points gives the $\Delta\phi_{XUV}$. The phase is converted to time to get the value in units of as/eV. In the RABBIT measurement on Helium presented here, the $\Delta\phi_{XUV}$ is estimated to be approximately 27 as/eV. The phase varies linearly for sidebands 22 through 28 and starts flattening for sidebands 30 and 32, which are dependent on the phases from harmonics 29-33 and in the cutoff region of the HHG spectrum. The flattening of phase around the cutoff arises due to the convergence of long and short trajectories close to the zero of the field[61]. This convergence leads to a vanishing phase variation since all harmonics in the cutoff region are in phase.

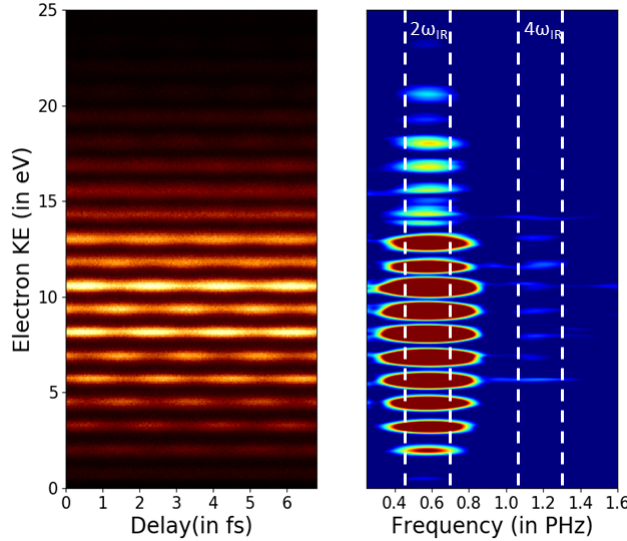


Figure 2.8: Example of a linewise Fourier transform for a RABBIT measurement performed on Argon with a very high probe IR intensity. Multi-photon transitions in the continuum due to the high IR resulted in a noticeable contribution of the $4\omega_{IR}$ oscillation in the RABBIT trace.

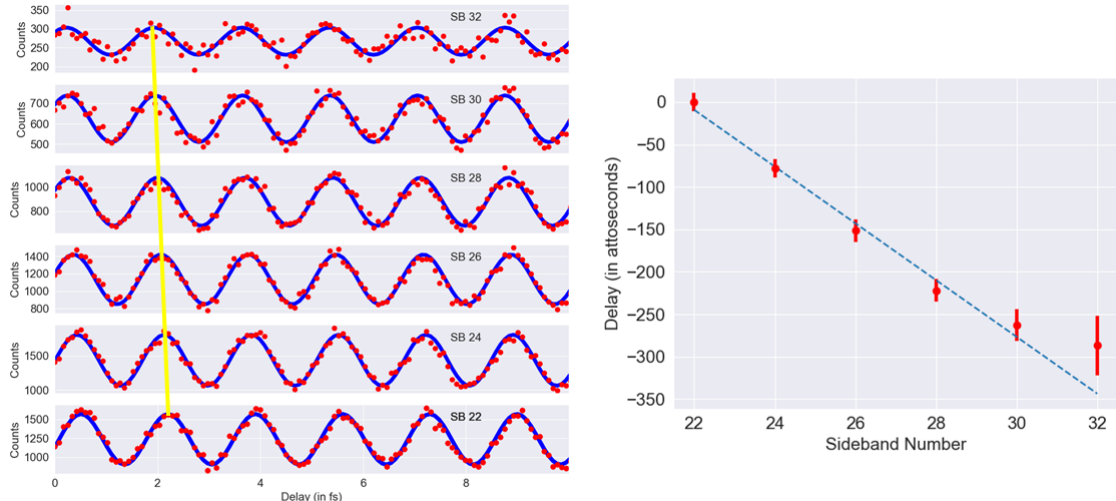


Figure 2.9: Left: Projections of sideband oscillations seen in Fig. 2.3. The yellow line tracks the relative phase between the oscillations. Right: The phases converted to time delays(red points) along with the linear fit (dashed blue line).

While comparing the phases across various sidebands for the same atom, the $\Delta\phi_{atomic}$ varies as well. However, in general $\Delta\phi_{atomic} \ll \Delta\phi_{XUV}$ [52] across the sidebands and hence $\Delta\phi_{atomic}$ can be neglected in this estimation.

To estimate the $\Delta\phi_{atomic}$ component, the $\Delta\phi_{XUV}$ needs to be eliminated and this can be achieved in a few different ways. One is by performing a measurement with two different targets simultaneously and comparing the respective sideband phases(eg. [62, 63, 64]). With this method, we obtain the difference of atomic phases for two atoms A & B ($\Delta\phi_{atomic}(A - B)$), which can be supplemented with theoretical calculations to obtain the τ_{Wigner} and τ_{CC} values. Other ways to eliminate the $\Delta\phi_{XUV}$ include looking at electrons ionized from different shells in the same atom [48] or measuring the phases of each sideband as a function of emission angle (w.r.t laser polarization axis)[65, 66].

All the above mentioned methods to measure the $\Delta\phi_{atomic}$ term results in a value that is a mix of the *Wigner* and *CC* terms. In the recent years, a novel method has been developed to extract the τ_{CC} term in isolation from the others[67, 68]. In this method, the XUV is generated by the second harmonic of the driving laser while the probe frequency is kept the same. Due to the doubled spacing between harmonics, three photon transitions with the fundamental IR probe pulses are required to reach a sideband state. Therefore, instead of one sideband, there are three sidebands and analyzing the phases of these sidebands provides direct insights into the τ_{CC} term.

2.4 Attosecond Pulse Reconstruction

Having discussed the extraction of phases from a RABBIT trace, we will now look at how the extracted phases can be used to reconstruct the pulses in an attosecond pulse train. To reconstruct the pulses produced by HHG, a RABBIT measurement on Argon (Fig. 2.10) is used. The lower ionization threshold of Argon allows inclusion of phases from lower harmonics into the pulse reconstruction.

In order to reconstruct a pulse, the spectral amplitude and phase are required. The spectral amplitude for each harmonic can be measured using a calibrated XUV spectrometer. In the absence of an XUV spectrometer, the photoelectron spectrum obtained from the ionization by XUV can be used (explained in Sec. 1.1.4). This method works effectively only when the detectors have a flat response across all electron kinetic energies and the resolution provided by the electron spectrometer is better than the bandwidth of each harmonic.

The XUV group delays obtained from the analysis of sideband oscillations is used to calculate the spectral phase of the harmonics. By integrating the line fitted to the group delays, the quadratic spectral phase for each harmonic Φ_q (where q is the order of the harmonic) is obtained. In Fig. 2.10, the sideband 16 is set to zero and the relative phases of the rest of the harmonics are calculated. While performing a linear regression fit, the phase of Sideband 16 is not included, since it deviates largely from the other points. The reason for this strong deviation is an aluminium filter used to separate the XUV from IR after HHG (see Fig. 3.4). Measurements on aluminium filters with various thicknesses, presented in [69]

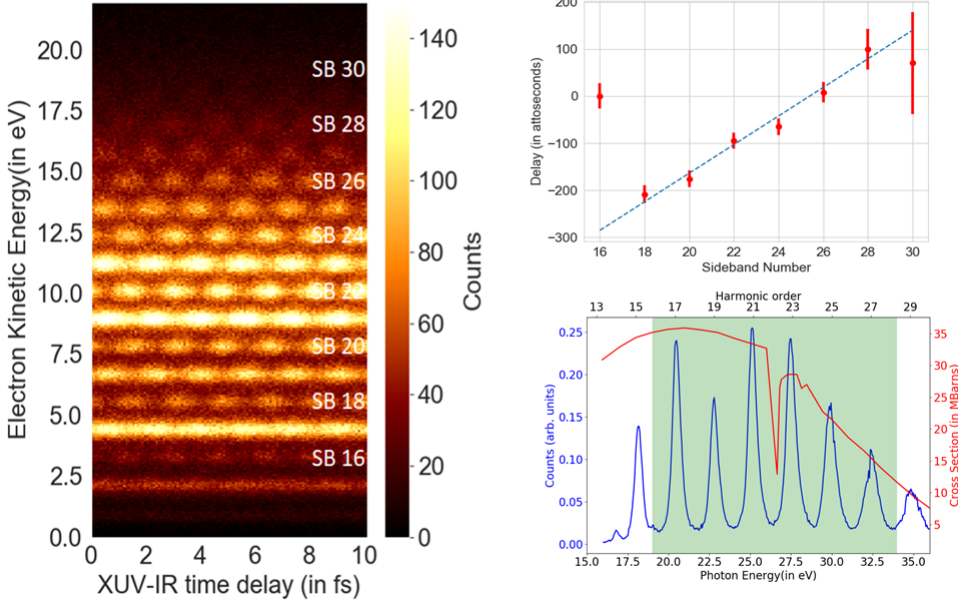


Figure 2.10: Left : Experimental RABBIT trace from a measurement on Argon, Right: Top - The XUV group delays extracted from the RABBIT trace, Bottom - XUV photon spectrum obtained from the photoelectron spectrum. The area shaded green denotes the harmonics chosen for pulse reconstruction

show that the strong deviation of phase for the lower sidebands are indeed due to the dispersion introduced by the filter.

With the spectral amplitude and phase, the temporal profile of the attosecond pulses can be reconstructed as [69]:

$$I(t) = \left| \sum_{q=18}^{28} \sqrt{I_q} e^{-iq\omega t - \Phi_q} \right|^2$$

For the pulse reconstruction, spectral amplitudes of harmonics 17 to 27 are used, along with the phases from sidebands 18 to 28. Sideband 30 is left out since the cosine fit returns a large error bar for the phase. The reconstructed pulses are seen in Fig. 2.11. The Fourier limited pulses for the given bandwidth have a duration of about 305 attoseconds. This is obtained by taking the XUV frequency comb in Fig. 2.10 and setting the same height to all peaks along with keeping the spectral phase zero. The duration of pulses including the chirp and spectral amplitudes is 410 ± 30 attoseconds, clearly indicating broadening by the chirp.

The chirp of attosecond pulses could be reduced by using thick aluminium filters after HHG[61]. This is because, the pulses produced by HHG are intrinsically negatively chirped and propagation through the filter introduces positive chirp, thereby reducing the overall chirp of the pulse. However, filters that are too thick

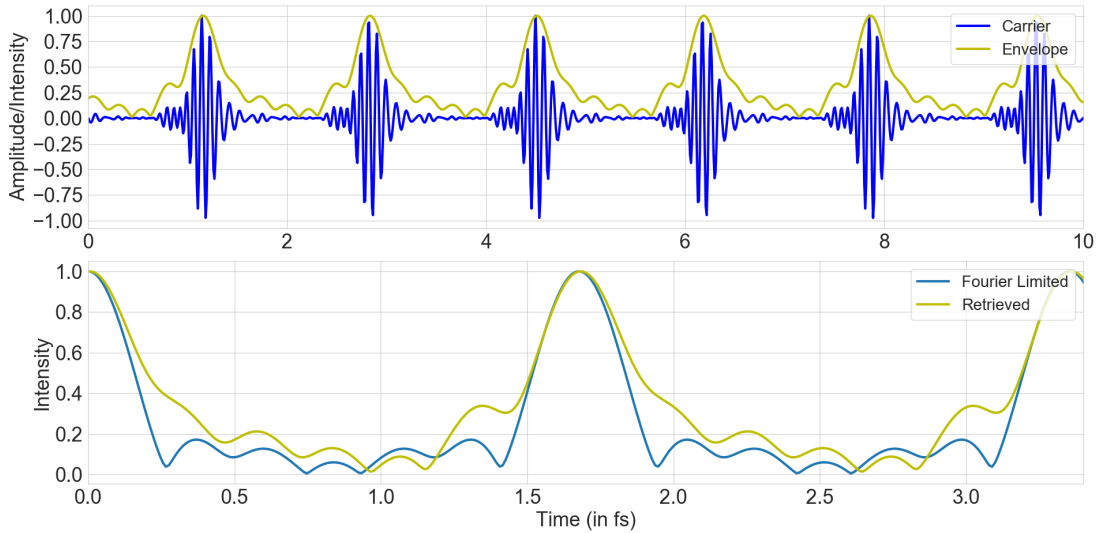


Figure 2.11: Top : Attosecond pulse train retrieved using the XUV spectrum and group-delays from the RABBIT trace, Bottom : The envelope of the retrieved pulse with chirp in comparison to the Fourier Limited pulses for the bandwidth

would result in a significant reduction of the XUV flux. So, a balance needs to be achieved between the chirp and flux. For this RABBIT measurement, aluminium filters with thickness ≈ 200 nanometers were used.

Another way to bring the attosecond pulse duration close to the Fourier limit, is by adjusting the chirp of the IR pulse used in HHG. Adding a small amount of positive chirp in the IR pulse helps achieve optimal XUV pulse durations. Experimentally, this is achieved by adjusting the incidence on a grating inside the laser amplifier or compressor.

To summarize, the RABBIT technique is a versatile tool to not only measure attosecond pulses, but also to study the dynamics of photoionization. The spectral phases obtained from a RABBIT measurement on noble gas atoms, can be combined with the spectral amplitudes of the harmonics to reconstruct the temporal profiles of the pulses in an attosecond pulse train. Although this method requires assumptions and does not always provide a complete characterization of the pulse, it helps making a very good guess of the XUV pulse duration. New algorithms developed in the recent years (eg. [70, 71]) can reconstruct the entire RABBIT spectrum with great accuracy, but are not discussed here due to being beyond the scope of this work.

3 Experimental Details

In order to carry out photoionization measurements, two experimental apparatuses are necessary : a light source and an electron/ion detector. This chapter contains a detailed explanation of the experimental setup used for the photoionization measurements presented in this thesis.

3.1 The Laser

The current experimental setup uses laser pulses from a commercially available femtosecond laser system from Active Fiber Systems[®] GmbH. The laser comprises of an oscillator which produces low energy pulses and an amplifier system which increases the pulse energy by several fold. The system is completely based on optical fibers - both for generating the seed pulses in the oscillator and subsequent amplification as well. The mechanism to generate and amplify pulses using such an optical fiber based system is explained in detail in the following references: [72, 73, 74]. However, a short summary of the whole process will comprise the rest of this section.

A schematic diagram of the laser is in Figure 3.1. The ultrashort pulses are generated in an oscillator through the mechanism of modelocking in optical fibers[75, 76]. The repetition rate is in the order of 100 MHz. These pulses are of very low energy (≈ 10 nJ) and are then prestretched temporally before amplification. A significant number of pulses are dumped with the help of an Acousto-Optic Modulator, and the pulses now have a repetition rate of 150 KHz. They are then amplified using the *Coherent Combination* [74] method, where the pulses from the oscillator are split into 8 parts temporally, amplified individually and later recombined. This method of amplifying pulses provides a crucial advantage over traditional femtosecond laser amplifiers using Ti:Sapphire crystals, since the former can be operated at high repetition rates.

In Ti:Sapphire amplifiers, the seed pulses from the oscillator are stretched temporally with a pair of gratings and these pulses then pass multiple times through a Ti:Sapphire crystal which is irradiated by another pump laser beam. During each pass the pulses are optically pumped and thereby amplified. This method however does not support high repetition rates due to excessive heating of the gain medium and subsequent damage to it. In a fiber laser, the process involves temporally splitting the beam and then amplifying it and hence high repetition rates do not damage the gain medium.

After amplification, the pulses are temporally recombined and also compressed

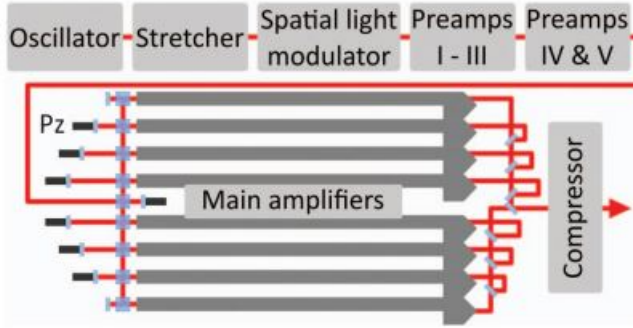


Figure 3.1: The laser's seed and amplification stage. Figure taken from [73]

with the help of a grating compressor. This process yields pulses with a duration of ≈ 250 fs and energy around 2 mJ. These pulses are then sent to a 2-step pulse compression stage which uses hollow core fibers filled with Argon or Neon[77, 78].

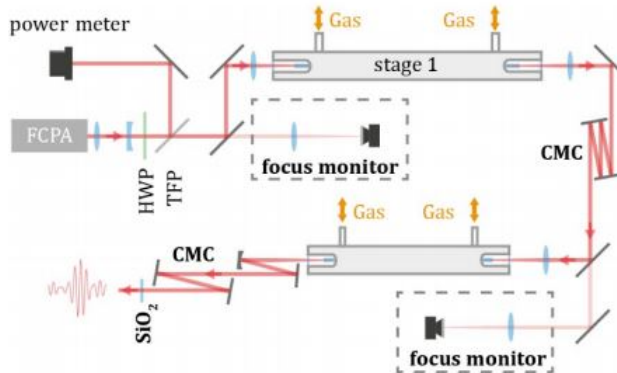


Figure 3.2: A schematic of the Hollow Core Fiber compressor stage of the laser.
Figure taken from [77]

These hollow core fibers spectrally broaden the pulses from the amplifier in order to temporally shorten them. This happens through a process called *Self-Phase Modulation*[79]. The pulses that exit the hollow core fiber although spectrally broad, are not temporally short due to a large amount of spectral dispersion. This dispersion is reduced using a *Chirped Mirror Compressor* [80, 81] at the exit of the hollow core fiber. These mirrors have special coatings which compensate the spectral dispersion at every reflection on the surface of the mirror. The pulses are reflected multiple times off these chirped mirrors and the pulses are temporally compressed down to 40 fs. The pulse energy is reduced to about 1 mJ now as a consequence of the self-phase modulation inside the hollow core fiber which usually has about 50 – 55% efficiency. With the provision of a second hollow core fiber, the 40fs pulses can be further spectrally broadened and thereby a pulse duration of about 8 fs can be obtained albeit without *Carrier-Envelope-Phase*(CEP) Stabilization[82]. The output power reduces then to about 0.7 mJ.

These compressed pulses are then sent to a beamline comprising a Mach-Zehnder Interferometer[5].

3.2 Interferometric Setup for Pump-Probe experiments

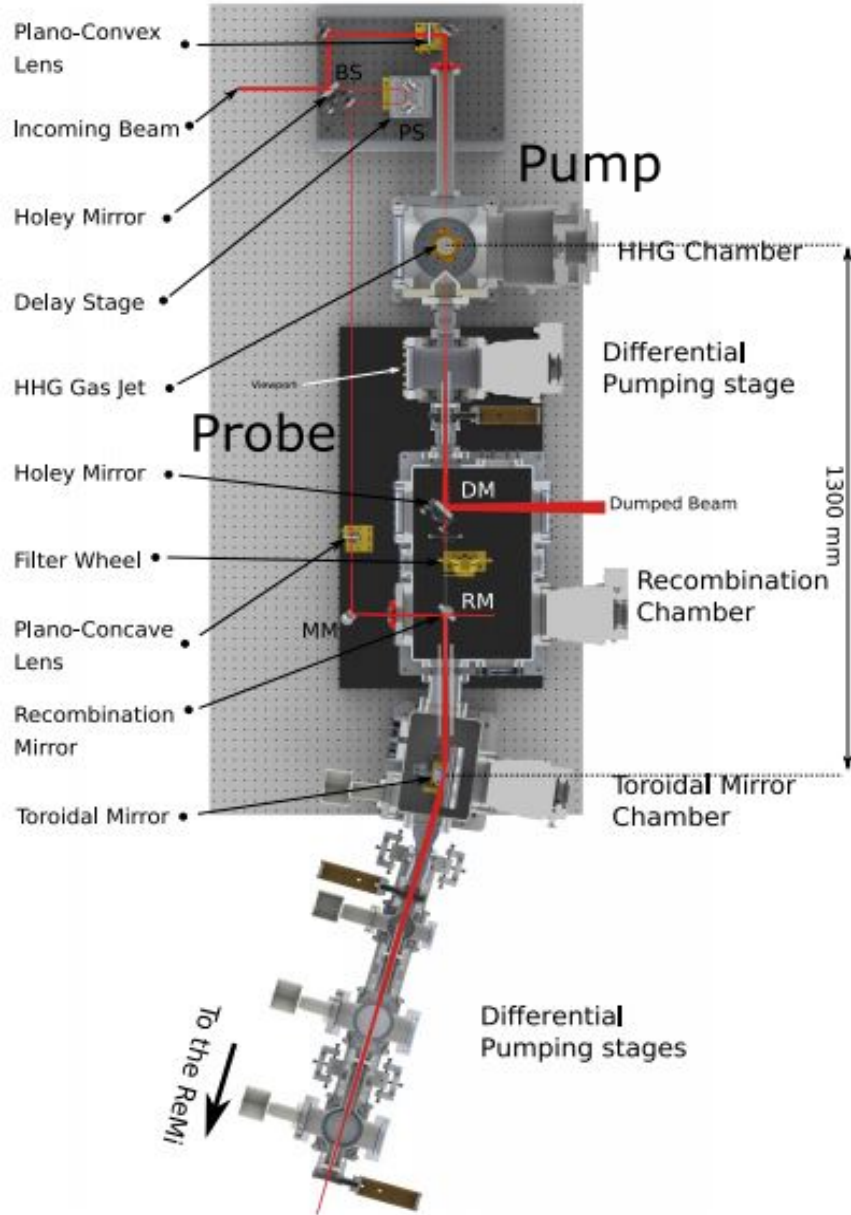


Figure 3.3: Schematic of the beamline. Figure taken from [32]

A Mach-Zehnder interferometer arrangement is used for pump-probe measurements as shown in Fig. 3.3. A mirror with a 3 mm diameter hole(BS) acts as

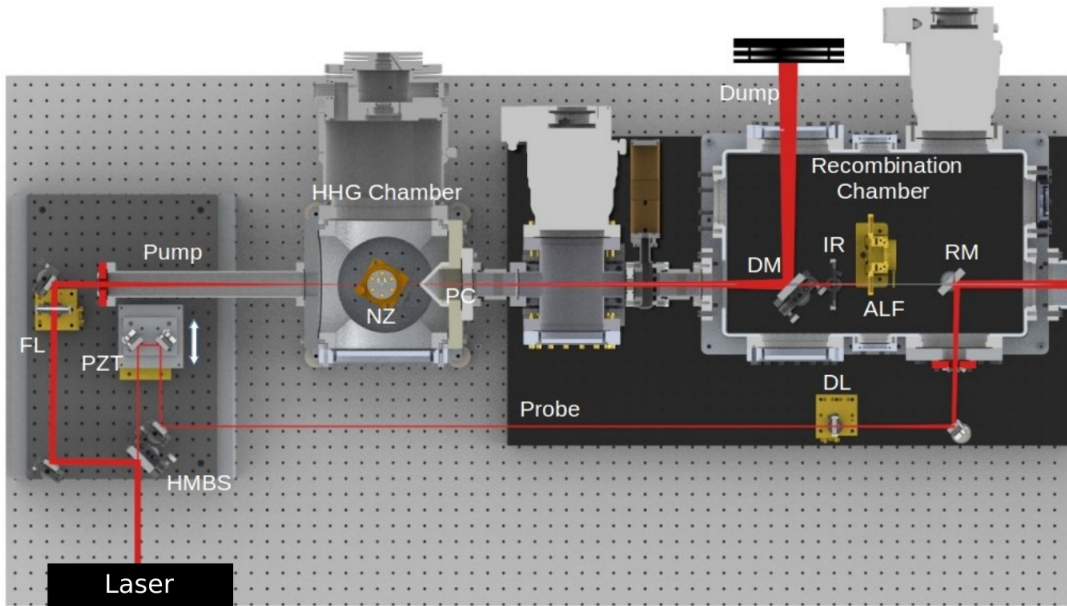


Figure 3.4: Zoomed in view of the interferometer, containing the HHG and recombination chambers. Legend: HMBS - Holey Mirror Beam Splitter, FL - Focusing Lens, NZ - Gas Nozzle, PC- Differential pumping cone, DM - Dump Mirror, IR- Iris, ALF - Aluminium Filter, RM - Recombination Mirror, PZT - Piezo Stage, DL - Diverging Lens

a beam splitter and splits the incoming beam with an R:T ratio of $\approx 85:15$. The stronger part of the beam is reflected by this mirror and travels through the "Pump" arm of the interferometer and weaker part is transmitted through the hole in the mirror and goes through the "Probe" arm of the interferometer. The High Harmonics generation chamber, lies in the Pump arm of the interferometer, where the XUV light is generated. The IR beam is focused with a 50 cm focal length convex lens and a gas nozzle is placed at the focus for generating the XUV light. The target gas is usually Argon with a backing pressure of 1.5 bars and the chamber pressure is about 5×10^{-2} mbar. The HHG chamber is then isolated from the Recombination Chamber which is at a pressure of 10^{-6} mbar with the help of an intermediate stage pumped by a turbomolecular pump with a flow rate of 100 l/s.

The recombination chamber houses the two holey-mirrors. The first mirror (DM) is used as a dump for the IR co-propagating with the XUV after HHG. The XUV beam passes through the center of this mirror. To remove any residual IR light after the dumping mirror, an additional iris is placed in front of an Aluminium filter of 200 nm thickness which then finally eliminates all the IR and lower order harmonics in the XUV beam. The second mirror(RM) has two holes drilled along perpendicular directions. One hole is used for the propagation of XUV light. The IR beam from the probe arm is combined with the XUV beam at the recombination mirror. A small amount of this probe beam passes through the second hole

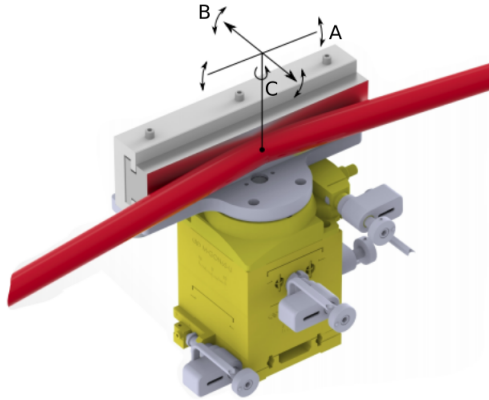


Figure 3.5: Schematic of the toroidal mirror. Axes A, B and C refer to the Pitch, Roll and Yaw axis respectively.

on the holey mirror and is used as a part of the interferometric drift stabilization described in a later chapter.

Downstream the recombination mirror, lies the Toroidal mirror (TM) which focuses both the XUV and IR beams into the Reaction Microscope(Fig.3.5). The Toroidal Mirror is positioned to have a grazing incidence of both the XUV and IR beams and is mounted on three Piezo-Electric stages giving it freedom along the three rotational axes - Yaw, Pitch and Roll[83]. The mirror has a B_4C coating and is placed such that it is at a distance of 130 cm from the focus inside the HHG chamber as well as the focus inside the REMI. This allows to have a 1:1 mapping of the XUV focus inside the REMI. It also eliminates the need to use a combination of cylindrical and spherical mirrors in a *Kirkpatrick-Baez* arrangement[84, 85], used typically to focus XUV/X-ray beams. The pressure inside the Toroidal Mirror chamber is typically 5×10^{-7} mbar or better. In order to reach a pressure of $\approx 10^{-11}$ mbar inside the Reaction Microscope, a differential pumping stage is in place between the Toroidal Mirror Chamber and the REMI. This stage is pumped by three different turbomolecular pumps helping to reach a pressure of 10^{-10} mbar at the end and providing a smooth pressure gradient between the Toroidal Mirror Chamber and the REMI.

3.3 Reaction Microscope

The Reaction Microscope is a versatile instrument used to detect electrons and ions in coincidence with multihit capabilities and 4π solid angle acceptance, thereby allowing a kinematically complete measurement of ionization processes. The fundamental principles and momentum reconstruction procedures are explained in great detail in references [86, 87]. The reaction microscope used in all the experiments here was built by a former PhD student in the group and the technical details are explained in the reference [20]. The setup comprises of an electron

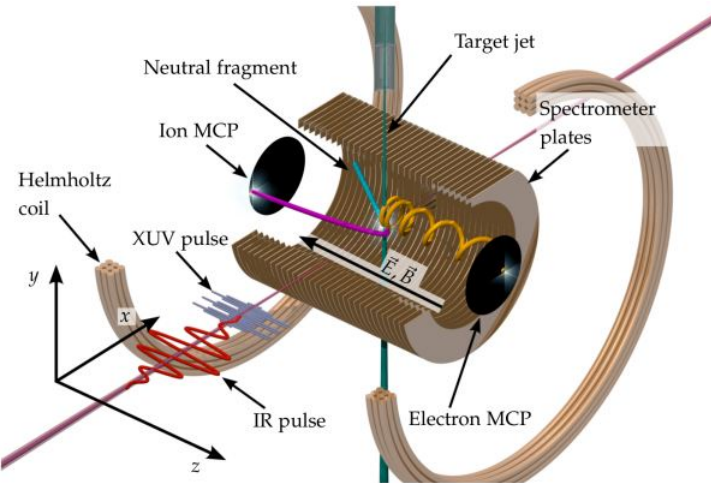


Figure 3.6: A schematic of the Reaction Microscope. Figure taken from [88]

and ion detector (Fig.3.6), with the charged particles being accelerated to their respective detectors by electric fields in association with a collinear uniform magnetic field introduced using a pair of *Helmholtz* coils [89].

3.3.1 Target

The target for photoionization measurements with the ReMi is a supersonic gas jet [90] (Fig. 3.7). The target gas is taken from a gas bottle with a backing pressure of a few bars and allowed to expand supersonically through a nozzle with a diameter of $30\mu\text{m}$ into a region with pressure of the order of 10^{-1} mbar. This cools the atoms and molecules in the gas jet from room temperature to a few Kelvins, reducing the thermal energy to ≈ 50 meV. The gas jet then passes through two successive stages which are pumped by turbomolecular pumps resulting in a pressure of $\approx 10^{-4}$ mbar and $\approx 10^{-6}$ mbar respectively. These stages have one skimmer each with diameters $150\mu\text{m}$ and $200\mu\text{m}$ respectively to let through only the central part of the jet that is cold. The collimated jet now has a very low momentum spread perpendicular to its direction of motion and interacts with the incoming laser beam in the interaction chamber. The interaction chamber is usually at a pressure of $\approx 10^{-10}$ mbar in the presence of the jet. The gas jet then continues further downstream into a dump, which is continuously pumped using a 300 l/s turbomolecular pump.

3.3.2 Spectrometer and Detector

The electron and ion spectrometers (Fig. 3.8) are together made of 32 metal plates each with a spacing of about 7 mm [20]. These plates provide a homogenous electric field to accelerate and guide the charged particle fragments onto their respective detectors. The spectrometer has a Wiley-McLaren configuration[91]

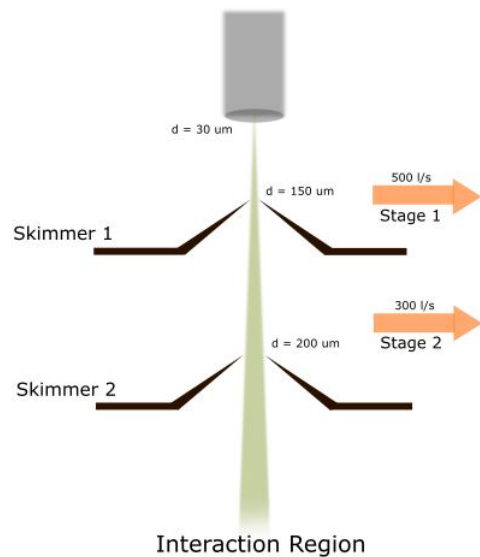


Figure 3.7: Schematic of the target gas jet undergoing supersonic expansion

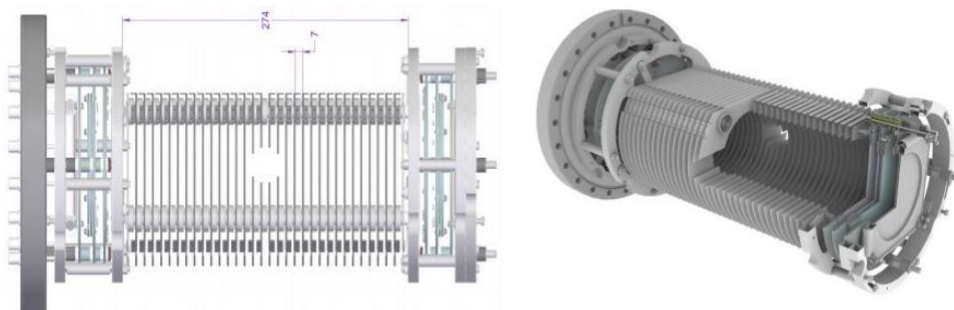


Figure 3.8: 3D CAD drawing of the Spectrometer. Figure taken from [32]

without the field-free drift region. Along with the electric fields for acceleration is an additional co-axial magnetic field provided by the Helmholtz coils. These help in achieving a 4π solid angle acceptance for the electrons. The electrons exhibit helical motion on the way to the detector due to the combined action of the electric and magnetic fields.

The electrons and ions impinge on the Multichannel Plate (MCP) Detectors[92]. These MCPs are (usually circular) disks having an array of tiny photomultiplier tubes, each with a diameter of roughly $10\mu m$.

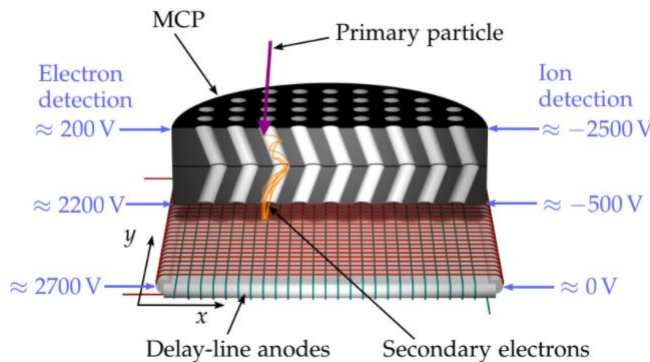


Figure 3.9: Schematic of the working of the MCPs in conjunction with the Delay line anodes. Figure taken from [88]

As a charged particle impinges on one of the channels, it leads to emission of secondary electrons upon each successive collision with the walls of the channel. The end result is a roughly 10^6 times amplification of the incoming signal and this leads to a bunch of electrons striking the delay line anode. A voltage drop occurs between the front and back edges of the MCP and this can be used to calculate the time of flight for the ions and electrons from the instant of ionization at the interaction region.

This makes use of the arrival of the laser pulse as a reference (t_{ref}) and the TOF is calculated as : $TOF = t_{MCP} - t_{ref}$, where t_{MCP} is the instant when the voltage drop is detected on the MCP. The TOF helps determine the longitudinal momentum (\vec{P}_{long} or $\vec{P}_{||}$).

The delay line anode is used to determine the position at which the charged particles strike the detector. With this information, the transversal component (\vec{P}_{trans} or \vec{P}_{\perp}) can be determined. From the projections of the transversal component of the momentum, the individual momenta along the two axes can be obtained, thereby providing all the three momentum components.

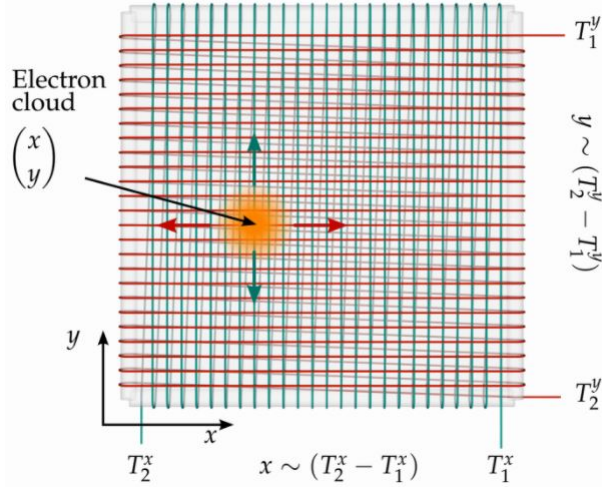


Figure 3.10: Schematic of the Delay Line Anode (figure taken from [88]). Based on the time taken for the signals to reach the end of the grid, the position of the hit on the detector is determined.

The delay line anode comprises of 2 sets of wires wound equidistantly and perpendicular to each other, thereby forming a two dimensional meshgrid. When the electron bunch strikes the grid, the signal propagates to the two ends of the wire (on each axis) which is biased with a positive voltage, higher than that of the backside of the MCP.

Consider the set of wires labelled as x . Assuming this signal propagates at a velocity v_{sig} , and takes time T_1^x and T_2^x respectively to reach the ends. The x and y coordinates can therefore be calculated as:

$$x_{sig} = \frac{v_{sig}}{2} \cdot (T_1^x - T_2^x) \quad y_{sig} = \frac{v_{sig}}{2} \cdot (T_1^y - T_2^y) \quad (3.1)$$

The time taken for the signal to propagate to the ends of the wire remains a constant for a given length of wire. This can be used to filter out events which are either false hits or noise.

$$T_{sum}^x = T_1^x + T_2^x - 2t_{ref} \quad T_{sum}^y = T_1^y + T_2^y - 2t_{ref} \quad (3.2)$$

3.3.3 Momentum Calculation

The prerequisite information to calculate the momenta of ions and electrons lies in their respective time of flights and hit positions on the detectors. To proceed with calculating the momenta of the charged particles, we begin with the Lorentz force for charged particles and Newton's Second law:

$$\vec{F} = q(\vec{E} + \vec{v} \times \vec{B}) = m\vec{a} \quad (3.3)$$

where q is the charge and m is the mass of the particle and \vec{E}, \vec{B} are the electric and magnetic fields respectively. The vector \vec{v} is the velocity of the charged particle and \vec{a} the acceleration experienced by the charged particle. Let the acceleration length be L and the acceleration voltage be U and the time of flight(ToF) of the charged particle to the detector be T .

Ion Momentum

While calculating the momentum for ions, the motion of the ions is fairly independent of the applied magnetic field applied[93]. In order to calculate the longitudinal momentum, only the parallel component of the electric field (E_z) plays a significant role in the acceleration of the ions to the detector.

We are then left with the following differential equation to solve:

$$F_z = qE_z = m_{ion}\ddot{z} \quad (3.4)$$

Upon integration and substituting for the acceleration length and electric field along the z direction, we have:

$$L = \frac{1}{2} \frac{q}{m_{ion}} \frac{U}{L} T^2 + \frac{p_z}{m_{ion}} T \quad (3.5)$$

The constants of integration equate to zero in the above equation since we assume the ionization occurs at the center of the REMI, which acts as the origin. Rearranging this equation, we can get the longitudinal momentum p_z as:

$$p_z = L \frac{m_{ion}}{T} - \frac{1}{2} \frac{qU}{L} T \quad (3.6)$$

For calculating the transversal momentum, the positions of the ion hits on the detector are essential. This can be obtained by solving once again Eq. 3.4 for the components along the x and y directions. Here, the contribution of the electric field is neglected and hence the solution of Eq. 3.4 for the x and y components yields:

$$x = \frac{p_x}{m_{ion}} T \quad y = \frac{p_y}{m_{ion}} T \quad (3.7)$$

Here too, the constants of integration are zero just like in the longitudinal case. Rearranging this equation yields the p_x and p_y momentum components.

$$p_x = \frac{m_{ion}}{T} x \quad p_y = \frac{m_{ion}}{T} y \quad (3.8)$$

Electron Momentum

The longitudinal momentum of electrons is determined in a manner analogous to

that of the ions. The transversal component of the momentum however involves the inclusion of the magnetic field, unlike the ions. The electrons exhibit thus a helical trajectory on its way to the detector. The equations of motion are:

$$F_x = e\dot{y}B_z = m_e\ddot{x} \quad F_y = -e\dot{x}B_z = m_e\ddot{y} \quad F_z = eE_z = m_e\ddot{z} \quad (3.9)$$

The longitudinal component of the momentum is

$$p_z = L\frac{m_e}{T} - \frac{1}{2}\frac{eU}{l}T \quad (3.10)$$

where m_e is the mass of the electrons. It should be noted that the longitudinal momentum of both ions and electrons depend on the sign of the potential used ie. if U is taken positive for electrons it should be taken negative for ions and vice versa.

For the transversal momentum \vec{p}_\perp , we need to consider the helical motion of the electrons (Fig.3.13). This is projected onto the detector in the form of circles. From this, it is possible to reconstruct the helical trajectory as shown in the image 3.12.

The radius of the cyclotron motion can be obtained by equating it with the centrifugal force, which is given by:

$$R_c = \frac{|\vec{p}_\perp|}{eB_z} \quad (3.11)$$

Having obtained the cyclotron radius, it is possible to estimate the hit distance on the detector from the reaction volume. Let this distance be denoted by $|(x,y)|$. The angle α seen in the figure indicates the phase of the helical trajectory. The value of α can be obtained by taking the cyclotron frequency from the above equation and multiplying it with the time of flight(T) of the electron to the detector.

$$\omega_c = \frac{eB_z}{m_e} \quad \alpha = \omega_c T \quad (3.12)$$

Using trigonometry, we arrive at the relation

$$|(x,y)| = 2R_c |\sin(\frac{\alpha}{2})| \quad (3.13)$$

Using Eq. 3.11 and rearranging the terms yields the expression for the transversal momentum

$$|\vec{p}_\perp| = |(x,y)| \frac{eB_z}{2|\sin(\frac{\alpha}{2})|} \quad (3.14)$$

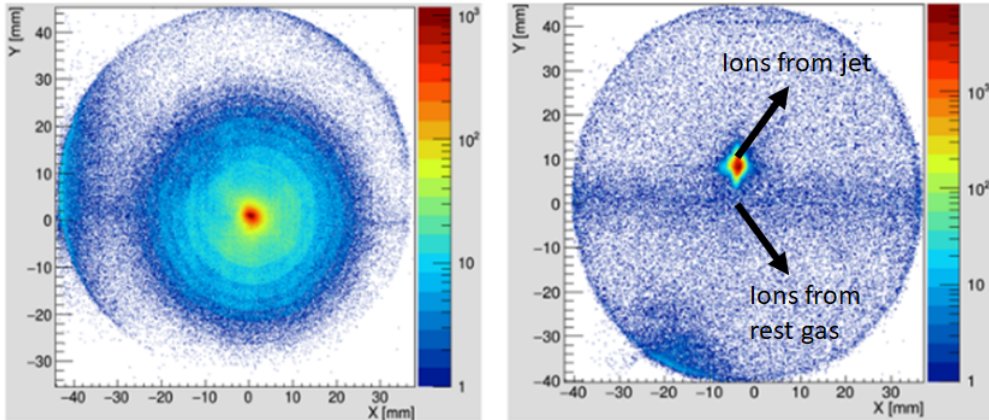


Figure 3.11: Exemplary images of the electron(left) and ion(right) detectors. The concentric rings visible on the electron detector correspond to the electrons coming from ionization by the XUV comb.

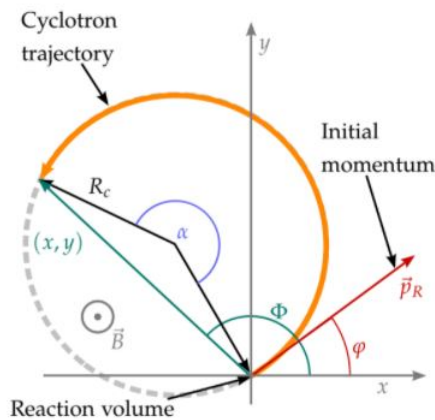


Figure 3.12: Projection of the helical motion on the detector plane. Figure taken from [88]

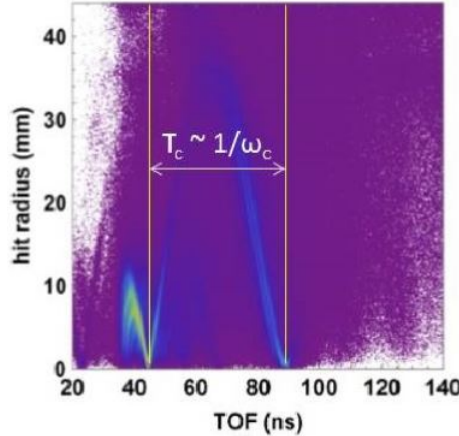


Figure 3.13: A plot of the radius of cyclotron motion versus the time of flight for the electrons

In order to obtain the projections of the transversal momentum along the x and y directions, the angles Φ and φ need to be considered. Using geometry, the angles can be estimated to be:

$$\Phi = \arctan\left(\frac{x}{y}\right) \quad \varphi = \arctan\left(\frac{p_x}{p_y}\right) \quad (3.15)$$

Using this the azimuthal angle of emission φ can be written as

$$\varphi = \phi - \frac{\alpha}{2} \quad (3.16)$$

It should be noted that for electrons satisfying the condition $\alpha = 2n\pi$ (where $n \in N$) will always hit the center of the detector and hence the initial transversal momentum cannot be reconstructed unambiguously. These are called the "Nodes" in the electron momentum distribution.

3.3.4 Acceptance and Resolution of the spectrometer

Acceptance

The acceptance of longitudinal momentum solely depends on the voltage applied and the acceleration length of the charged particles. Therefore the maximum longitudinal momentum for ions and electrons that can be detected is given by

$$p_{||}^{max} = \sqrt{2mqU} \quad (3.17)$$

where m refers to the mass of the charged particle.

The transversal momentum is however influenced by the magnetic field applied, particularly for electrons. Assuming emission of electrons purely along the transversal direction, they can only be detected when the condition $|(x, y)| <$

R_{MCP} (R_{MCP} is the radius of the MCP detector) is satisfied. So for electrons, the maximum transversal momentum that can be detected is

$$p_{\perp}^{max} = BR_{MCP} \quad (3.18)$$

$$p_{\perp}^{max} = R_{MCP} \frac{\sqrt{2mqU}}{2L} \quad (3.19)$$

For all experiments presented in this thesis, an acceleration voltage of 136V along with a field of 9-10 Gauss was used. For ions, this gives a momentum acceptance of ≈ 50 a.u. and for the electrons, it is ≈ 1 a.u. .

Resolution

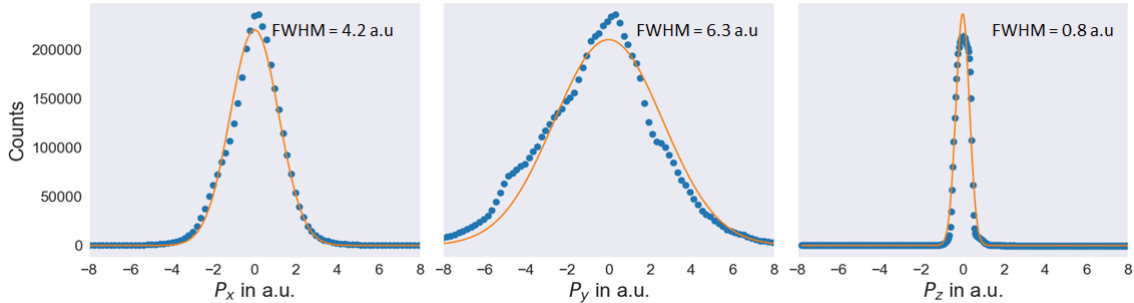


Figure 3.14: Experimental momentum distributions for N_2^+ ions, from the ionization of an N_2 gas jet with XUV. From the gaussian fits, the resolution for each momentum can be determined

The resolution for all charged particles fundamentally depends on the homogeneity and the strength of the electric and magnetic fields. For the electrons in particular, the \vec{E} & \vec{B} fields need to be aligned along the same direction, for optimal resolution. In addition, the bandwidth of the laser pulses influences the resolution for electrons as well. Apart from the influence of the electric field on the resolution for ion momentum, the temperature of the gas jet also plays a crucial role.

The resolution becomes poorer with increasing momentum and needs to be accounted for during calibration. The theoretical calculation of resolution often results in an underestimation and hence the actual resolution offered by the experimental setup can be measured by fitting a Gaussian function to the momentum distributions of ions and electrons (Fig. 3.14).

To conclude, the experimental setup for XUV-IR pump-probe experiments to study photoionization in atoms and molecules has been discussed in this chapter. The reaction microscope is an extremely versatile device to measure get a complete 3-Dimensional picture of atomic and molecular fragmentation. Combining it with a high-repetition rate attosecond beamline opens up opportunities to perform experiments which were earlier extremely challenging.

4 Interferometer Drift Stabilization

In order to acquire a sufficient number of data points from coincidence measurements, the experiment needs to be run anywhere between 6-12 hours, depending on the target of interest. For atomic and molecular systems having tens of kilo-Barns of ionization cross-section in the 20-40 eV photon energy range (eg. single ionization of noble gases and diatomic molecules), several million electron - ion coincidences can be obtained within this time frame. For processes such as the dissociation of diatomic molecules, the cross section is typically two to three orders of magnitude lesser than direct ionization and hence requires an acquisition time of at least 12 hours.

While performing a RABBIT measurement over several hours, due to heating of the optics by the laser, the interferometer path length drifts. This 'smears' out oscillations and reduces the contrast, thereby making phase retrieval challenging. In order to counter this, a method to stabilize the interferometer has been designed and implemented, which will be explained in the forthcoming sections.

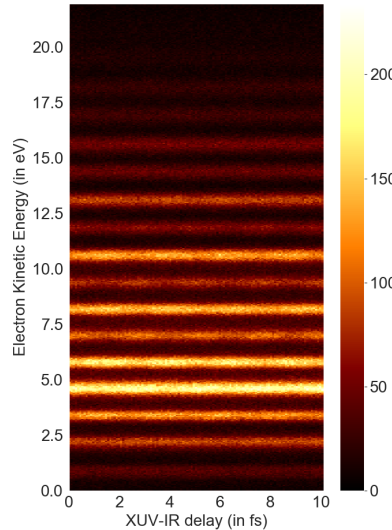


Figure 4.1: Example of a RABBIT trace where the sideband oscillations are smeared out over time, due to thermal drifts.

The contents presented in this chapter are also a part of the following publication: **High-repetition rate attosecond beamline for multi-particle coincidence experiments**, *Optics Express Vol. 30, Issue 8, pp. 13630-13646 (2022)*

4.1 Setup

In this section, a modification to the existing XUV-IR pump-probe setup (explained in Sec. 3.2) will be discussed.

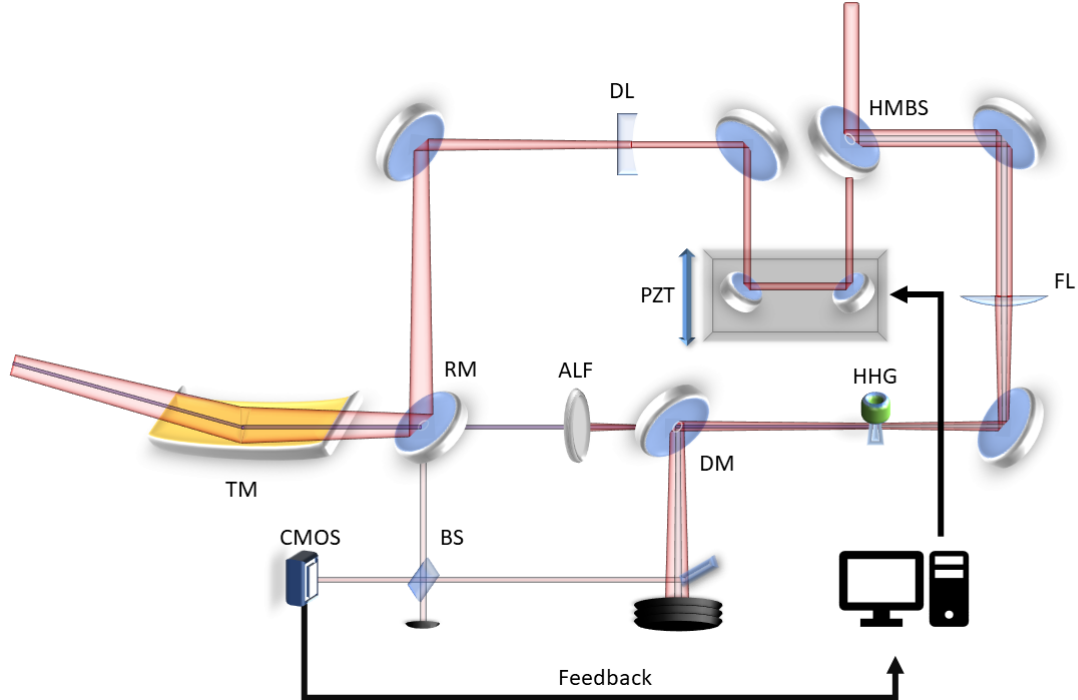


Figure 4.2: Modified Interferometer to include Active-Interferometric Stabilization. Note : HMBS - Holey Mirror Beamsplitter, FL- Focusing Lens, HHG - Gas Nozzle, DM - Dump Mirror, ALF - Aluminium Filter, RM - Recombination Mirror, BS - Beam Splitter, PZT - Piezo Translation Stage, DL - Diverging Lens, CMOS - Camera, TM - Toroidal Mirror

The extension begins with a rectangular silver mirror used to pick up a small portion of the diverging pump beam, that is reflected by the dumping mirror(DM). The dumping mirror on the pump arm of the interferometer has a hole drilled in the center to let the XUV light pass through and to reflect the remaining co-propagating IR beam. The beam picked up by the rectangular mirror passes through an iris in order to get a circular beam with a 3 mm diameter. Following this, the beam is incident on a beam splitter(BS) having an R:T of 70:30. Light from the probe arm passes through a hole in the recombination mirror(RM) and is combined with the pump beam on the beam splitter. Together, the beams are made to interfere on an off-the-shelf CMOS camera mounted outside the vacuum chamber. By adjusting the spatial overlap of the beams, vertical fringes are obtained on the camera and the fringe contrast is further enhanced by moving the translation stage on which the rectangular mirror is mounted.

4.2 Stabilization Method

The method presented here to reduce interferometer drifts is an adaptation of the work done in references [94] and [95]. It relies on a Fourier-Transform based analysis of interference fringes that has its roots in holography and is discussed in detail in references [96, 97, 98]. Firstly, the program uses interference fringes from the camera frame as input signal (Fig. 4.3).

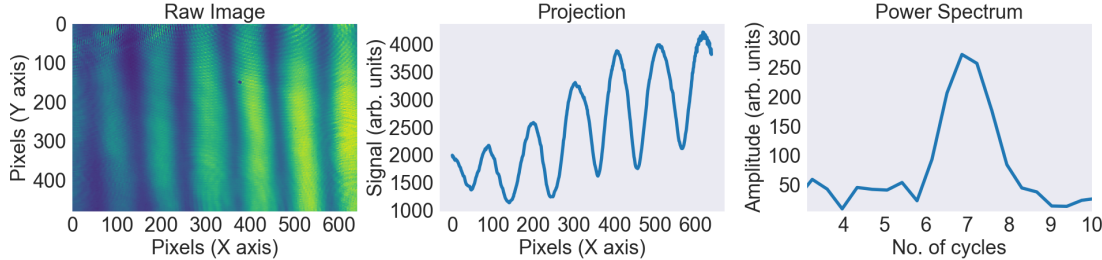


Figure 4.3: Left: False color representation of the interference fringes as seen on the camera, Center: Integrated signal over the selected region of the image, Right: Absolute value of the Fourier transform

The image obtained from the camera is converted from RGB to Grayscale in order to obtain a 2-dimensional matrix. Conversion to Grayscale helps in faster analysis of images and also helps in accurately identifying features such as edges. A section of the image with excellent fringe contrast is chosen and the signal is then integrated over the rows in this window. This gives a sinusoidal waveform. The sinusoidal waveform is transformed into the Frequency Domain with the help of a *Discrete Fourier Transform*[99], which results in a frequency distribution. The mean value of the signal is equivalent to a DC offset given to a sinusoidal wave, which appears as the dominant peak around 0 Frequency units and mean subtraction suppresses this component. A window condition is then applied in the frequency domain to choose the dominant frequency. The phase at the maximum of this frequency window is obtained using the arctangent of the complex-valued Fourier transform X, given by:

$$\Phi(X) = \tan^{-1}\left(\frac{\text{Im}(X)}{\text{Re}(X)}\right) \quad (4.1)$$

This method gives the phase of the interference fringes at any given instant of time, with the sign to indicate the quadrant. By tracking the phases over various durations of time the phase shifts can be compared. A phase variation ($\Delta\phi$) of 2π units would mean a net path length change (ΔL) of one wavelength (λ). Using this, the path length variation of the interferometer is calculated.

$$\Delta L = \Delta\phi \times \frac{\lambda}{2\pi} \quad (4.2)$$

The corresponding length variation in this case is given in nanometres. In order to calculate the path length variation, the central wavelength of the laser beam used needs to be known accurately. This can be done by measuring the spectrum of the laser at the beginning of the experiment.

Alignment

Before obtaining the fringes on the camera from the extension, the actual interferometer is first aligned for a good spatial and temporal overlap. This is done with the help of a camera placed outside the Reaction Microscope(REMI). The beam is directed to the camera outside through a window using a silver mirror mounted inside the REMI. While performing an XUV-IR pump-probe experiment, the image from this camera is not used for stabilization since an aluminium filter is used to block the IR co-propagating with the XUV.

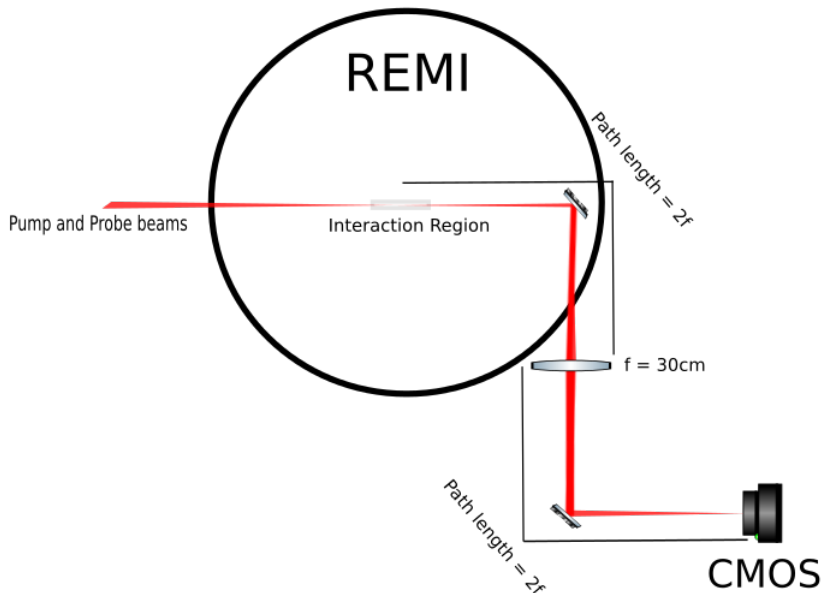


Figure 4.4: Imaging the focus inside the REMI with the help of a focusing lens, placed at $2f$ from the interaction region.

A focusing lens with $f = 30\text{ cm}$ is placed at a distance of 60 cm ($2f$) from the focus inside the REMI. With this arrangement, the focus inside the REMI is mapped onto the camera placed at 60 cm ($2f$) from the lens (Fig. 4.4). By overlapping the pump and probe beams on the camera image, the focii of the two beams inside the REMI overlap as well¹.

Following this, the length of the probe arm is adjusted to temporally overlap the two pulses. This is done using the retro-reflectors on the probe arm. These are mounted on a piezo translation stage, which is in turn coupled to a mechanical

¹To achieve a near-perfect spatial overlap for the XUV and IR beams, the ToF and y-position coordinates for the ions are used. This procedure is explained in Ref. [88]

translation stage. Coarse length adjustments to the probe arm are done using the mechanical translation stage, while the piezoelectric stage helps fine adjust the length and also to perform delay scans. A piezo stage from *Physik Instrumente* (PI) GmbH is used, providing a scan step resolution of 5 nm, with a range of 1.5 mm.

Once the main interferometer is aligned, the extended interferometer is adjusted to obtain fringes on the camera outside the recombination chamber. The piezo stage is then driven a few microns back and forth to check for correlated motion of the fringes on both cameras, to ensure a good temporal overlap of the pulses in both the interferometers. Particular attention is paid to the time of disappearance and appearance of fringes on both cameras to eliminate the possibility of fringes appearing in the extended interferometer from spurious reflections.

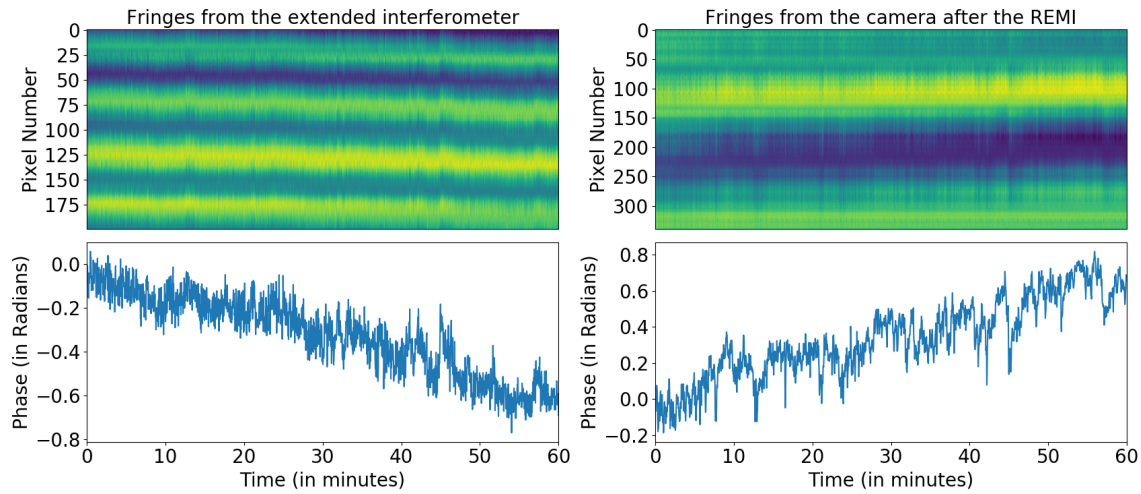


Figure 4.5: Tracking the interference signal from the extended interferometer and the actual interferometer

Once this is done, the vacuum chambers can be sealed and pumped to a very high vacuum, duly followed by the process of HHG and ionization of the gas jet in the REMI with XUV and IR. The path length and spatial overlaps are fine adjusted until the sideband peaks are visible in the photoelectron spectrum during the online analysis of the data. Once this done, the pump-probe measurement with stabilization can be carried out by performing scans using a self-written **Python** program, which also analyzes the interference fringes on the camera and uses it as feedback to compensate the drifts by adjusting the piezoelectric stage (Figure 4.6).

Program

A very concise description of the program is as follows:

- At the beginning of the experimental run an image is stored and the phase is measured. This acts as the reference.
- The interference fringes on the camera are tracked 20 times a second and compared to the reference phase.
- If the difference between the current phase and reference phase is greater than a threshold, then the program calculates the net path displacement required to get the interference fringes back to the reference phase and the piezo stage is moved accordingly.

The threshold for correcting the phase shift is chosen based on the resolution of the piezo translation stage.

In the experiments reported in this thesis, the piezo stage used offers a resolution of 5 nm. Since the probe beam passes through two reflections on the retroreflectors, the effective path length change attained by moving the piezo stage needs to be doubled. Taking this into account, the actual length resolution then is 10 nm. If the central wavelength of the laser beam is taken to be 1030 nm, this results in a resolution of 3.5 Degrees(0.06 Radians) in phase. This translates into a temporal resolution of ≈ 33 attoseconds.

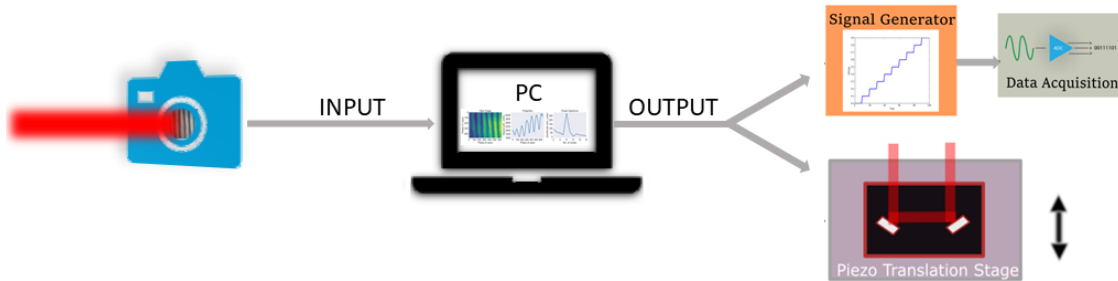


Figure 4.6: A schematic of the drift stabilization mechanism

The above mentioned method is used to hold the relative phase between the pump and probe beams close to one setpoint. In a pump-probe experiment however, the setpoint phase is continuously incremented at regular intervals of time so as to perform an XUV-IR Pump-Probe delay scan. As the reference/setpoint phase is incremented, so is the stage moved. The position of the piezo stage is mapped to the electron and ion momenta using an input to a channel on the ADC(*Analog to Digital Converter*) in the Data Acquisition System (see Fig. 4.6). The ADC can measure voltages between 0 to 4V with 1 mV resolution.

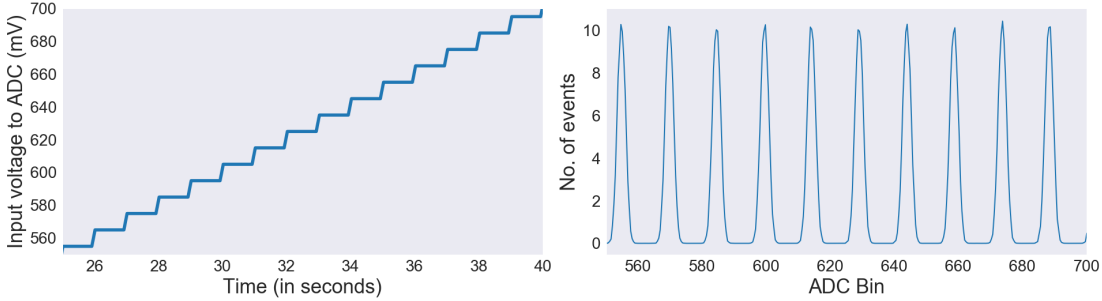


Figure 4.7: Left : Input voltage to the ADC as a function of time, Right : ADC readout

It converts the input voltage to a number between 0 and 4095 and maps all the ions and electrons detected to the respective bin value. Using the ADC input, the photoelectron spectrum corresponding to various delays is recorded. Since the XUV-IR phase is adjusted in discreet steps, the DC offset is also changed at regular intervals corresponding to the change in the setpoint phase. A plot of the ADC input as a function of elapsed time would then be a staircase function and the corresponding ADC readout will be a series of peaks (Fig. 4.7). It should be noted that the input voltage to the ADC is independent of the signal used to drive the piezo stage. In order to obtain best results, the phases are incremented in steps of at least twice the resolution offered by the stage i.e 20 nm steps (net displacement) corresponding to a net phase increment of 7 degrees (0.12 Radians). In the forthcoming sections, the actual precision this arrangement offers in an experiment will be discussed.

4.2.1 Tests with Drift Stabilization

In this section, some of the tests performed to characterise interferometer drifts would be discussed.

The first test was to observe if the drifts in the main interferometer and extended interferometer are correlated. This was done by placing a camera outside the REMI and observing the interference fringes simultaneously along with the fringes of the extended interferometer. The results of this test can be seen in Figure 4.5, in the previous section.

In figure 4.5, the movement of fringes on both cameras exhibit a correlation. The magnitude of drifts in both interferometers is almost equal, although they have opposite signs due to the difference in number of reflections. This test indicates that the fringes from the extended interferometer can be used as a reliable monitor of the drifts from the actual interferometer. The goal of the second test was to evaluate the stability of the interferometer with and without active stabilization. The results are seen in Figure 4.8. The camera image from the extended interferometer is used for this analysis.

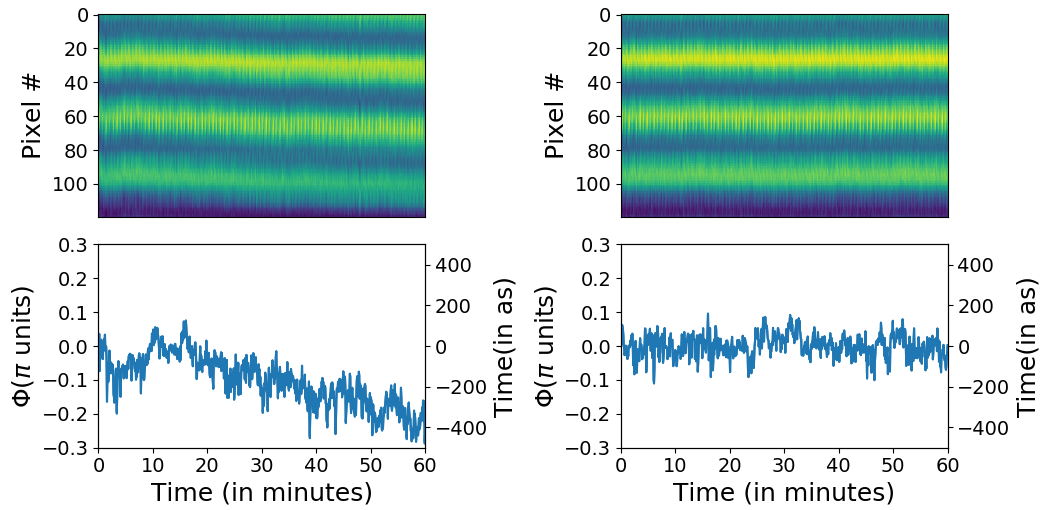


Figure 4.8: Left: Drifts from the unstabilized interferometer, Right: Drifts after locking the interferometer

Over the course of an hour, the interferometer drifted by about $\approx 0.25\pi$ radians. This corresponds to a temporal drift of ≈ 400 attoseconds. Upon locking the phase to one setpoint, the drift was negligible and only a ≈ 50 attoseconds "jitter" due to the high-frequency perturbations was observed. Repeated measurements with the stabilization returned jitter values in the vicinity of 50 attoseconds, indicating that the stabilization efficiently corrects the slow drifts happening over a few hours.

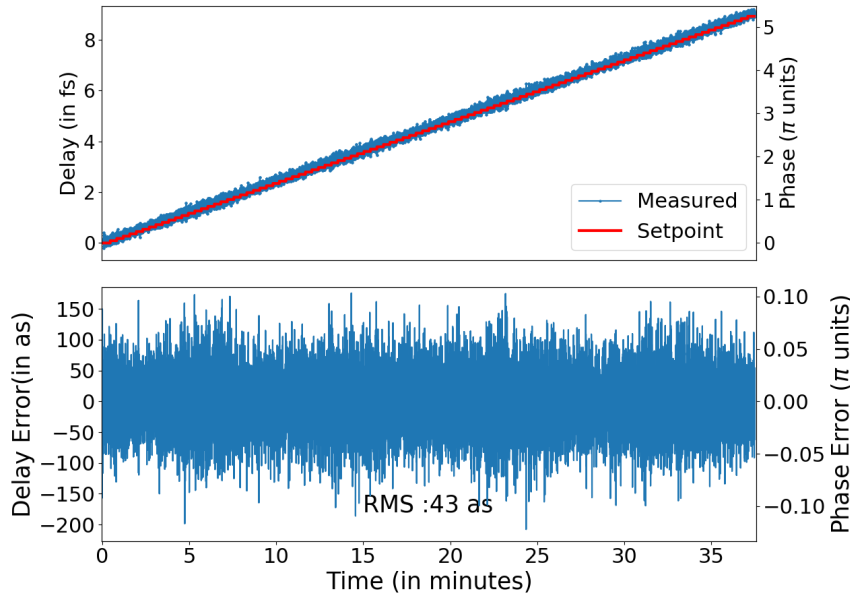


Figure 4.9: Delay Scan performed with the active stabilization

The third test involved continuously changing the setpoint phase at regular intervals of time to perform a delay scan. This was done by incrementing the setpoint phases by $\frac{\pi}{10}$ units until a net phase shift of 5π radians was reached and the drifts were corrected simultaneously. The results are shown in Figure 4.9. The RMS of the difference between the setpoint and the measured phase is **43 attoseconds**, which is only slightly more than the ultimate precision of 33 attoseconds offered by the movement of the piezo stage. The test was repeated thrice returning values less than 50 attoseconds, indicating that XUV-IR Pump-probe experiments can now be performed reliably with only a 50 attoseconds jitter.

Additional tests with higher step sizes ($\frac{\pi}{6}, \frac{\pi}{4}$ radians) also returned values within the 45-50 as range, indicating that the stability achieved is fairly independent of the step size chosen and the program works well enough to correct drifts happening over the course of a few hours.

Comparison with the old method

In the earlier iterations of the beamline, delay scans were performed by driving the piezo stage back and forth with a triangular wave from a function generator. The same signal would also serve as the ADC input, to map the stage position. This method is extremely easy to implement and is used in most femtosecond pump-probe experiments. However, there are a couple of drawbacks to this method, while performing scans over a delay range of 10 femtoseconds or lesser. Firstly, it assumes that the piezo stage responds linearly to the driving signal. This is not true especially at the turning points, due to the piezo stage's inertia of motion. Second, the ADC input signal is continuous and hence signal from consecutive bins overlap. This overlap results in a DC background in the sideband oscillations, thereby limiting the contrast that can be achieved.

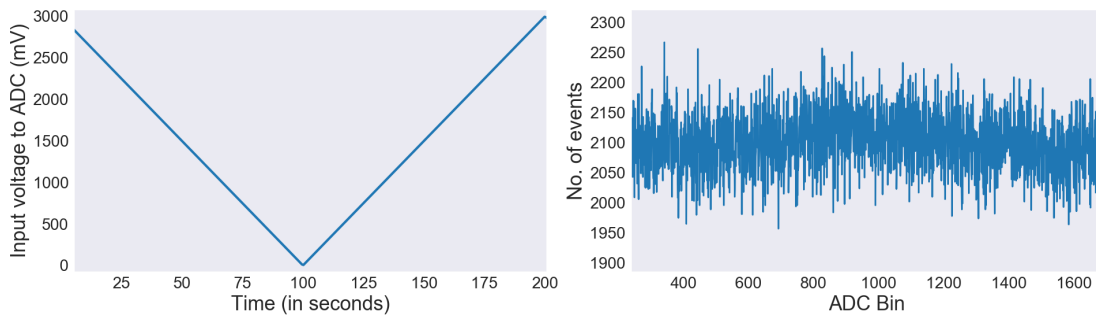


Figure 4.10: Left : Input voltage to the ADC as a function of time. The same signal was used to drive the piezo stage earlier, without active stabilization.
Right : ADC readout over several scans.

When active stabilization is used, the discrete ADC inputs ensure that data from each bin can be unambiguously identified and put together to construct RABBIT traces with a very good oscillation contrast.

4.3 RABBIT with Active Stabilization

So far, the stability of the interferometer was discussed by analyzing the interference pattern. To quantify the effects of the interferometer drift on a RABBIT trace, some measurements with and without stabilization were performed. A detailed quantification of the drifts for both short durations(lasting a few hours) as well as long durations(>12hrs) will be done in this section.

The RABBIT principle has been explained in Sect. 2.4. To give a quick recap, the sideband oscillations can be fitted with a simple cosine function:

$$I_{SB}(t) = A\cos(2\omega_{IR}\tau + \phi) + B \quad (4.3)$$

where the phase ϕ is a sum of ϕ_{XUV} - the intrinsic chirp of XUV pulses and ϕ_{atomic} - the atomic phase, A is the amplitude and B is the offset.

4.3.1 Short Duration measurements

The first set of tests included performing two sets of RABBIT measurements on Argon, one with active stabilization and one without (Figure 4.11). This was done in quick succession to prevent any effects of varying experimental parameters such as the laser's power output or spectrum.

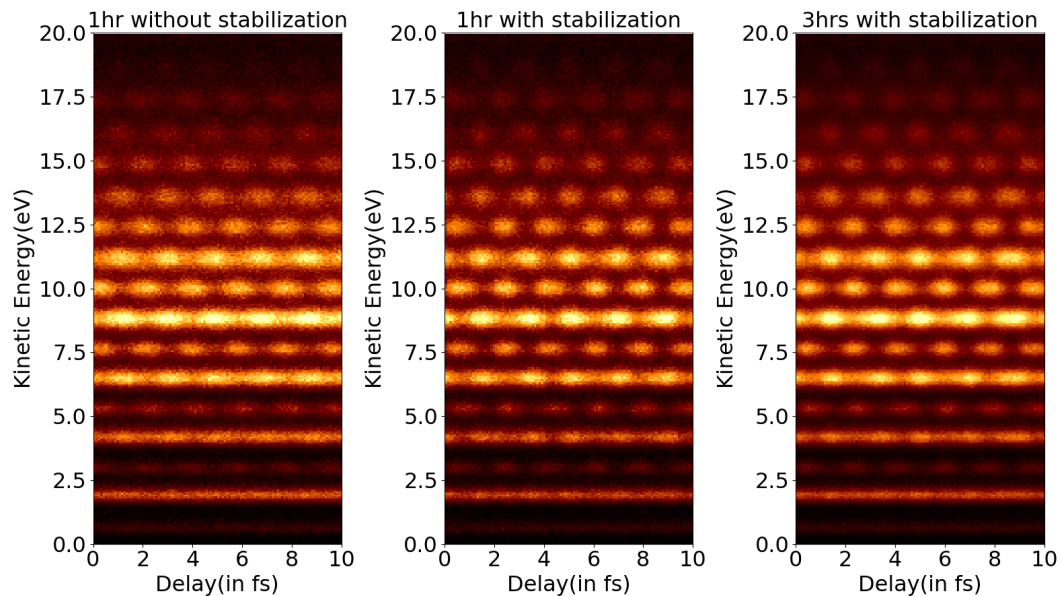


Figure 4.11: Comparison of RABBIT Spectrograms obtained with and without active stabilization

In the first measurement over an hour, the data were acquired by scanning the piezo stage back and forth without any stabilization. This was done using a triangular wave with a period of one minute as input for driving the piezo stage.

The second measurement lasted over three hours and the data was acquired by scanning with the active stabilization. Phases were increased in steps of $\frac{\pi}{20}$ and over a range of 6π radians. This gives 6 cycles of sideband oscillations in the RABBIT spectrum. The total delay range is calculated to be 10.2 fs and each scan from 0 to 6π lasted 15 min. Inspecting the spectrograms in Figure 4.11 and comparing, it is evident that the delay scans performed with stabilization result in a better contrast than those without stabilization.

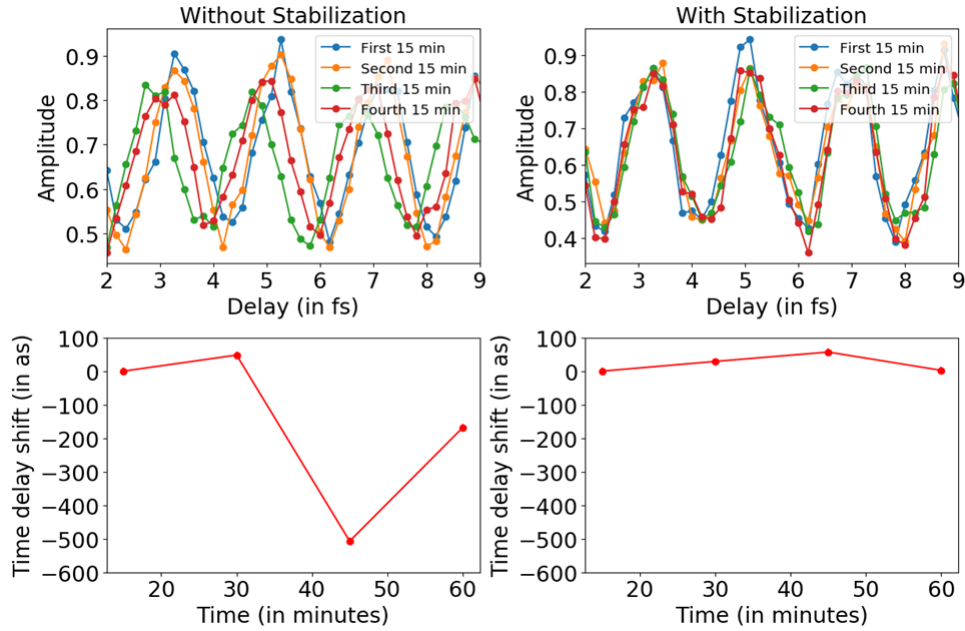


Figure 4.12: Quantifying the drift in sideband oscillation phases in a RABBIT measurement over 1 hour with and without stabilization. Top: Projections of the sideband oscillations (SB 22) for each 15 minute slice of the dataset. Bottom: Temporal drift with respect to the data from first 15 minutes.

To quantify drifts in the RABBIT trace over time, one sideband is chosen and tracked. This is done by dividing the data acquired over 1 hour into smaller segments of 15 minutes each. The projections of sideband oscillations from each of these segments are fitted with a cosine function as given in Eq. 4.3. In the projection plot (Fig. 4.12), for the unstabilized case, there is a clear phase shift in the sideband oscillations due to drift. Within 1 h, the unstabilized scan exhibits an average shift of about 200 attoseconds, whereas the stabilized scan exhibits a much smaller shift, at about 40 attoseconds. The data analyzed over three hours indicate an average shift of only about 60 attoseconds, indicating that this method indeed compensates for the slowly occurring thermal drifts over a few hours. Therefore, this set of measurements proves that very good stability can be achieved in the main interferometer even by monitoring drift on the extended interferometer.

4.3.2 Long Duration Measurements

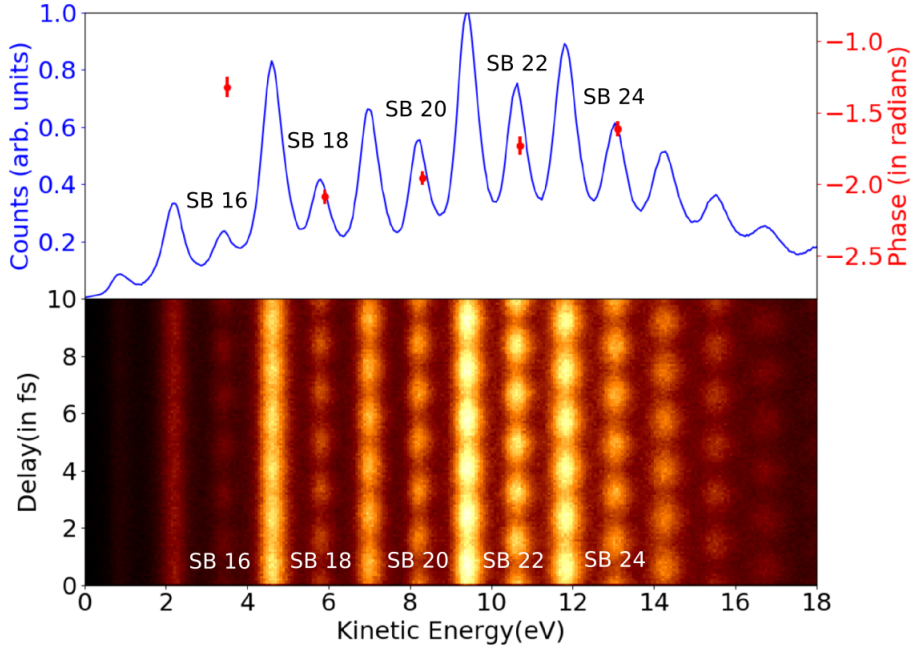


Figure 4.13: Bottom: RABBIT spectrum for photoionization of Argon, Top: Photo-electron spectrum integrated over all time delays and the respective sideband oscillation phases. The data was recorded over 13 hours.

Following this, ultimately two sets of RABBIT measurements lasting more than 12 hours were performed on Argon to look at the influence of drifts on long acquisition times. The RABBIT spectrogram from one of these runs is shown in Fig. 4.13. The sideband oscillation phases shown in Fig. 4.13 were obtained by fitting a cosine function to the projections of the sideband oscillations. Data were recorded for 13 hours and no additional corrections were made to the data set. The variation of the sideband oscillation phases over time is shown in Fig. 4.14. The phase estimated from the data of the first 1 hour is taken as the reference. The mean change is estimated to be ≈ 300 attoseconds over 12 hours.

This set of measurements indicates that over a few hours, the drift in the sideband oscillations is negligible and does not affect their contrast. However, when data is acquired for more than 12 hours and the data is added up, it leads to a slight reduction in the contrast of oscillations (Fig. 4.15). Since the drift is less than $\pi/2$ units of phase over about 12 hours, slices of data for 6 to 8 hours can be taken and corrected for drifts and put together, if required. This becomes particularly useful in analyzing dissociation processes in molecules, where events in the dissociation channel are typically 1% of events in the single-ionization channel that require long acquisition times.

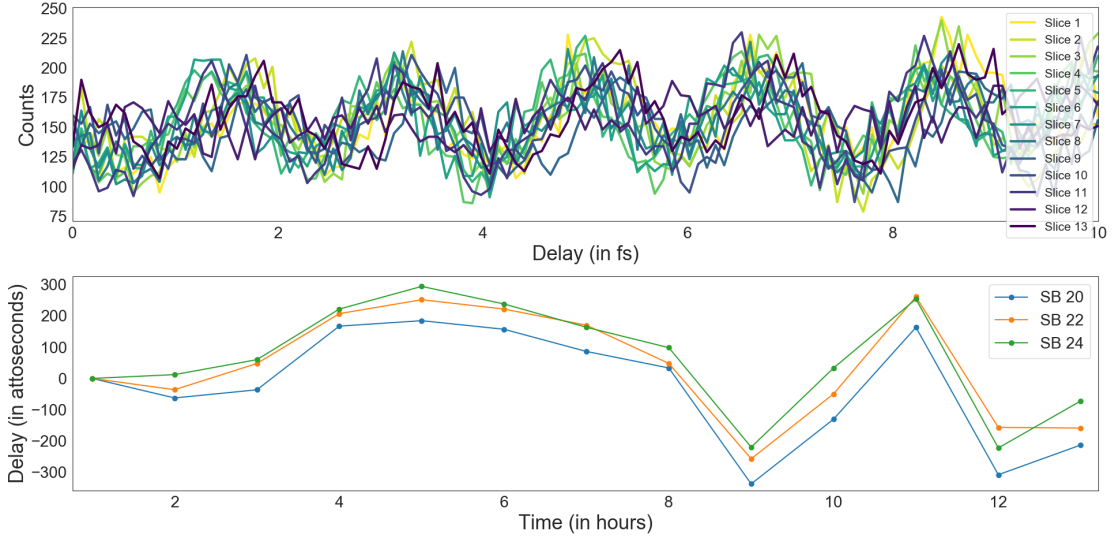


Figure 4.14: Top: Projections of SB22 from each 1 hour slice, Bottom: Drift of the sideband oscillations in SB20 - SB24 over 12 hours

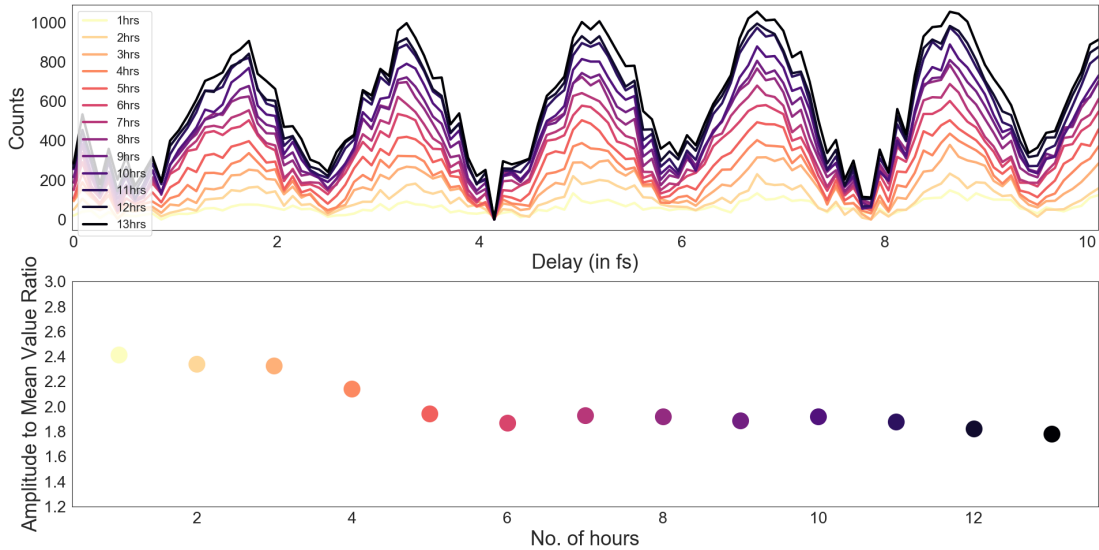


Figure 4.15: Top: Build-up of signal in sideband 22 over 13 hours, obtained by adding the sideband oscillations, Bottom : Change in sideband oscillation contrast upon adding data over time

The inability to completely eliminate drifts in the RABBIT traces in spite of using drift stabilization has two main reasons. First, fluctuating laser pulse energy and spectrum result in varying phase-matching conditions for generating XUV pulses through HHG. This affects the spectral width of the harmonics and also the XUV chirp (Fig. 4.14), both of which play a role in the contrast of sideband oscillations [100, 101]. Intensity fluctuations of even 5% can reduce the

temporal accuracy of the measurement by as much as 60%, as explained in the reference[100].

Second, due to beam-pointing instabilities, the overlap of XUV and IR foci inside the REMI can change with time due to a small beam walk-off. For any focused beam, the light wave exhibits a π radian phase shift as it passes through the focus, which is termed the Gouy phase shift[27, 102]. When the focus of the probe IR changes due to a beam walk-off, the sideband oscillation phases are affected by these Gouy phase variations. For every millimeter of focus shift, the measured delay from a given sideband can change by 50 attoseconds[103]. Therefore for measurements performed over several hours this is inevitable, unless the beam pointing is also stabilized.

To conclude, the drifts of the interferometer have been characterized and its effect on the sideband oscillations discussed in this chapter. Active stabilization successfully compensates for slow thermal drifts that occur over a few hours. For experiments lasting a few hours, the data can therefore be directly analyzed without any corrections. For measurements lasting 12 hours or more, the sideband oscillations exhibit minor shifts, due to the influence of factors such as laser power and spectrum variation, and Guoy phase shifts due to beam-pointing instabilities.

To improve the stability of the interferometer, the following factors can be considered:

1. Piezo stage - The piezo stage used in this measurement is one of the main factors that imposes a close to 50 attosecond jitter. Using a stage that offers a better resolution (about 2nm or less) can help reduce the jitter even further.
2. Camera - The second is the CMOS camera used to monitor the fringes. A faster camera readout would also help in sampling many more images per second and might help correct the faster movements occurring over a few seconds. However, this is a computationally intensive task and would require a sophisticated method for image acquisition and processing.
3. Beam Pointing - Finally, a beam-pointing stabilization can be coupled to the existing setup to reduce the impact of spatial shifts of the beams.

In addition to the RABBIT measurements presented here, active stabilization was also successfully used to perform novel 3-Sideband RABBIT measurements[104]. In these measurements, the sidebands oscillate with a period of 850 attoseconds and hence low jitter and drift are required to ensure that the sideband oscillations are visible, even on short timescales. In the following chapters, measurements performed on argon dimers and Krypton atoms with active stabilization will be discussed.

5 Angle-resolved RABBIT measurements on Krypton

In this chapter, RABBIT measurements performed on Krypton will be discussed to study the influence of spin-orbit splitting on photoionization delays. So far, two RABBIT measurements on Krypton have been reported in [105, 106] that study the influence of spin-orbit splitting on photoionization delays. Both measurements used electron spectrometers that integrate signals from electrons emitted along all directions. There have also been additional reports of XUV-IR pump-probe measurements on Krypton (Refs. [107],[108]) where a Velocity-Map Imaging Spectrometer[109] was used to detect the electrons. In the former case (Ref. [107]), the photoelectron angular distribution was measured over a delay range of several hundred femtoseconds. The latter measurement, although performed over a sub-50-fs delay range, does not resolve the spin-orbit splitting except for the first one or two orders of the harmonics and also does not delve into the angular distributions of photoelectrons.

With this background, a Krypton measurement was performed with a Reaction Microscope to look for any angle-dependent variations that can be attributed to spin-orbit splitting and / or intershell correlations.

5.1 Spin-Orbit splitting in XUV ionization of Krypton

The fine-structure[9] that is observed in atomic spectra is explained by corrections to the Hamiltonian of an atomic system, taking into account the relativistic effects. There are two terms that play an important role for atomic systems that do not have valence s electrons . The first one is obtained by considering the relativistic motion of the electron. This is essentially a relativistic correction term for the kinetic energy of electrons. The second is obtained by considering the motion of the nucleus from the electron's frame of reference. The interaction between the electron's intrinsic angular momentum (Spin) and the magnetic moment obtained from the current loop caused by the nuclear motion with respect to the electron causes the spin-orbit coupling. It scales non-linearly with the atomic number($\propto Z^4$) and particularly for multi-electron atoms, the spin-orbit coupling dominates the energy correction terms[9]. For noble gases heavier than argon, this leads to a significant split in the energy levels(ΔE_{SO}) of electrons. With the help of sufficiently narrowband XUV radiation along with a photoelectron spectrometer that provides optimal resolution, we can obtain a photoelectron spectrum with two distinct peaks arising from the $P_{\frac{3}{2}}$ and $P_{\frac{1}{2}}$ levels of the ionic core.

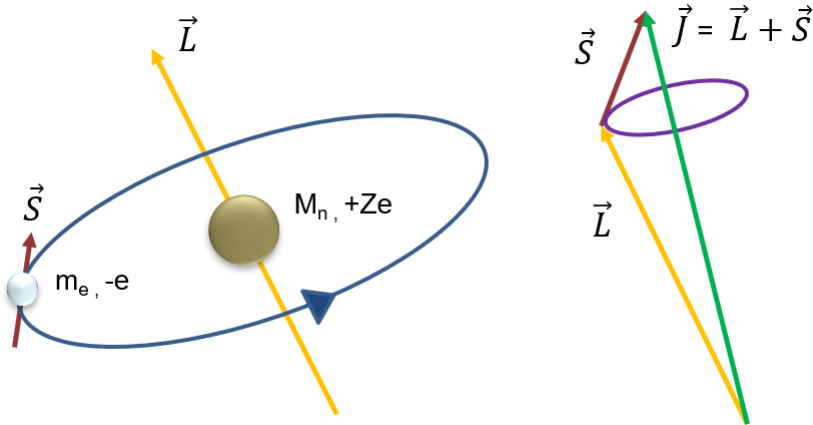


Figure 5.1: Pictorial representation of the Spin-orbit coupling. Left - electron in a classical orbit around the nucleus, Right - Vector addition of the orbital angular momentum and spin.

When a comb of frequencies forms the XUV radiation that ionizes the atom, the resulting photoelectron spectrum comprises a sequence of pairs of peaks (Fig. 5.2). Within each pair, the spacing is ΔE_{SO} and the spacing between each of the $P_{\frac{3}{2}}(P_{1/2})$ peaks is $2\omega_{IR}$. In the case of Krypton ($Z = 36$), the spin-orbit split in energy is around $\Delta E_{SO} \approx 0.67$ eV [110] and hence there are two ionization thresholds - 14.0 and 14.67 eV for the components $P_{3/2}$ and $P_{1/2}$, respectively. Therefore, photoelectrons ejected with different kinetic energies tend to experience considerably different ionic core potentials, which in turn influences the phases of the outgoing electron wavepackets in a non-trivial manner[105].

In Fig. 5.2, the photoelectron spectrum of the ionization of Krypton atoms with XUV radiation is seen. The $P_{\frac{3}{2}}$ peaks are close to twice the strength compared to $P_{\frac{1}{2}}$ due to the different bound-continuum transition probabilities[9]. The peaks are well resolved up to an electron kinetic energy of 16 eV (≈ 30 eV photon energy). At higher kinetic energies, the spectral lines start to overlap because of a poorer resolution. The spectrum was recorded with a spectrometer acceleration voltage of 136V along with a magnetic field of 9.5 Gauss. The same parameters were used for the RABBIT measurements on Krypton, which are presented in the following section.

5.2 RABBIT measurements on Krypton

5.2.1 Experiment and Data Analysis

The spacing between two $P_{\frac{3}{2}}(P_{\frac{1}{2}})$ peaks in the XUV ionization spectrum is 2.4 eV, and in the presence of IR after XUV ionization, sidebands are formed at 1.2 eV

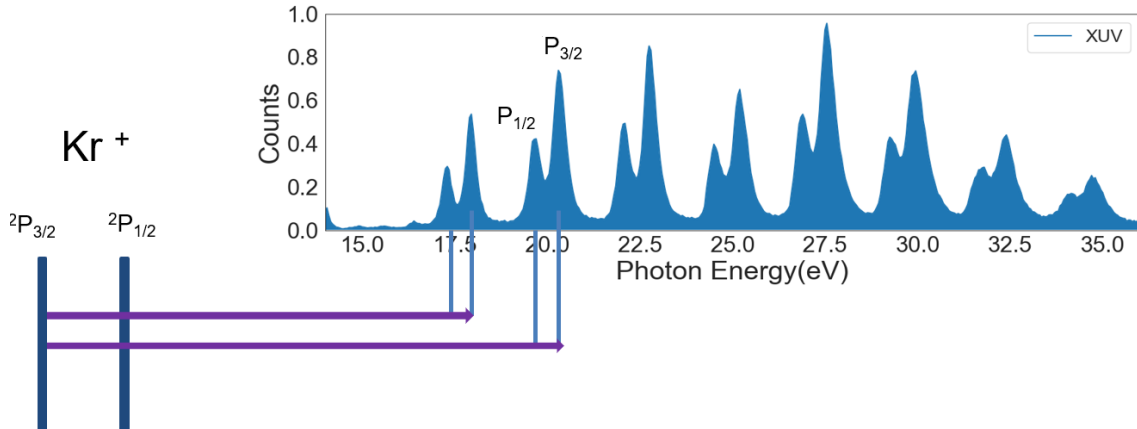


Figure 5.2: Photoelectron Spectrum of Krypton ionized by XUV radiation. The spectrum is obtained by integrating the photoelectron signal for electron emission angles between $0 - 65^\circ$ w.r.t respect to spectrometer axis.

between two consecutive $P_{\frac{3}{2}}(P_{\frac{1}{2}})$ peaks. When the harmonics and sidebands overlap, it is extremely difficult to observe any sideband oscillations because of the dominant background signal from the XUV ionization.

In the case of Krypton, as seen in Fig. 5.3 the sidebands do not overlap significantly with the harmonics for ionization up to 30 eV photon energy. It should be noted here that only electrons emitted along an angle $0^\circ - 65^\circ$ with respect to the spectrometer axis are considered here for analysis. This is done to minimize the spectral overlap between the photoelectron peaks due to the suboptimal resolution of the electrons emitted between $65^\circ - 90^\circ$.

The data was recorded for 15 hours with active stabilization implemented. Delay scans were performed over a range of 10 femtoseconds. Each scan lasted 2 minutes. The data were split into 1 hour slices each and analyzed individually to look for any possible slow drifts that might occur despite using the active stabilization. The data from these scans where the sideband oscillation contrast was poor were rejected, while the rest of them were put together.

The RABBIT scan is shown in Fig. 5.4 (left). As can be seen, the RABBIT trace consists of pairs of sidebands that oscillate. Additionally, the electrons coming from the ionization of XUV alone (harmonics) exhibit an oscillation as well. To visually separate the two, a 2D histogram is generated by plotting the photoelectron spectrum from ionization with XUV as a function of delay. In the absence of any probe beam, the spectrum does not modulate and remains constant. When the two spectra are visually compared, the sidebands and harmonics can be identified.

In order to resolve photoionization delays that would be only a few tens of attoseconds in this experiment, it is critical to identify and isolate any spectral overlap of the harmonics with the sidebands. Not only is the signal-to-noise ratio

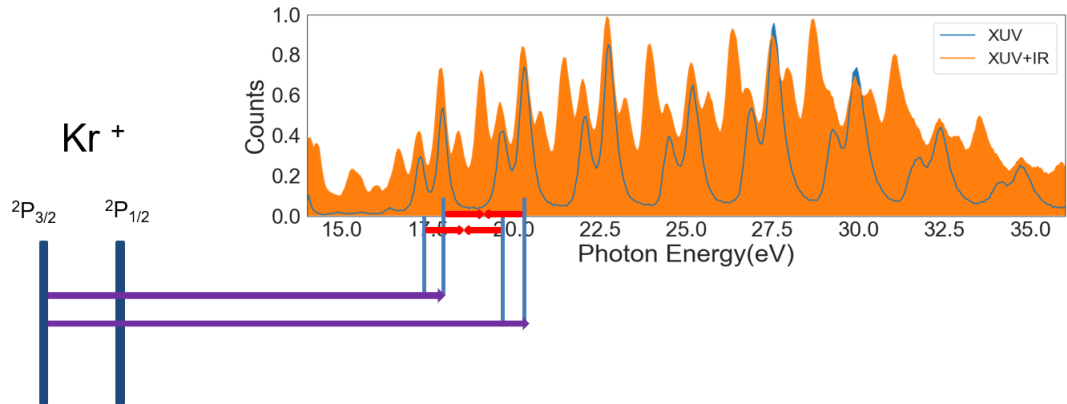


Figure 5.3: Formation of Sidebands in Krypton. The $P_{\frac{3}{2}}$ levels from neighbouring harmonics lead to the formation of corresponding sidebands. The same happens with the $P_{\frac{1}{2}}$ levels as well.

of the sideband oscillations significantly affected by the overlap, but it could also lead to rapid phase variations within the sideband itself. The identification of regions with large phase variations can be done with the help of an FFT spectrogram (explained in Chapter 2). The spectrogram is obtained by doing a linewise Fast Fourier Transform for each kinetic energy bin on the RABITT histogram, along the delay axis. The resulting spectrogram then displays the various frequency components of the sideband oscillations. Fig. 5.5 is one such example. As can be seen, the $2\omega_{IR}$ component is the strongest. The absence of higher frequencies ($\geq 4\omega_{IR}$) indicates that the intensity of the probe IR was low and did not induce multiphoton transitions in the continuum. By choosing a frequency window centered on $2\omega_{IR}$, the phase variation is obtained for each energy bin using the arc-tangent function.

In Fig. 5.5, it can be seen that the harmonics oscillate at roughly π radians out of phase with respect to the sidebands, and in places where they overlap there are large variations in phase. Using such FFT spectrograms, energy windows can be selected where there are no rapid phase variations for the sideband oscillations. When these energy windows are integrated, projections on the delay axis are obtained (Fig. 5.6). These projections are then fitted with a cosine function (described in 2.3), which gives the average phase and the standard deviation (σ). Figure 5.7 contains the phases so obtained. The phases are then converted to time delays using the relation $\tau_{SB} = \frac{\phi}{2\pi}\tau_{2\omega_{IR}}$, where ϕ is the phase in radians. Then, the time delay for the $P_{1/2}$ electrons is subtracted from that of the $P_{3/2}$.

$$\tau_{3/2} - \tau_{1/2} = \frac{\phi_{3/2} - \phi_{1/2}}{2\omega_{IR}} \quad (5.1)$$

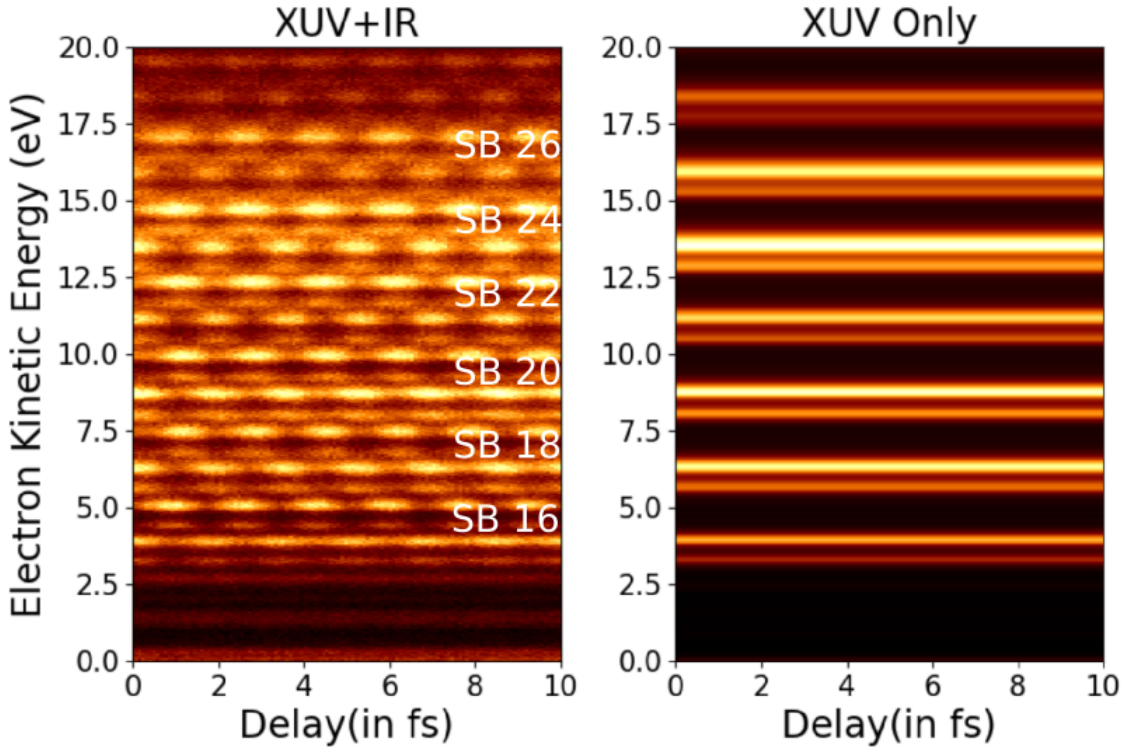


Figure 5.4: Left : Experimental RABBIT trace for Krypton, Right: Spectrum for the electrons coming from the ionization of XUV alone v/s Delay

5.3 Angle-averaged Results

In fig. 5.7, we have the sideband oscillation phases for the $P_{3/2}$ and $P_{1/2}$ components and the corresponding delay differences for each sideband. The time delay differences for most sidebands are only of the order of ± 10 attoseconds, except sideband 20 which is about +27 attoseconds. The observed trend is similar to the data presented in [106].

The atomic delay depends on the kinetic energy of the electron, as $\tau_{atomic} \propto \frac{1}{E^{3/2}}$ [52, 111]. Low-kinetic energy electrons exhibit large atomic delays, since they interact with the atomic potential for a longer time and hence experience larger phase shifts. Near the threshold, the atomic delays for the $P_{3/2}$ and $P_{1/2}$ components have a significant difference due to the low electron kinetic energies. Electrons of very low energy (< 3 eV KE) coming from ionization close to the threshold could not be studied in this experiment due to the use of aluminum filters to separate XUV from IR after HHG. The transmission edge of the aluminum filter opens up at about 18 eV[112], and therefore the signal for electrons with kinetic energies less than 3 eV is extremely weak.

SB 16, SB 18 : In SB 16, a negative delay difference of about 5 attoseconds is observed. The delay difference is negative due to the larger Wigner delay expe-

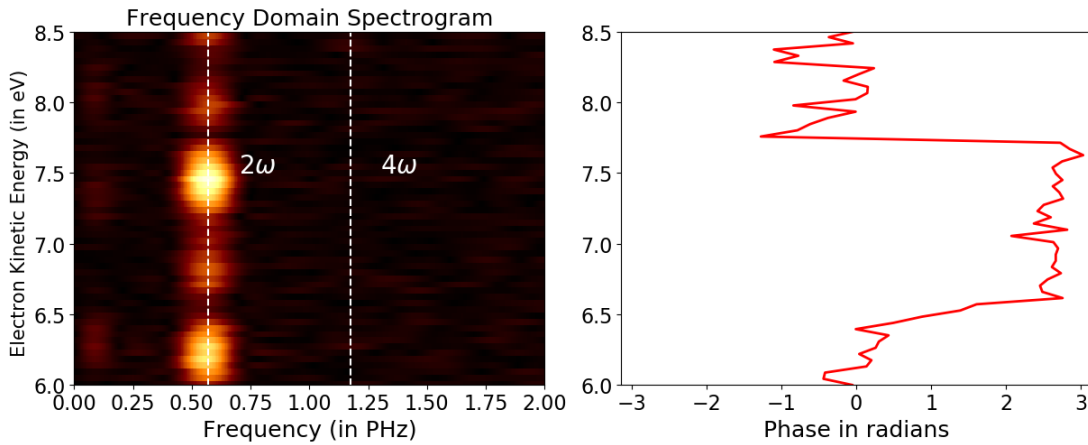


Figure 5.5: Left : Spectrogram obtained by performing a linewise Fast Fourier transform along the delay axis for each kinetic energy bin, Right : Phases estimated from the Fourier Transform

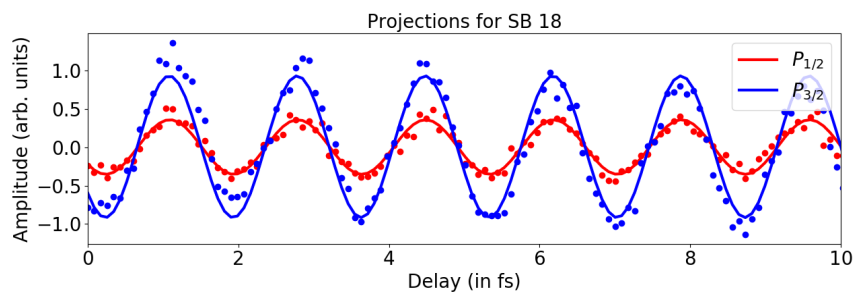


Figure 5.6: Projections of the sideband oscillations for SB 18. These projections were obtained by choosing the energy windows 7.2–7.6 eV and 6.6–6.9 eV in Fig.5.5 for the $P_{3/2}$ and $P_{1/2}$ electrons respectively.

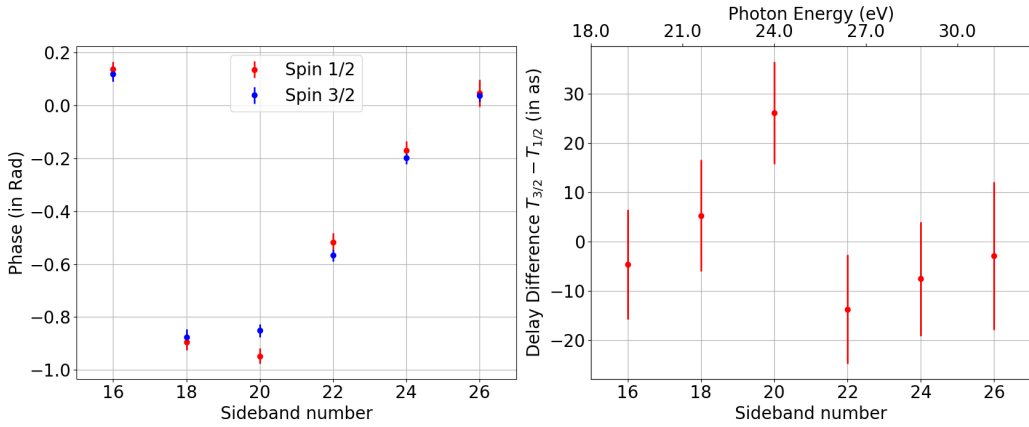


Figure 5.7: Left: Phases of sideband oscillations. Right: Difference in time delays for the electrons from the $P_{3/2}$ and $P_{1/2}$ levels

rienced by the $P_{1/2}$ electron. As the kinetic energy of the electron increases, the values τ_{Wigner} and τ_{CC} converge to zero[52]. For photon energies between 19-22 eV, the delay difference is close to zero.

SB 20, SB 22: A series of autoionizing resonances ($4s^14p^6np$) [113] in Krypton can be reached by using photons with energies between 24-28 eV. These are highly excited but short-lived states. They are the lowest inner shell Rydberg states and result in $4s^24p^6 \rightarrow 4s4p^6np$ ($n = 5, 6, 7, 8$) transitions. Harmonic 21, with a photon energy of 25.2 eV (Fig. 1.10) covers a number of resonances in the $4s4p^65p$ series, which were previously identified in synchrotron measurements (Fig. 5.9) [114, 115]. These resonances decay through autoionization into the ϵs and ϵd continua, as shown in Fig. 5.10. In the vicinity of these resonances, the $4p \rightarrow \epsilon d$ and $4p \rightarrow \epsilon s$ cross sections vary rapidly, which in turn influences the Wigner delay τ_{Wigner} . The variation of Wigner delay and atomic delay across resonances has been measured by earlier RABBIT measurements on argon[66, 116]. Harmonic 21 leads to the formation of sidebands 20 and 22, through the absorption or emission of an IR photon. Due to this, a significant delay difference was measured for sidebands 20 and 22. For sideband 20, the delay difference is about +27 attoseconds, while for sideband 22 it is -15 attoseconds. The origin of this significant difference in atomic delays will be discussed in detail in the following section, where the angular distribution of the electrons provides further insight into the various transition pathways involved.

SB 24, SB 26: As the photon energy increases, we move further away from the resonances. The $4s4p8p$ resonances at 27 and 27.2 eV, are not covered by the bandwidth of harmonic 23, with a photon energy of 27.6 eV. Moreover, as seen in Fig. 5.9, the $4s4p^68p$ is a relatively weak resonance and therefore does not significantly affect the phases of SB 24 and SB 26. Therefore, the difference in atomic delays for the $P_{3/2}$ and $P_{1/2}$ cases is less than 10 attoseconds.

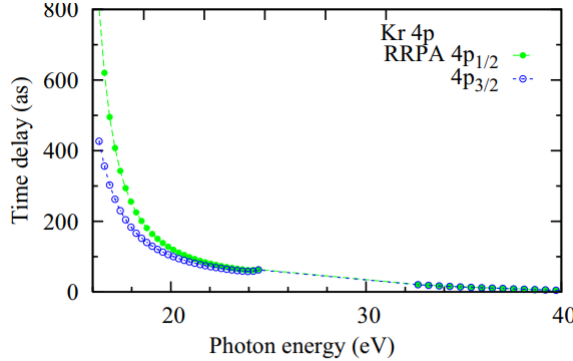


Figure 5.8: Theoretically calculated τ_{Wigner} values for the $4p_{3/2}$ and $4p_{1/2}$ electrons. There are no data points calculated between 24 to 32 eV photon energy, due to the presence of $4s4p^6np$ resonances. Figure taken from [111].

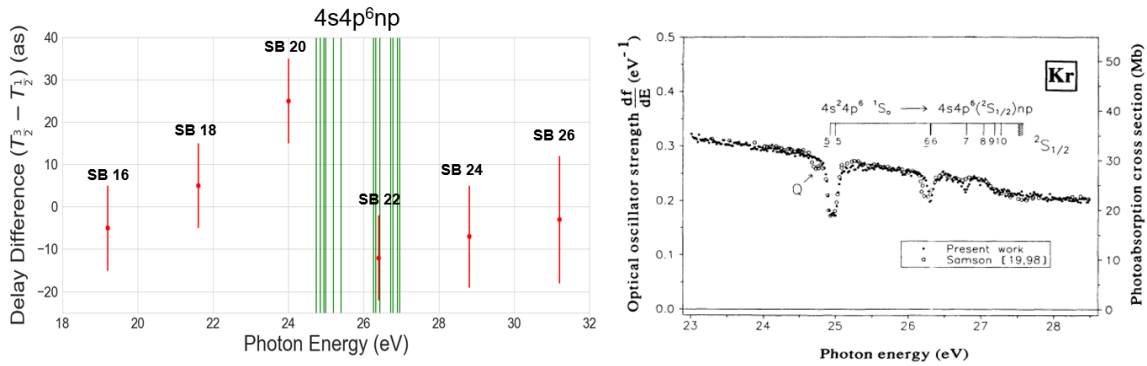


Figure 5.9: Left : Delay differences for the $P_{3/2}$ and $P_{1/2}$ electrons. Green lines indicate $4s4p^6np$ ($n=5,6,7,8$) resonances. The data for resonances is taken from [117]. Right: Experimentally observed $4s4p^6np$ resonances. Figure taken from [118].

5.4 Angle-resolved time delays in Krypton

The oscillation phases for sidebands 20 and 22, indicate that the resonance $4s4p^65p$ plays an important role in the measured photoionization delays. To better understand the influence of the resonance on atomic delays, we look at the angular distribution of photoelectrons. Moreover, by comparing the sideband oscillation phases as a function of the angle of emission, we obtain additional insights into the bound-continuum transition pathways. This method of analyzing the phases as functions of the emission angle is also known as angle-resolved RABBIT and has been the central theme of several RABBIT measurements in recent years (e.g. [66, 119]). The angle-resolved analysis is restricted to electrons with longitudinal momentum between -1 atomic units and 0 atomic units, due to a magnetic field node (Sec. 3.3.3) for electrons having a longitudinal momentum (p_{long}) greater

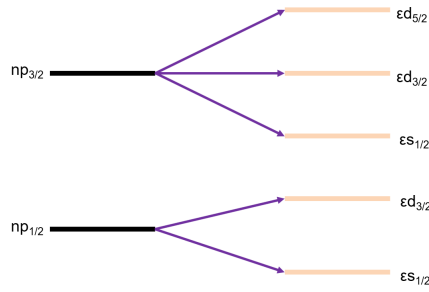


Figure 5.10: Transitions arising from XUV ionization, from a bound np state to $\epsilon d, \epsilon s$ states in the continuum for the $P_{3/2}$ and $P_{1/2}$ ionic states.

than 0.

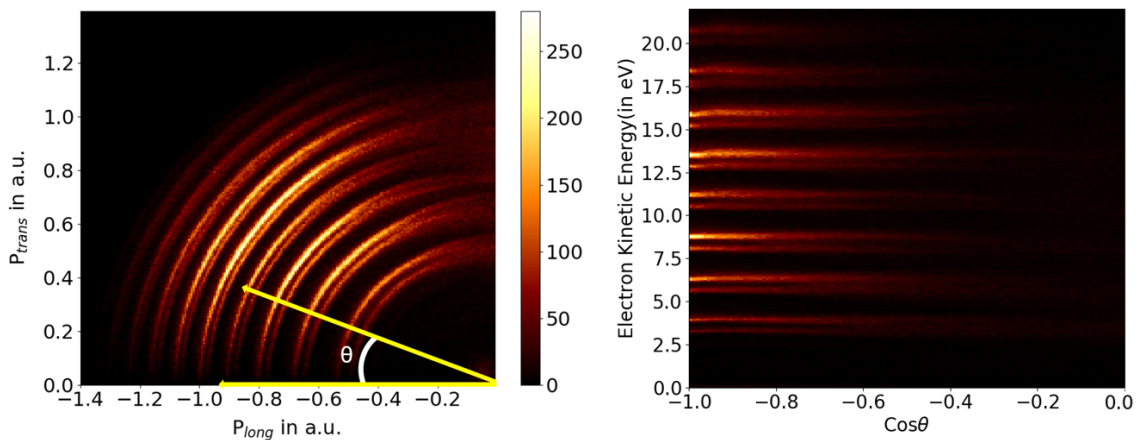


Figure 5.11: Left : Momentum distribution of the electrons along the longitudinal and transversal direction, upon ionization by XUV. Right : Electron kinetic energy v/s cosine of the angle of emission.

5.4.1 Analysis of β parameters

The ReMi provides complete 3-dimensional momentum information for the electrons. The angular distribution of the electrons can be obtained using the longitudinal and transversal momentum components (Fig. 5.11). To measure angles, a reference axis is necessary. In this case, the polarization axis of the laser is chosen. Therefore, the angle of emission with respect to the polarization axis can be calculated for each detected electron. When the laser polarization axis is aligned with the spectrometer axis, the angle of emission can be calculated using the following formula.

$$\theta = \cos^{-1}\left(\frac{P_{long}}{\sqrt{P_{long}^2 + P_{trans}^2}}\right) \quad (5.2)$$

The signal collected on the detector is proportional to the solid angle at which the electrons are emitted. When plotting the angular distribution of the electrons, the electron counts are very low for angles close to zero. To eliminate this effect, the data can be further reorganized to obtain a distribution of the electron kinetic energy as a function of $\cos\theta$ [120]. The angular distribution of photoelectrons ionized by linearly polarized light exhibits azimuthal symmetry and can be expressed as [66, 121, 122]:

$$\frac{d\sigma}{d\Omega} = \frac{\sigma_{total}}{4\pi} \left[1 + \sum_{i=1}^{2l} \beta_i P_i(\cos\theta) \right] \quad (5.3)$$

where $\frac{d\sigma}{d\Omega}$ is the partial cross section over a solid angle $d\Omega = \sin\theta d\theta d\phi$ (ϕ - azimuthal angle), σ_{total} is the total cross section, β_i is the asymmetry parameter and $P_i(\cos\theta)$ is the Legendre polynomial of order i . The parameter β takes a value between $[-1, 2]$, indicating whether the emission is parallel to the polarization axis ($\beta = 2$) or isotropic ($\beta = 0$) or perpendicular to the polarization axis ($\beta = -1$). In single-photon ionization the bound-continuum transitions follow the $\Delta l = \pm 1$ rule and are expressed by the second term in the expansion of the Legendre polynomial($P_2(\cos\theta)$). Therefore, for XUV ionization, we have:

$$\frac{d\sigma}{d\Omega} = \frac{\sigma_{total}}{4\pi} \left[1 + \beta_2 \left(\frac{1}{2} (3\cos^2\theta - 1) \right) \right] \quad (5.4)$$

In the presence of an additional IR photon after XUV ionization, the fourth term in the Legendre expansion($P_4(\cos\theta)$) contributes to the expression of the angular distribution.

$$\frac{d\sigma}{d\Omega} = \frac{\sigma_{total}}{4\pi} \left[1 + \beta_2 \left(\frac{1}{2} (3\cos^2\theta - 1) \right) + \beta_4 \frac{1}{8} (35\cos^4\theta - 30\cos^2\theta + 3) \right] \quad (5.5)$$

By fitting the angular distribution of electrons for each harmonic or sideband with the polynomials above, the experimental values of the β_2, β_4 parameters can be obtained as shown in Fig. 5.12. The parameters β_2 obtained from the XUV ionization of Krypton are compared with the data from the synchrotron measurements in Fig.5.13. The beta parameter increases with the electron kinetic energy, in good agreement with the trend observed in synchrotron measurements. For low kinetic energies, the electrons are strongly scattered by the ionic core and hence exhibit a high angular isotropy in emission, leading to a value of β_2 close to 0. As the kinetic energy increases, the probability of scattering decreases and the angular distribution of the outgoing electron depends on the ionization channel that dominates (ie $4p \rightarrow \epsilon s$ or $4p \rightarrow \epsilon d$). Electrons are therefore preferentially emitted along the polarization axis of the XUV as their kinetic energy increases.

In the vicinity of the resonance $n = 5$, the beta parameter varies significantly from the continuous upward trend. The beta parameter for the $P_{1/2}$ electron is much lower than that of the $P_{3/2}$ electron. This is due to the strong interference between the s and d ionization channels. At the lower energy end of the

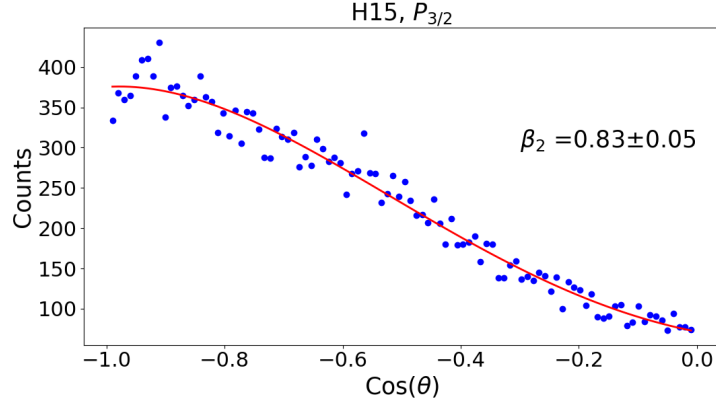


Figure 5.12: Blue: Angular distribution of the $P_{3/2}$ electrons ionized by harmonic 15, Red: Legendre polynomial fit. The details of the fit and the individual plots for each harmonic are provided in Appendix A.

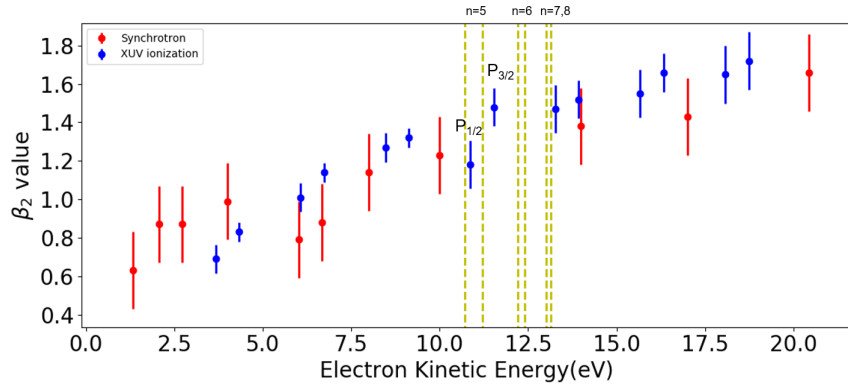


Figure 5.13: Experimentally obtained β_2 parameters for Krypton. Blue points: XUV ionization of Krypton. Red points: Synchrotron measurements reported in [123]

resonance, s-wave ionization is suppressed, while d-wave ionization is strongly enhanced[124, 125]. This results in a sharp increase in the parameter β_2 . At the higher energy end of the resonance, the opposite occurs, where the s-wave contribution is much stronger, resulting in a sharp decrease in the β_2 parameter.

In Krypton, due to spin-orbit splitting, the level $P_{3/2}$ has a lower ionization threshold than the level $P_{1/2}$. When autoionization occurs between these two levels, the decrease in the β_2 value is more significant for the $P_{1/2}$ electron due to a dominant s wave at the higher energy end of the resonance (Fig. 5.14). The value of β_2 does not vary significantly for the resonances of $n = 6, 7, 8$, as the cross-sectional variation decreases with increasing value of n in the Rydberg series.

The variation of the β_2 value for harmonic 21 indicates that the difference in

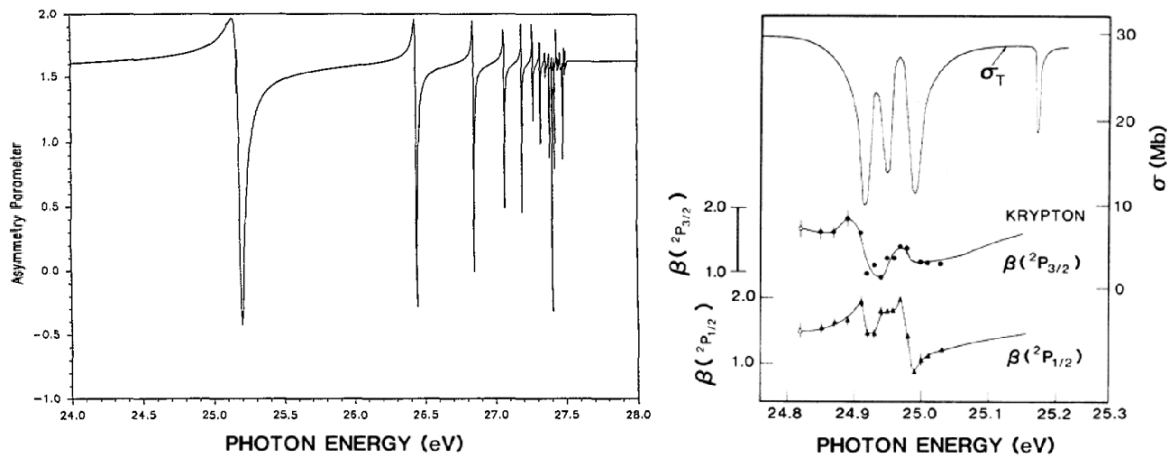


Figure 5.14: Left: Theoretically calculated variation of the asymmetry parameter in Krypton, for single photon ionization around the $4s4p^55p$ resonances. Figure taken from [118]. Right: Top: Theoretically calculated total ionization cross section variation, Bottom : Experimentally measured variation of β_2 values around the $n=5$ resonance. Figure taken from [114]

photoionization delays for the two components of the spin orbit will depend on the angle of emission, since the s and d waves do not have the same strengths for the outgoing electrons from the two levels.

5.4.2 Angle dependent spin-orbit delays

To evaluate the difference in spin orbit delays as a function of the angle of emission, the electrons emitted between 0° and 65° (Fig.5.15) with respect to the polarization axis are chosen and divided into 'angular slices' e.g. 0° to 8° , 8° to 16° and so on. The RABBIT traces for each of these slices are then generated and the sideband oscillation phases are evaluated as explained in Sect. 5.2.1. The phases evaluated for sidebands 16 to 22 are shown in Fig.5.16. Sidebands 24 and 26 are excluded from the analysis due to very large error bars.

The spin-orbit delays for sidebands 16 and 18 show no variation as a function of the angle, due to the lack of resonances in the vicinity of harmonics 15,17 and 19. However, sidebands 20 and 22 show a significant variation as a function of angle due to the influence of $n = 5$ resonances in the vicinity of Harmonic 21. The delays in this region depend strongly on the contributions of each partial wave and hence show a stronger angular dependence.

To understand this variation, we need to look at the mathematical expressions derived in [106, 111], used to calculate the delays $\tau_{3/2}$ and $\tau_{1/2}$ for $P_{3/2}$ and $P_{1/2}$ components respectively.

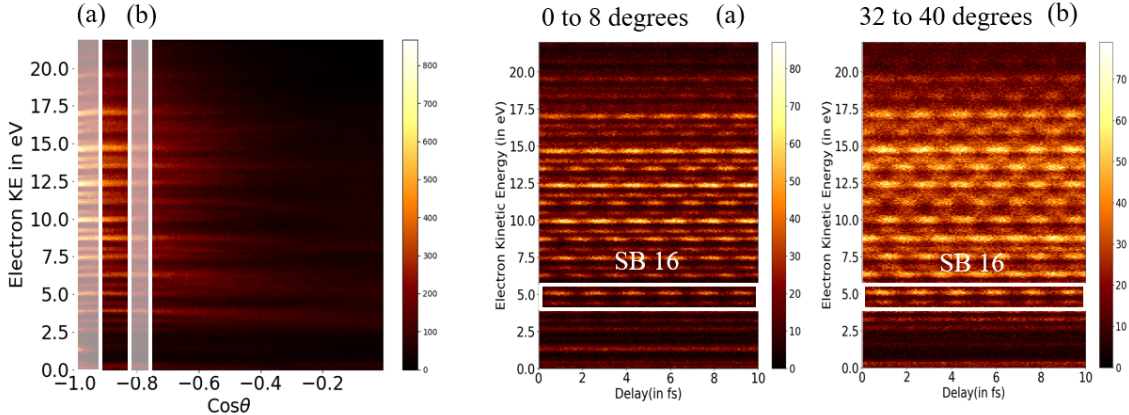


Figure 5.15: Left : Angular distribution of electrons from a RABBIT measurement on Krypton, integrated over all delays, Right : Top : RABBIT traces for electrons emitted at 0 to 10 and 30 to 40 degrees respectively, Bottom : Sideband phases as a function of emission angle for SB 16.

For ionization by linearly polarized XUV, the selection rules are $\Delta l = \pm 1$ and $\Delta m = 0, \pm 1$. Therefore, the ionization delay is a weighted average of the various pathways. The general expression for the delays of $np_{3/2}$ and $np_{1/2}$ is given by:

$$\tau_j \simeq \frac{\tau_{np_{m=0}} |T_{np_{m=0}}|^2 + 2\tau_{np_{m=1}} |T_{np_{m=1}}|^2}{|T_{np_{m=0}}|^2 + 2|T_{np_{m=1}}|^2} \quad (5.6)$$

where $j=1/2$ and $3/2$, $T_{np_{m=0}}$, $T_{np_{m=1}}$ are the elements of the dipole transition matrix elements (see 1.1.1), given by:

$$\begin{aligned} T_{np_{m=0} \rightarrow \epsilon s} &= \frac{1}{\sqrt{3}} Y_{00} R_{np \rightarrow \epsilon s}, \\ T_{np_{m=1} \rightarrow \epsilon d} &= 2\sqrt{\frac{1}{15}} Y_{20} R_{np \rightarrow \epsilon d}, \\ T_{np_{m=1} \rightarrow Ed} &= -\sqrt{\frac{1}{5}} Y_{21} R_{np \rightarrow Ed} \end{aligned}$$

where Y_{lm} and $R_{np \rightarrow \epsilon s, \epsilon d}$ are the spherical harmonics and the radial integrals, respectively. For emission close to the polarization axis of the laser, only the $4p_{m=0} \rightarrow \epsilon d$ transition dominates, while at higher angles ($\theta > 45^\circ$), the $4p_{m=1} \rightarrow \epsilon d$ and $4p_{m=0} \rightarrow \epsilon s$ transitions contribute significantly as well.

The spherical harmonic for the d-wave has a node at the 'magic angle' of 54.7° , resulting in a strong decrease in the contribution of ϵd channel. Combined with the variation of the relative strengths of the ϵs and ϵd channels throughout the resonance, a significant variation of the photoionization delays is expected as a function of the emission angle. As discussed above, at resonance, the ϵs channel dominates the ionization $P_{1/2}$, while its contribution to the transition $P_{3/2}$ is

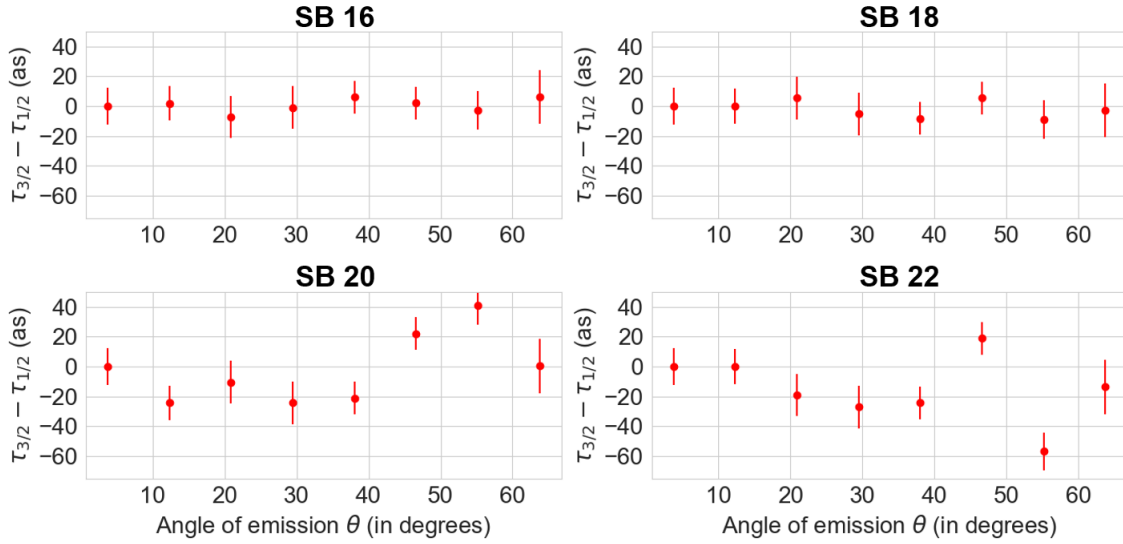


Figure 5.16: Difference in photoionization delays between the $P_{3/2}$ and $P_{1/2}$ levels as a function of angle of emission, for the various sidebands.

greatly reduced. Therefore, τ_{Wigner} for $P_{3/2}$ varies strongly from 45 degrees onward. This results in a variation of the delay difference as a function of angle for sidebands 20 and 22, which are formed by the emission/absorption of an IR photon, respectively.

The continuum-continuum delay (τ_{cc}) does not play a significant role here, as the long-range interaction resulting in τ_{cc} is very weak compared to the short-range interaction resulting in τ_{Wigner} . The τ_{cc} is close to zero for kinetic energies greater than a few electron volts[52, 126].

Overall, the analysis of photoionization delays for the two spin orbit components in Krypton clearly shows that, in the vicinity of $4s4p^6np$ autoionizing resonances, significant variation can be observed. Away from the resonances, the spin-orbit delays do not vary significantly. Near the resonances, the delay differences exhibit dependence on the angle of emission. The presence of strong angle-dependent variation close to the 'magic angle', indicates a complex ionization pathway that combines the ϵs and ϵd channels.

The results presented here complement another measurement on argon presented in [66], where similar angle-dependent delays have been attributed to the presence of resonances $3s^{-1}np$ in the vicinity of a harmonic. The work presented here clearly indicates the potential to theoretically and experimentally investigate further the role of spin-orbit interactions on the outgoing electron wavepacket's phase. As a next step, RABBIT measurements with circularly polarized IR probe pulses or even cross-polarizing the IR pulse with respect to XUV can help to understand the contributions of the $\Delta m = \pm 1$ channels[127].

6 RABBIT measurements on Argon dimers

In this chapter, a RABBIT measurement performed on argon dimers will be presented. Although there have been several synchrotron measurements on noble gas dimers in the past (e.g., [128, 129]), so far there have only been a few time-resolved measurements (see, e.g., [130, 131]). To gain an insight into the photoionization delays experienced by electrons due to Van der Waals[132] forces, a RABBIT measurement was performed on argon dimers. The data presented here is from the same measurement presented in section 4.3. With the help of coincidence measurements, the photoionization delays for dimers is compared to atomic photoionization. Some of the results presented here are also part of the following publication: **High-repetition rate attosecond beamline for multi-particle coincidence experiments**, *Optics Express Vol. 30, Issue 8, pp. 13630-13646 (2022)*

6.1 Formation of dimers

In a freely expanding gas jet, a small number of atoms and molecules aggregate through a very weak attraction to form clusters. The smallest cluster possible is a dimer, which has two atoms or molecules bound together by Van der Waals forces, which are extremely weak forces. To understand the formation of dimers, we need to consider the thermodynamics of an expanding gas jet¹. The supersonic expansion of a gas through a nozzle in the REMI can be considered *isoentropic* (constant entropy). This situation is represented by the Isoentrope curve in the figure below. Starting from stagnation conditions in a gas bottle, the gas expands isentropically from point A to point B in the figure. If thermal equilibrium is maintained beyond point B, then the expansion continues along the *vapor pressure* curve $P_v(T)$. However, if the expansion occurs very quickly and thermal equilibrium cannot be maintained (as it does in the REMI), the expansion proceeds through the Dry Isentrope ($P(T)$) curve BC in the figure. The state of the gas at this point is unstable and it is superaturated due to delayed condensation during the rapid expansion. Depending on the temperature and pressure at B, it expands further to C, where the supersaturated state collapses and results in dimers or clusters.

Usually, diatomic molecules are formed by sharing electrons between two atoms through a covalent bond. In the case of noble gases, this is not possible because of the completely filled electronic shells. However, at large internuclear distances ($>5 \text{ \AA}$), the atomic electron polarizabilities interact. Although this interaction is weak, the momentary polarization of noble gas atoms can result in an attractive

¹An in-depth description is available in Ref. [133]

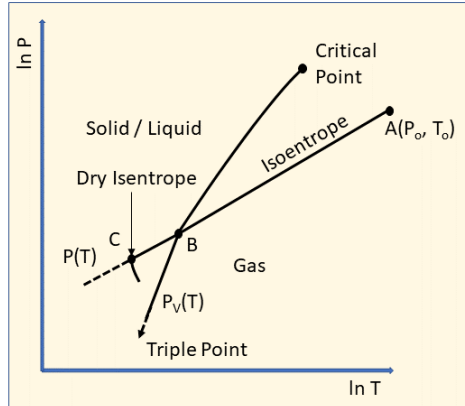


Figure 6.1: $\ln P - \ln T$ diagram for a gas which condenses upon expansion. Figure adapted from [133].

London dispersion force [134] that leads to the formation of a noble gas dimer. The interaction leading to the formation of dimers scales with R^{-6} , where R is the internuclear distance.

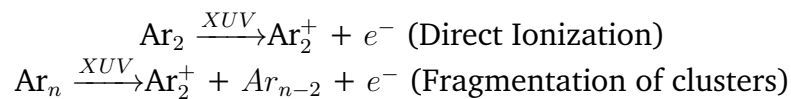
These interactions are called Van der Waals interactions and are well approximated by the Lennard-Jones potential [135], given by:

$$V(R) = \frac{D_e}{(\frac{R}{R_0})^{12}} - \frac{2D_e}{(\frac{R}{R_0})^6} \quad (6.1)$$

The quantities R_0 and D_e refer to the equilibrium distance(Van der Waals contact distance) and the depth of the potential well, respectively. The Van der Waals interactions are usually 100 to 1000 times weaker than the Coulomb interactions, and their magnitude is almost the same as the thermal energies at room temperature (i.e. $k_B T \approx 0.025$ eV). Therefore, to study noble gas dimers, very low temperatures (< 10 Kelvin) are required. This is achieved by supersonic expansion of noble gases inside the REMI.

6.2 Direct Ionization of dimers

When argon is used as a target gas in the REMI, a small but noticeable number of dimer ions (Ar_2^+) are detected. Dimer ions (Ar_2^+) are visible in the time-of-flight (ToF) spectrum for the ions, at $\sqrt{2}$ times the ToF for monomer (Ar^+) ions. The dimer ions are formed as a result of two different processes :



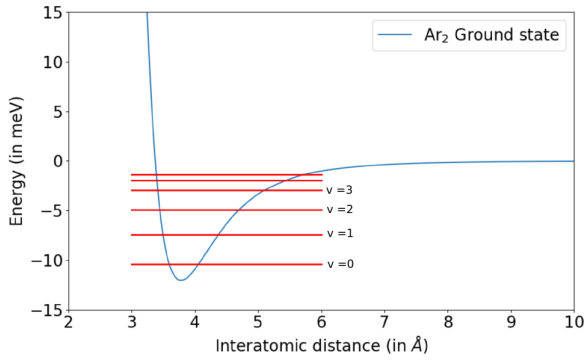


Figure 6.2: Potential energy curve for the Ar_2 ground state along with the first few vibrational levels. The data for the potential energy curve and the vibrational levels is taken from references [136, 137, 138]

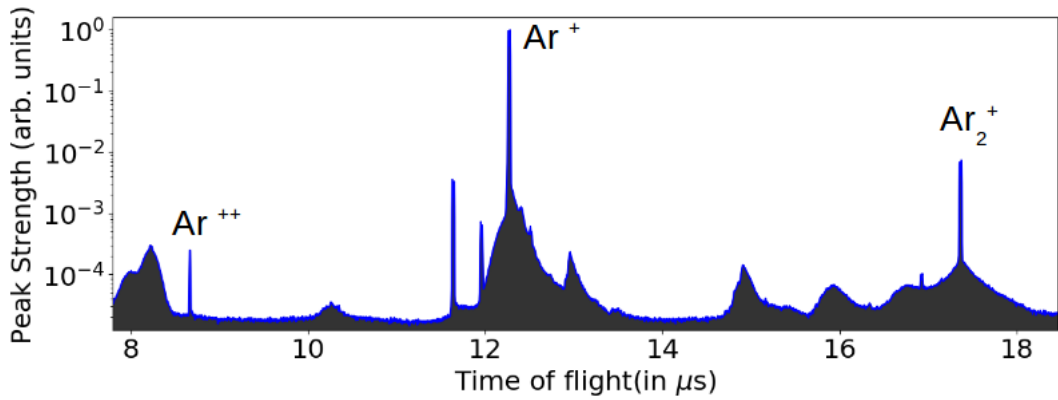


Figure 6.3: Time-of-flight spectrum for ions, from the ionization of an argon gas target by XUV and IR

Due to cluster formation and subsequent fragmentation, the dimer yield therefore increases with backing pressure of the supersonic jet. For this measurement, the backing pressure was approximately 3 bars. The number of dimer ions detected in this measurement is about of 1% of monomer ions (Fig. 6.3).

Although the number of detected dimer ions is low compared to atomic argon, the number of ion-electron coincidences is sufficient to resolve peaks in the photoelectron spectrum and also to observe sideband oscillations. Because both ions were created under identical experimental conditions, the photoelectron spectra and sideband oscillation phases for both cases can be compared directly.

6.2.1 Comparing photoelectron spectra

In order to compare the photoelectron spectra, the kinetic energy spectra of electrons detected in coincidence with the ions Ar^+ and Ar_2^+ are integrated over all

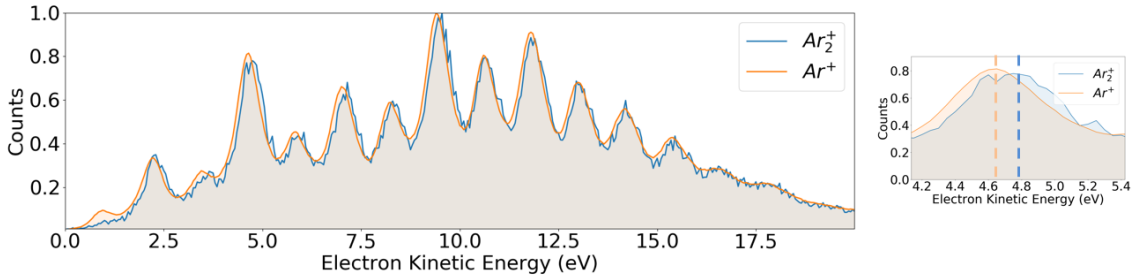


Figure 6.4: Left: Photoelectron spectrum integrated over all delays for electrons detected in coincidence with monomers and dimers respectively. Right: An inset showing an almost 0.2 eV spacing between the kinetic energies of electrons.

XUV-IR delays. They are normalized to their respective maxima and the resulting distributions are overlaid for comparison (Fig. 6.4). The spectra are almost identical, except for small differences in electron kinetic energies (≈ 0.2 eV). The electrons from the dimer have a slightly higher electron kinetic energy in comparison to those from the monomer. The reason is the slightly lower ionization threshold of the Argon dimers, which has been measured in synchrotron measurements earlier[139, 140].

The photoelectron peaks also do not exhibit any vibrational broadening. This is because the potential well of the neutral dimer is very shallow and the vibrational states have a bandwidth of ≈ 10 meV[140](Fig. 6.2). Due to the resolution of the setup, the vibrational levels cannot be resolved. Hence, the photoelectron spectrum for both cases is almost identical except for the one difference explained above.

6.2.2 Comparing photoionization delays

The argon atom has an electronic configuration of $1s^2 2s^2 2p^6 3s^2 3p^6$, while the argon dimer has a linear combination of atomic orbitals, resulting in molecular orbitals. Closest to the ionization threshold is the highest-occupied molecular orbital (HOMO) and for argon dimers, they are $3p\sigma_u$, $3p\pi_g$, $3p\sigma_g$ & $3p\pi_u$.

When a neutral dimer absorbs an XUV photon, it results in the release of an electron in the continuum and a transition from the neutral ground state to one of the ionic ground states (A to D in Fig. 6.5). $A^2\Sigma_u^+$, $B^2\Pi_g$ are bound ionic states, while $C^2\Pi_u$ and $D^2\Sigma_g^+$ are antibonding/dissociating states that result in dissociation of the dimer ion ($Ar_2^+ \rightarrow Ar^+ + Ar$) to an ion and a neutral atom. To detect the dimer ions, they need to be in a bound state, and hence the XUV ionization of a neutral dimer must result in a transition to the A and B states. Therefore, the ionization of the dimer proceeds from the $3p\sigma_u$ & $3p\pi_g$ orbitals in the ground state and ends in a superposition of the $A^2\Sigma_u^+$ (*ungerade*) and $B^2\Pi_g$ (*gerade*) ionic states, both of which have opposite parities. Mixed parities of the

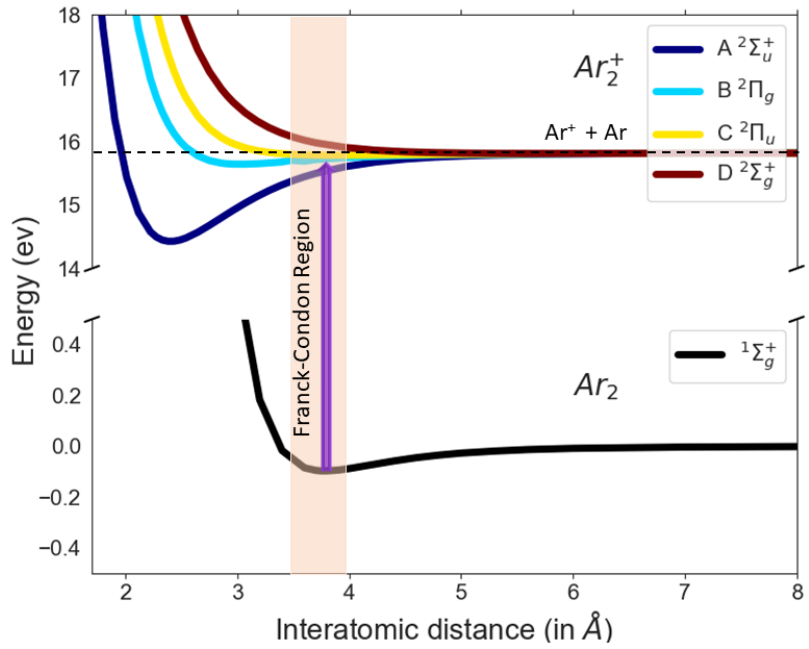


Figure 6.5: Calculated potential energy curves(PECs) of the neutral argon dimer and the argon dimer ion. The data for the PECs is taken from Ref.[141, 142]

ion wavefunction result in a superposition that oscillates over time, due to the energy difference between the two levels[138]. However, the oscillation period is so long that the ejected electron practically sees a frozen molecular ion core.

In atomic argon, the electron wavepacket released in the continuum will experience a *Wigner* phase shift due to its interaction with the Coulomb potential, as described in Sec. 2.2. Likewise, in the dimer, the electron experiences a phase shift due to the double-well potential. At the instant of ionization, the electron is localized on one of the atoms in the dimer and when the electron is released into the continuum, it experiences an additional phase shift as a result of the long-range potential of the "other" atom in the dimer. The interatomic distance remains large enough after ionization that the electron released after localization on one side of the dimer is diffracted by the atom on the other side[136, 143].

To quantify the phase shifts in the atomic and dimer cases, the RABBIT traces (Fig. 6.7) of electrons detected in coincidence with monomers and dimers respectively, can be analyzed with the procedure described in Sect. 2.3. Analogous to the atomic case, the sideband oscillations can be fitted with a cosine function given by:

$$I_{SB}(t) = A \cos(2\omega_{IR}\tau + \Delta\phi_{XUV} + \Delta\phi_{dimer}) + B \quad (6.2)$$

where $\Delta\phi_{XUV}$ is the XUV spectral phase and $\Delta\phi_{dimer}$ is the phase shift arising from the interaction of the electron with the Van der Waals potential and the probe IR

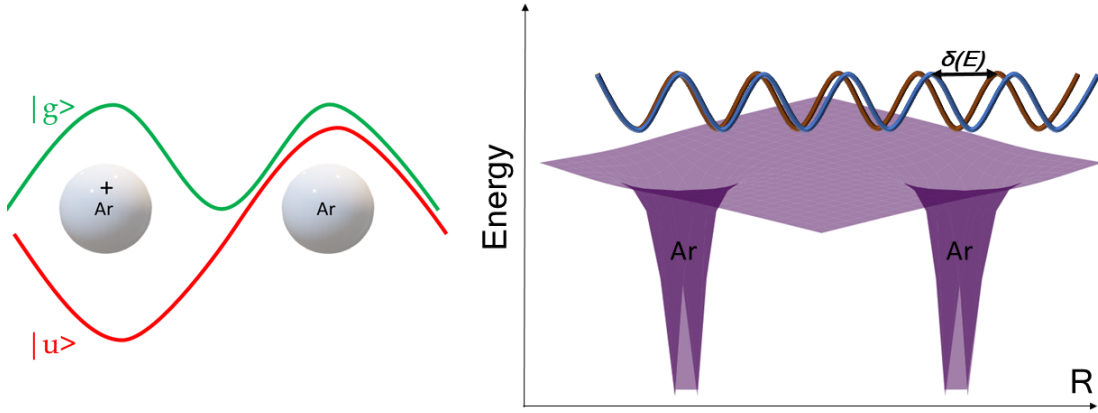


Figure 6.6: Left : Visualization of the superposition of *gerade* and *ungerade* states of the Ar_2^+ ion and the charge localized on one side, Right : The brown colored wave is a freely propagating wavepacket with kinetic energy E and the blue colored wave is the phase shifted wavepacket of the same kinetic energy, experiencing scattering by the dimer potential

field in the continuum. By taking the phase difference of each sideband from the two RABBIT traces, we can directly compare the atomic and dimer phases. The XUV spectral phase cancels out, since the experiment was performed under identical conditions. Dividing the phase difference by $2\omega_{IR}$ provides the time delay difference, given by :

$$\Delta\tau(\text{Ar}_2 - \text{Ar}) = \frac{\phi_{\text{Ar}_2} - \phi_{\text{Ar}}}{2\omega_{IR}} \quad (6.3)$$

The sideband oscillation phases and the corresponding delay differences are plotted in Fig. 6.8. The error bars for the individual phases are obtained from the covariance matrix of the cosine fit (explained in 2.3), while the error bars for the phase difference are obtained using the expression $\sigma_{\phi(\text{Ar}_2 - \text{Ar})} = \sqrt{\sigma_{\phi_{\text{Ar}_2}}^2 + \sigma_{\phi_{\text{Ar}}}^2}$, where σ represents the respective standard deviations.

The phases show the same trend in both cases and indicate that the difference between the two is independent of the XUV chirp. The error associated with the phase retrieval is larger in the dimer case due to the smaller number of data points. Since the standard deviation depends on the square root of the number of data points ($\sigma \propto \frac{1}{\sqrt{N}}$), the errors for dimers are 10 times higher than monomers.

The delay differences exhibit a weak trend that resembles a damped oscillation. The oscillating trend is limited to sidebands 16 and 18, while the difference is almost zero as the electron kinetic energy increases. The reason for this is the additional phase shift a dimer electron experiences from the second atom in the dimer, as explained earlier. This effect is visible particularly close to the ionization threshold. As the kinetic energy increases, the outgoing electron in a dimer

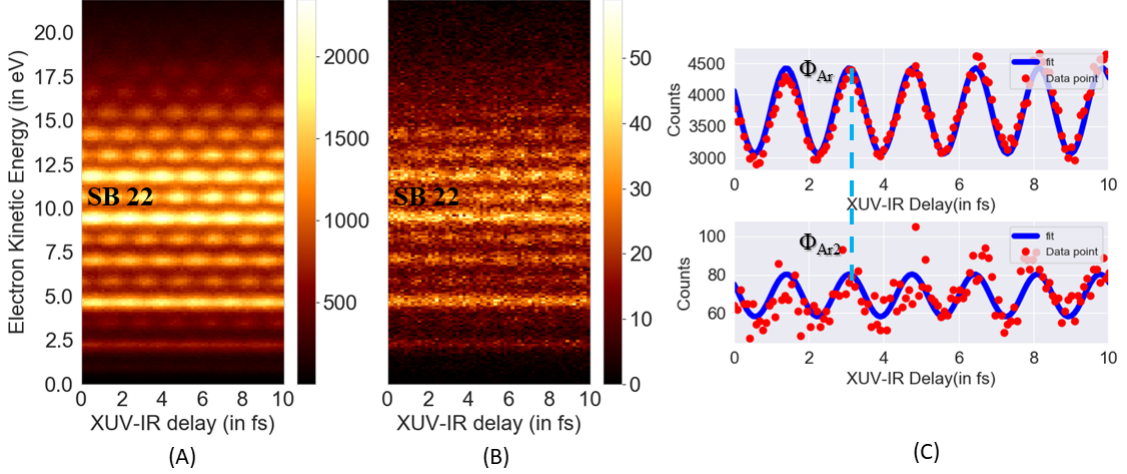


Figure 6.7: (A): RABBIT trace for electrons detected in coincidence with the monomer ions (Ar^+), (B): RABBIT trace for electrons detected along with the dimer ions (Ar_2^+), (C): Top - Projection of Sideband 22 from (A) , Bottom - Projection of Sideband 22 from (B)

experiences a phase shift that is mostly from the potential of only one atom and hence there is no difference in the photoionization delays between monomers and dimers.

A RABBIT measurement on Krypton monomers and dimers presented in reference [143], reveals a similar trend as well. This is interpreted as a consequence of a two-center interference effect involving ${}^2\Sigma_u$ and ${}^2\Pi_g$ ionic states. The krypton dimer ion is in a superposition of ${}^2\Sigma_u$ and ${}^2\Pi_g$ after photoionization and these states launch electron wavepackets with a phase difference of π units with respect to each other. If the ionization probabilities for the *gerade* and *ungerade* parities are equal, the interference effect would not be visible. However, since the ionization probabilities are unequal for the two parities, the outgoing wavepackets are not exactly π radians out of phase and hence a residual interference effect is observed.

Although parallels can be drawn between the results presented in ref. [143] and the results presented here, there is one important point that needs to be taken into consideration. Just as in Krypton, a two-center interference effect could be expected for sidebands 14 and 16 in argon, which are closest to the ionization threshold. The signal for sideband 14 however is very weak because the aluminium filter used to remove any residual IR after HHG suppresses even the XUV photons having energies below 15 eV. Without a sufficiently strong signal for sideband 14 in the measurement presented here, it is not possible to retrieve sideband oscillation phases and ascertain the presence of two-center interference effects.

Nonetheless, a comparison of the angular distributions for the low kinetic energy electrons reveals an interesting feature. In fig. 6.10, the SB 14 is clearly

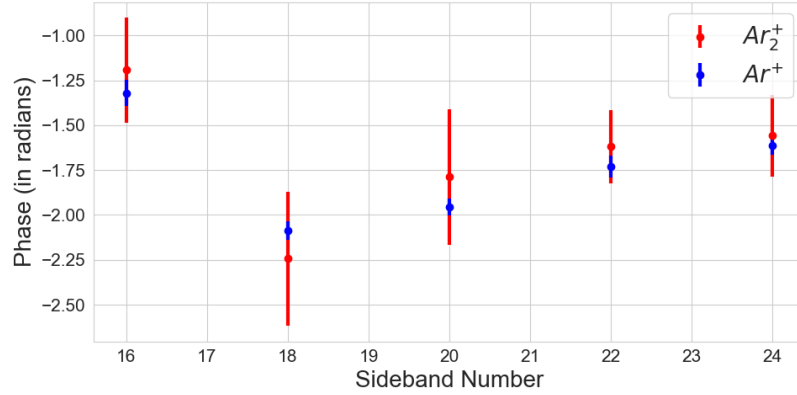


Figure 6.8: Sideband oscillation phases for the electrons detected in coincidence with Argon dimer and monomer ions respectively, Right : Time delay differences for the each sideband

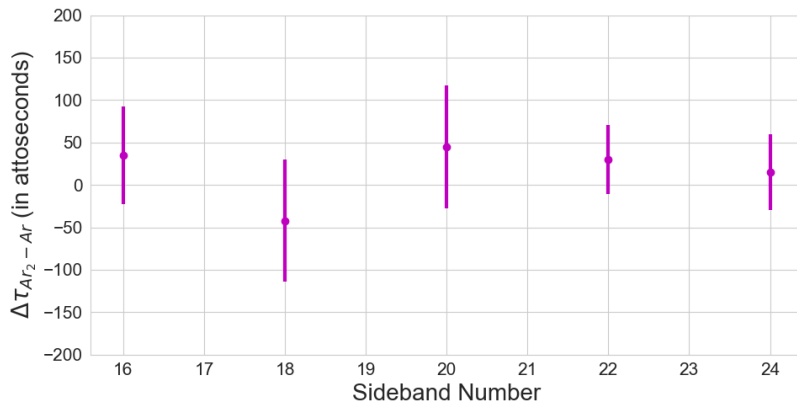


Figure 6.9: Time delay differences for each sideband

stronger in the Ar^+ case. The reason for this is the under-threshold excitation of Argon by harmonic 13 and subsequent ionization by the IR as shown in Fig. 6.11. While a similar under threshold excitation is possible in the dimer as well, the absorption of IR after excitation by XUV leads to the dissociation (Fig. 6.13) of the dimer. Hence there is no signal for sideband 14 with the bound dimer ions. This goes on to show that it may not be possible after all to measure the two-center effects in argon dimers, very close to the ionization threshold. In addition, while comparing the phases for the sidebands closest to the threshold, the effects of under-threshold excitations in atoms would dominate and significantly affect the results of a measurement.

Therefore, with the information available from the RABBIT measurement presented here, it can be concluded that the photoionization delays associated with argon dimers is not significantly different from that of atomic argon. Unlike krypton, the two center interference effects (if any) would be very weak. An alternate

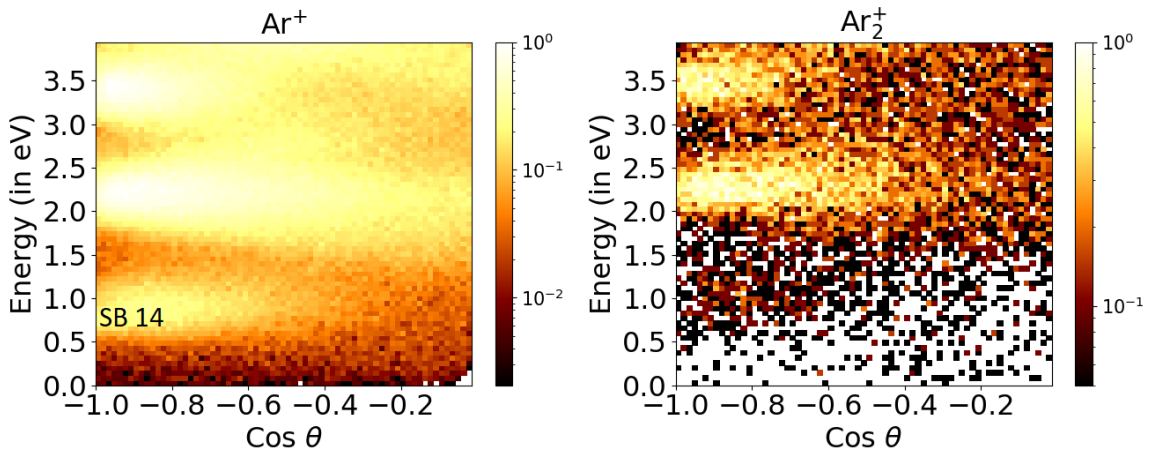


Figure 6.10: Angular distribution of the low energy electrons detected in coincidence with the monomer and dimer ions respectively.

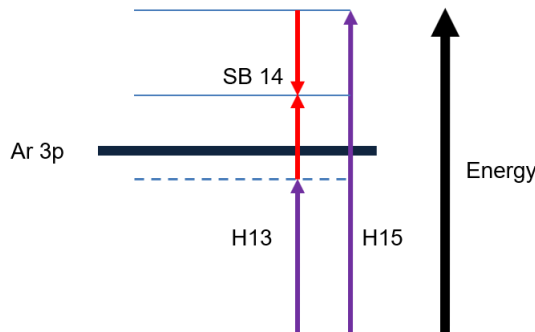


Figure 6.11: Formation of SB 14, through under-threshold excitation of Argon by Harmonic 13 and subsequent ionization by IR

way to observe two center interferences in argon dimers would be to look at the dissociation channel.

6.3 Dissociation of Dimers

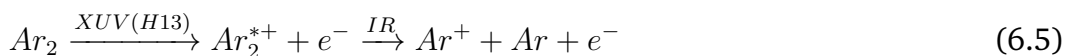
In addition to the removal of an electron through direct ionization, the XUV radiation incident on argon dimers can also result in an additional fragmentation process called dissociation. The dissociation of dimers could lead to two sets of end products, namely, an ion and a neutral ($Ar^{+*} + Ar^0$) or two ions ($Ar^{n+} + Ar^{n+}$). During dissociation, the excess energy after the removal of an electron is shared between the ions and neutrals through the Kinetic Energy Release (KER) [144]. For dissociation into an ion and a neutral, the KER is calculated by multiplying the Ar^+ ion kinetic energy by two. The XUV photon energies used in the measurement presented above, predominantly involve pathways which result fragmentation into an ion and a neutral (Fig. 6.17). The lowest dissociation threshold for Argon dimers

is at ≈ 15.7 eV, and therefore a significant number of Ar^+ ions detected come from the dissociation of the dimer ion.

There are two ways through which the dimer can dissociate. The first is the *direct* dissociation (Fig. 6.12), which happens by absorbing an XUV photon of sufficient energy.



In this pathway, the electron carries most of the energy and the KER is only about 0.2 to 0.4 eV. The second is an *indirect* dissociation (Fig. 6.13):



In this pathway, the XUV ionizes the dimer and leaves it in the bound state ($A^2\Sigma_u^+$). In the presence of an additional IR photon, the nuclear wavepacket undergoes a transition to the dissociating $D^2\Sigma_g^+$ curve. This would result in a KER slightly less than 1.2 eV. By choosing electrons detected in coincidence with ions having two different KER values, the RABBIT spectra for electrons from the two channels can be obtained. The phases can then be extracted from the respective RABBIT traces and compared, to look for any effects that can be attributed to interference effects. The two distinct reaction pathways contributing to the same final state of the electron leads to an interference.

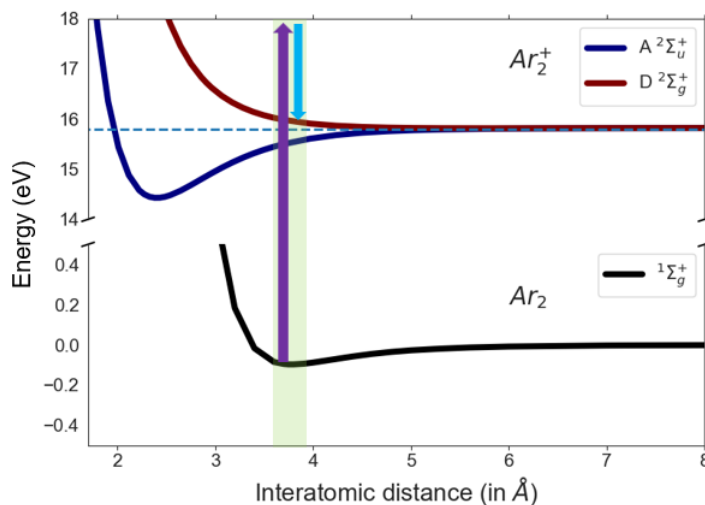


Figure 6.12: Schematic of the "direct" dissociation pathway

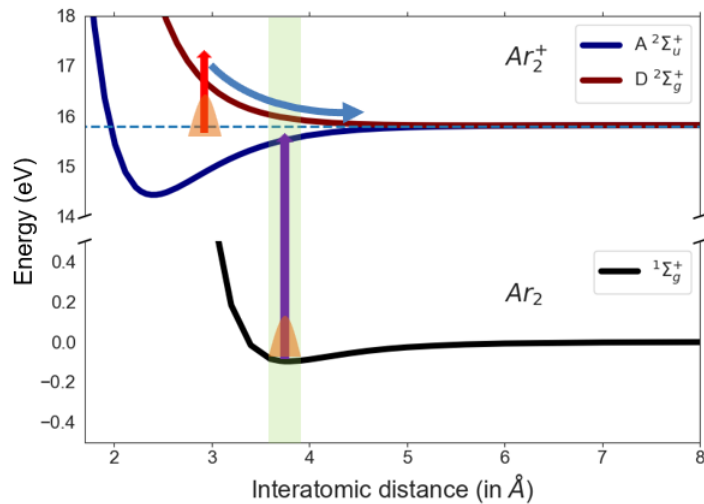


Figure 6.13: Schematic of the "indirect" dissociation pathway

In this experiment, the retrieval of sideband oscillation phases from the two channels is complicated for two reasons. First, the number of coincidences that can be detected from the two dissociation channels is inherently low. The KER distribution for Ar^+ is dominated by events from ionization of atomic argon. The number of dimer dissociation events is usually 10^{-3} to 10^{-4} times lesser than the number of events detected from atomic photoionization.

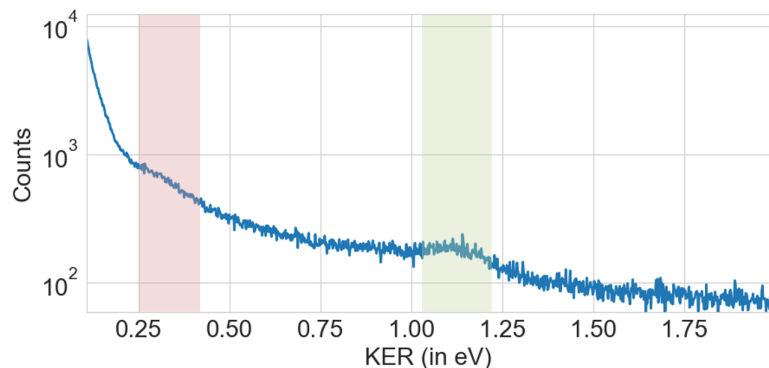


Figure 6.14: KER Distribution of Argon ions. The region shaded red corresponds to ions from the "direct dissociation" while the region shaded green corresponds to "indirect" dissociation

Second, the formation of argon clusters and their subsequent fragmentation introduces a significant background to the overall signal. This can be seen clearly in figures 6.3 and 6.15. The dissociation of dimers appears as a broad distribution around the Ar^+ peak in the ion ToF spectrum. Likewise, the presence of a broad distribution around Ar_2^+ ions indicates that there are a significant number

of clusters formed along with the dimers in the gas target, which breaks down into dimers and possibly even monomers.

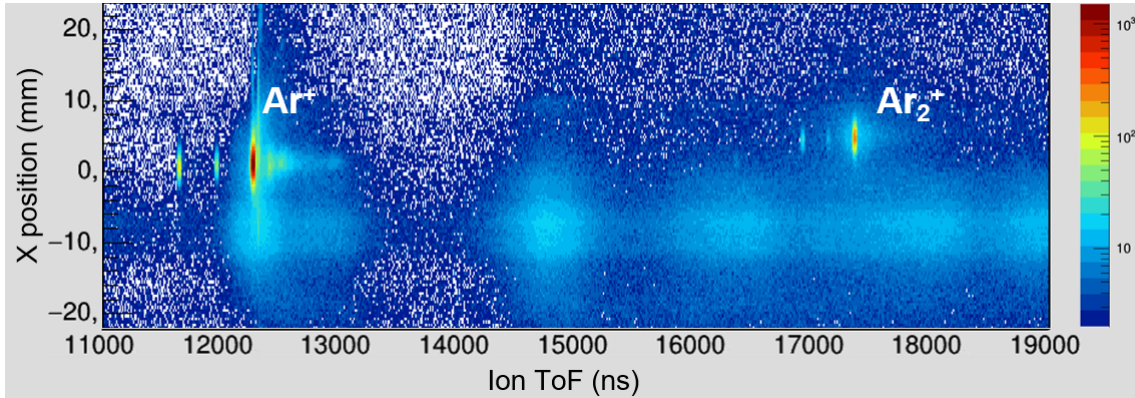


Figure 6.15: A plot of the time of flight of the ions versus the X coordinate of the hits on the ion detector

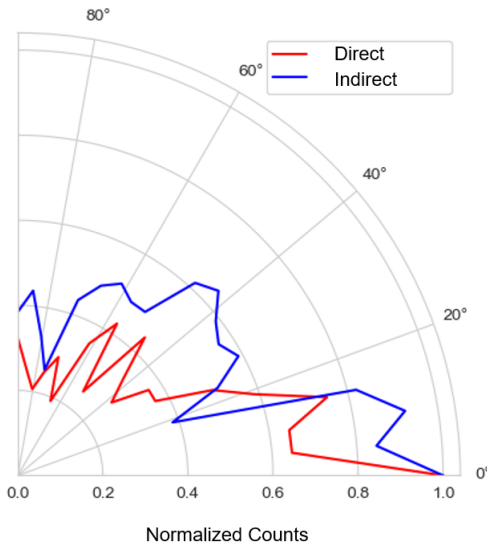


Figure 6.16: Angular distribution of the electrons corresponding to the direct and indirect dissociation channels

Due to these reasons, an analysis of the RABBIT traces is not presented here, since the variations in sideband oscillation phases cannot be unambiguously interpreted. Another clear indicator of two-center interferences is the molecular frame photoelectron distributions which could also not be generated for the same reason. The angular distribution of photoelectrons in the lab frame however indicates a small difference between the two channels (Fig. 6.16). Even with the limited statistics, it can be noticed that the electrons from the two channels exhibit slightly different distributions, arising quite possibly from the opposing parities of the wavefunctions in the direct and indirect pathways.

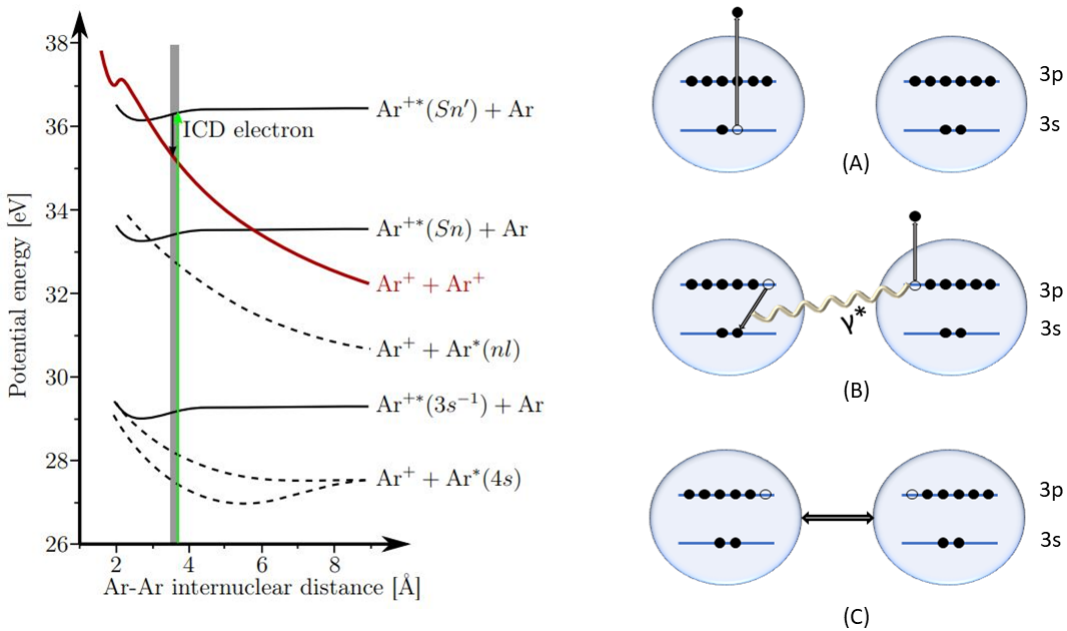


Figure 6.17: Left: Potential energy curves showing the decay of various excited states of Ar_2^+ ions. Of particular interest here is the transition that results in ICD (red curve). PECs taken from [145]. Right : ICD in Ar_2 . (A) 3s ionization by XUV, (B) $3p \rightarrow 3s$ decay and 3p ionization through a virtual photon, (C) Dissociation via Coulomb explosion.

As the XUV photon energy increases close to the 40 eV photon energy, the argon dimer dissociates through a process called *Interatomic Coulomb Decay*(ICD)[146]. ICD is an indirect electron decay mechanism, observed particularly in weakly bound systems such as dimers and clusters, and results in a doubly ionized dimer that then fragments into two ions (Fig. 6.17). The mechanism can be understood as follows: first, an inner-valence electron is removed from one atom through photoionization. Following this, the outer-valence electron takes the place of the inner-valence electron through an Auger transition[147]. The excess energy from this transition excites and ionizes a valence electron from the neighboring atom. Repulsion of positive charges in neighboring atoms results in a Coulomb explosion[148] and releases two positively charged ions.

To identify the Ar^+ ions formed by ICD, we use a map of Photoion-Photoion coincidences, known as the PiPiCo[149]. This is done by taking the time-of-flight of the ion that arrives first at the detector (ToF1) versus that of the ion impinging second (ToF2), as shown in Fig. 6.18. Along the z-axis (spectrometer axis) the momentum component is approximately proportional to the ToF. Hence, the sum $\text{ToF1} + \text{ToF2}$ must be constant for all charged particles from the same molecule. In a spectrum where ToF1 is plotted versus ToF2 , the events which come from the dissociation of a molecule appear as a diagonal line.

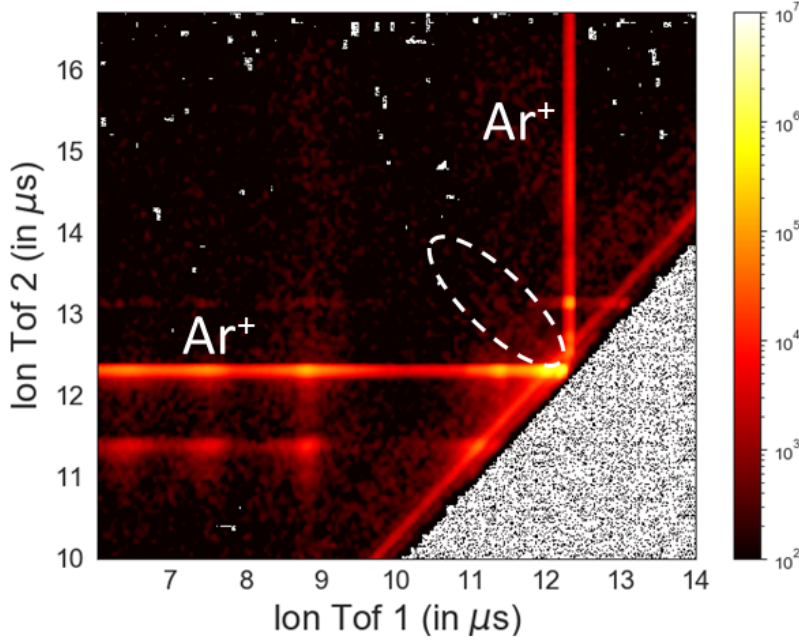


Figure 6.18: Photoion-Photoion Coincidence Spectrum (PiPiCo) ToF1 of the first particle reaching the detector plotted versus the ToF2 of the second particle for photoionization of Ar_2

In the measurement presented here, apart from the ionization of dimers, a small number of ions from the ICD pathway were detected as well. These events are faintly visible in the PiPiCo spectrum in (dashed ellipse in Fig. 6.18). The ICD pathways open up at the cutoff edge of the Harmonic spectrum (≥ 35 eV). Since the XUV harmonics spectrum reaches a maximum of 40 eV, only the first ICD channel resulting in two Ar^+ ions can be reached. The ICD signal can be enhanced by using XUV radiation with higher photon energies. In addition, ICD pathways resulting in higher charges on Argon ions (Ar_2^+ , Ar_3^+ etc) open up at higher energies as well.

The results of a RABBIT measurement on monomer and dimer argon presented here gives a brief overview of the influence of Van Der Waals forces on photoionization delays. Unlike diatomic molecules, photoelectrons from noble gas dimers exhibit a very weak variation in photoionization delays, compared to their monomer counterparts. The results presented also show it is possible to observe two-center interferences in dimer dissociation through XUV- IR pump-probe experiments, although there are several challenges to overcome. These interferences in dissociation have been already observed in IR multiphoton ionization measurements (e.g. reference [150]) but does not provide any information on the time-dependent dynamics.

For two-center interference measurements close to the ionization threshold, the wavelength of the driving laser requires tunability to adjust the frequency of XUV

harmonics away from resonances and minimize the influence of under-threshold ionization on the sideband oscillation phases. Alternatively, the measurements could be performed without an aluminium filter, so as to have sufficient signal from sidebands very close to the threshold.

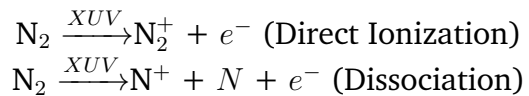
For the next set of measurements to study the dissociation of dimers, it is clear that the experimental apparatus would require additional tweaking. The experiment could be repeated for a longer duration with a lower backing pressure for the REMI target, to prevent the formation of clusters. In addition, the XUV harmonics cutoff needs to be increased to get more events from the ICD process. The ICD process so far has not been studied with attosecond precision and would be a promising field to explore.

7 XUV-IR measurements on Nitrogen

In this chapter, two sets of measurements that were performed to particularly study the dissociation of molecular nitrogen are presented. The first measurement involved ionization and dissociation of a nitrogen gas target in the REMI, with only the XUV harmonics. The data was acquired over 12 hours. Following this, a XUV-IR pump-probe measurement was performed as well, with the goal of observing dissociation dynamics on the sub-femtosecond timescale. The acquisition time for this measurement was about 24 hours. Till date, the XUV-IR pump-probe measurements on molecular nitrogen that have been reported in literature (eg. refs.[151, 152, 153]) either focus only on the dynamics of molecular ions or the dynamics of electrons. This experiment is aimed at observing the two processes simultaneously.

7.1 Ionization of Nitrogen by XUV

The XUV spectrum used in this experiment ranges between 15 and 40 eV. In this photon energy range, the nitrogen molecule can undergo two reaction pathways :



In the first case of direct ionization, one electron is removed from the molecule and a molecular ion is left behind. If the photon energy is high enough, the molecule could directly dissociate into an ion and a neutral. In the case of direct ionization, the photoelectrons carry almost all the energy, while the kinetic energy of ions is extremely low (<0.1 eV). In the case of dissociation however, a significant amount of energy is shared between the ion and neutral through kinetic energy release (KER)[144], reach upto a few electron Volts.

The ions coming from the two channels can be easily identified in the ToF spectrum. The N_2^+ ions coming from the direct ionization appear as a narrow peak in the spectrum, while the N^+ ions coming from the dissociation process appear as a broad distribution in the spectrum. The reason for this is the large spread in kinetic energies of the ions during dissociation. In fact, the vibrational levels from the potential energy curves that are involved in dissociation are visible in a plot of the X coordinate of the ion detector versus the ion ToF (Fig. 7.2).

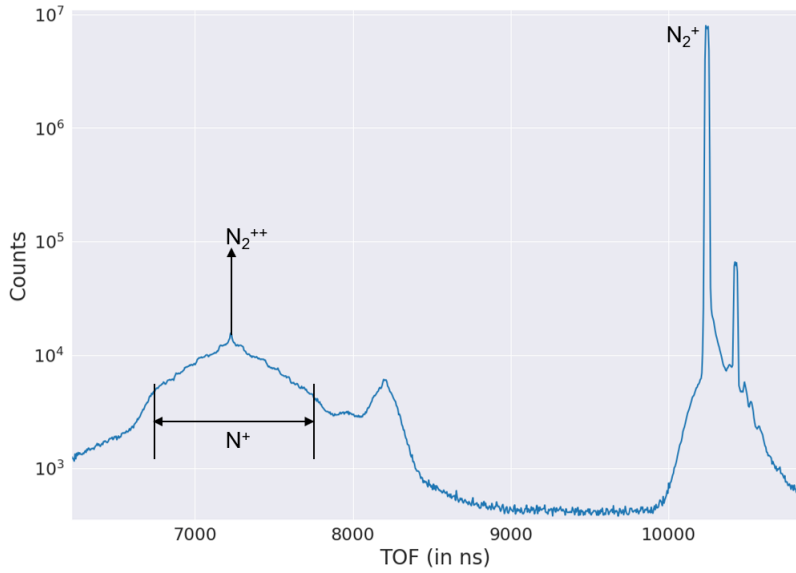


Figure 7.1: Time of flight of ions detected after ionizing N_2 as a target in the REMI

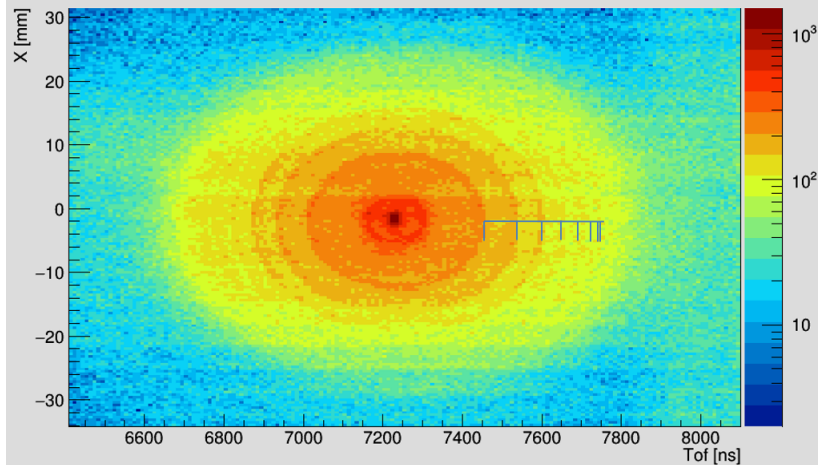


Figure 7.2: A 2D histogram mapping the ion time of flights with the X co-ordinate of the ion positions on the detector. The rings are formed by dissociation from various vibrational levels in the PEC.

Along with direct ionization and dissociation, there is a small number of doubly ionized N_2^{++} ions. The threshold for double ionization is about 42 eV and is ionized by the XUV in the cutoff region of the harmonics. Since the charge to mass ratio of the N_2^{++} ions is the same as N^+ ions, they appear in the middle of the N^+ ion distribution. As can be seen in Fig. 7.3, the nitrogen molecule is a complex system with several potential energy curves playing a role in photoionization and dissociation. Only with coincidence measurements can the ions and electrons coming from various ionization channels be identified. By choosing electrons detected in coincidence with the various ions, the photoelectron spectra for

each ionization channel can be obtained.

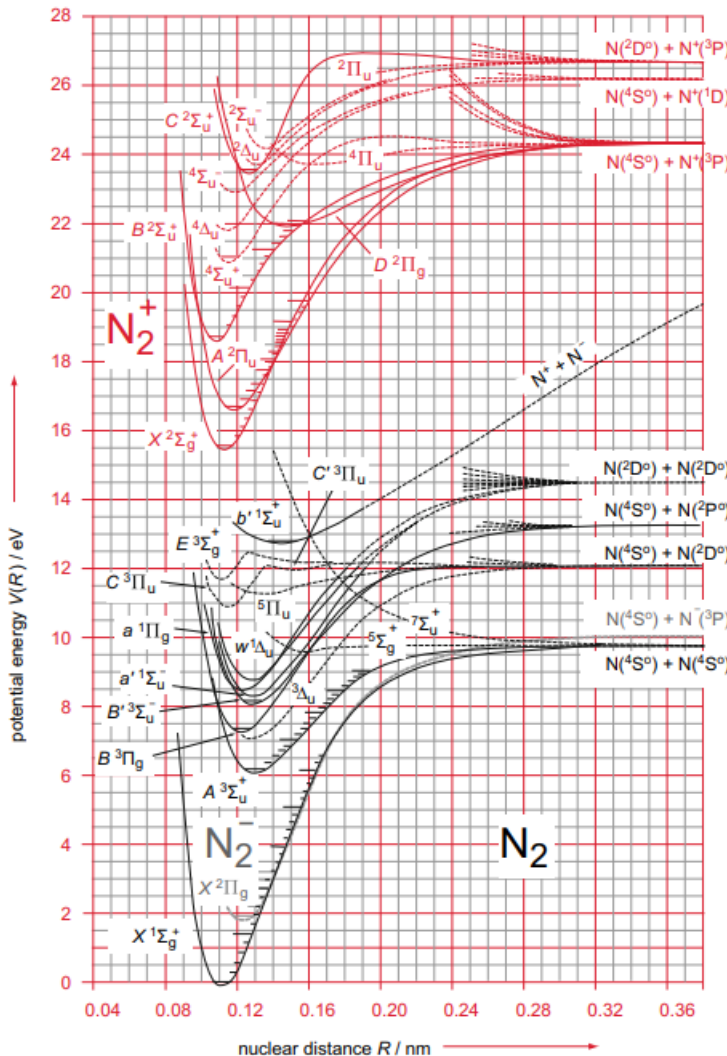


Figure 7.3: Potential energy curves for neutral N_2 and the ionic ground state N_2^+ .
 Figure taken from [36]

7.1.1 Direct ionization

We first look at the electrons detected in coincidence with N_2^+ ions, or the direct ionization channel. To get the best resolution, only the electrons emitted between 0 to 45° with respect to the spectrometer axis are chosen¹. In the direct ionization of nitrogen, there are three PECs that need to be considered[36, 154] (Fig. 7.4). Each harmonic in the XUV frequency comb that ionizes molecular nitrogen will

¹The procedure to choose electrons emitted over specific angles with respect to the polarization/spectrometer axis is explained in Sec. 5.4.1

hence result in a series of three peaks, as explained in Section 1.2.3 (blue line in Fig. 7.5). To identify each peak in the photoelectron spectrum, a very crudely calculated photoelectron spectrum is overlaid with the experimental data.

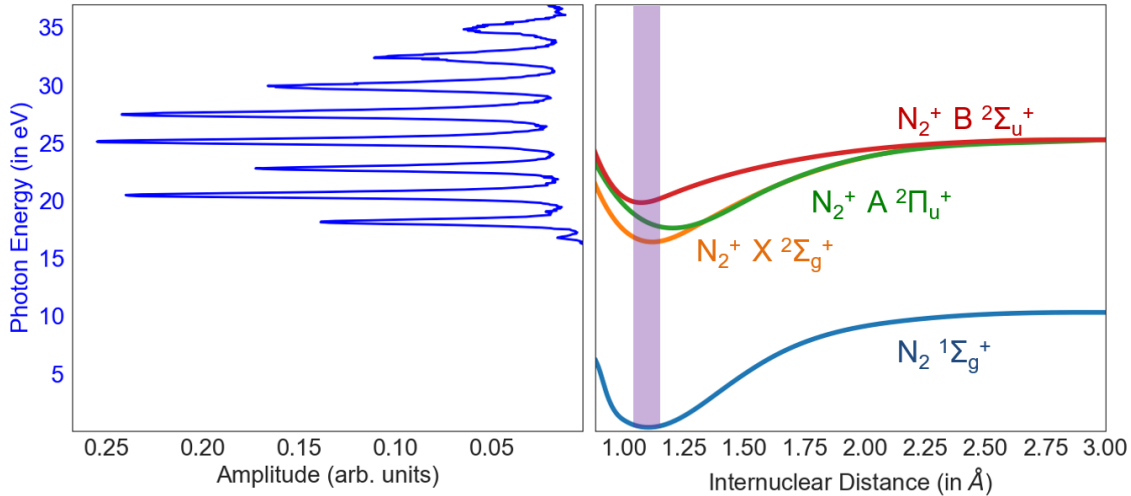


Figure 7.4: Left: XUV photon spectrum used for ionizing molecular N_2 , Right: the three lowest ionic bound PECs X, A and B respectively. The purple bar indicates the Franck-Condon overlap region

The calculated spectrum is obtained in two steps. First, a set of three Gaussian distributions with different widths and heights to mirror the transitions to the X, A and B states is taken. This would be used to replicate the spectrum obtained from one XUV harmonic. The strengths and spacing between these peaks is obtained from Synchrotron data[155]. By creating identical copies of these three distributions and adding offsets to each copy, the distributions that would result from a comb of XUV harmonics can be obtained. Each of these peaks is then multiplied with an appropriate factor to take into account the strength of each XUV harmonic. In this manner the photoelectron peaks can be easily identified.

From the figure, it is clear that the electron peaks from the X, A and B states are spread over almost 3 electron Volts and since the XUV harmonics have a spacing of 2.4 eV ($2h\nu_{IR}$), there is a significant amount of overlap between many peaks. This problem worsens in the presence of additional IR, since the signal from the sidebands and harmonics are strongly overlapped. Recalling from the previous chapters on RABBIT measurements, the harmonics and sidebands oscillate π radians out of phase with respect to each other. Since the two signals cancel out, it is therefore impossible to see any sideband oscillations.

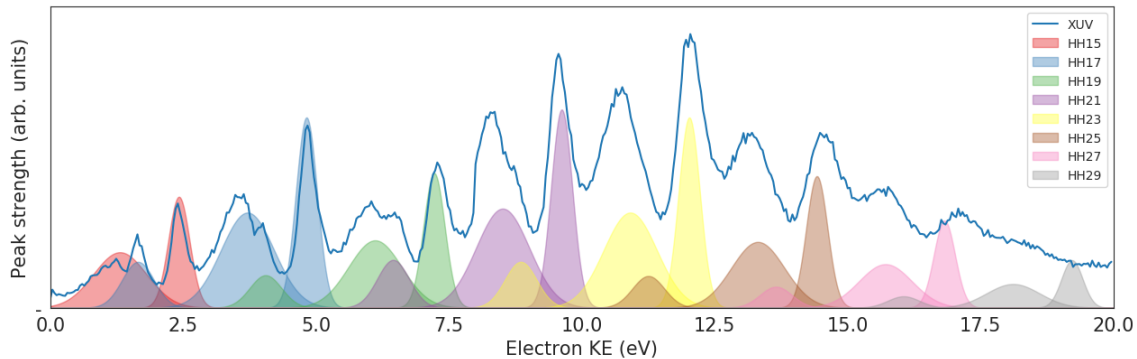


Figure 7.5: Experimentally measured photoelectron spectra (Blue line) overlaid with a calculated photoelectron spectrum for direct ionization of N_2 by XUV radiation.

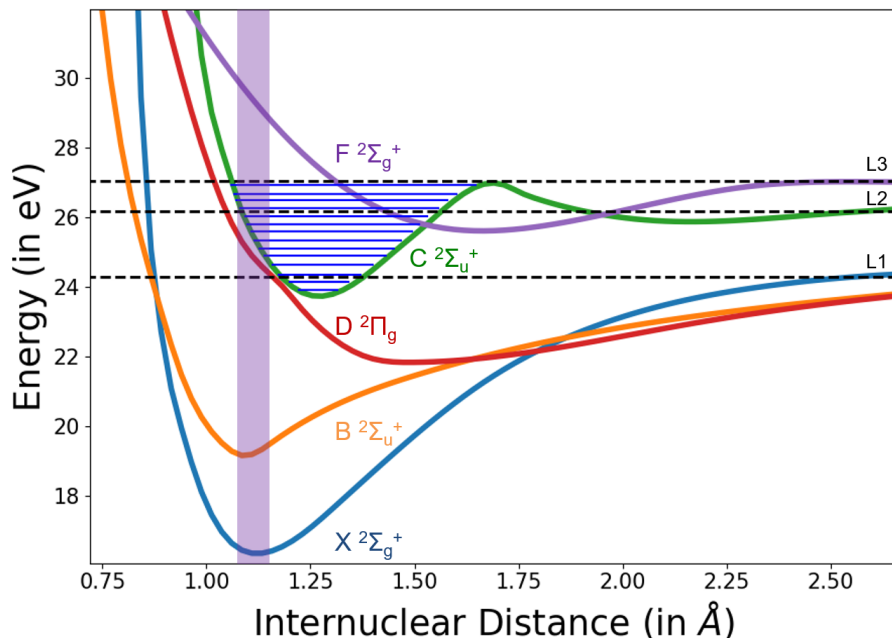


Figure 7.6: Potential energy curves relevant to the dissociation of N_2^+ ions.

7.1.2 Dissociation

For the dissociation channel however, the situation is slightly different. The molecular ion N_2^+ dissociates into an ion and a neutral through at three different thresholds for photon energies between 20 and 35 eV (Fig. 7.6). The dissociation thresholds L1 ($N(^4S^0) + N^+(^3P)$), L2 ($N(^4S^0) + N^+(^1D)$) and L3($N(^2D^0) + N^+(^3P)$) in Fig. 7.3, are at 24.29 eV, 26.19 and 26.68 eV respectively [156]. The electron kinetic energy spectrum is therefore a broad distribution due to the contributions from various dissociation thresholds (Fig. 7.7). In addition, the presence of a large

number of vibrational levels in the PECs leads to broadening of the peaks. The dissociation energy is shared with the ions through the KER and is usually a few electron volts. In Fig. 7.7, the plot for KER spectrum comprises of a series of peaks followed by a broad distribution.

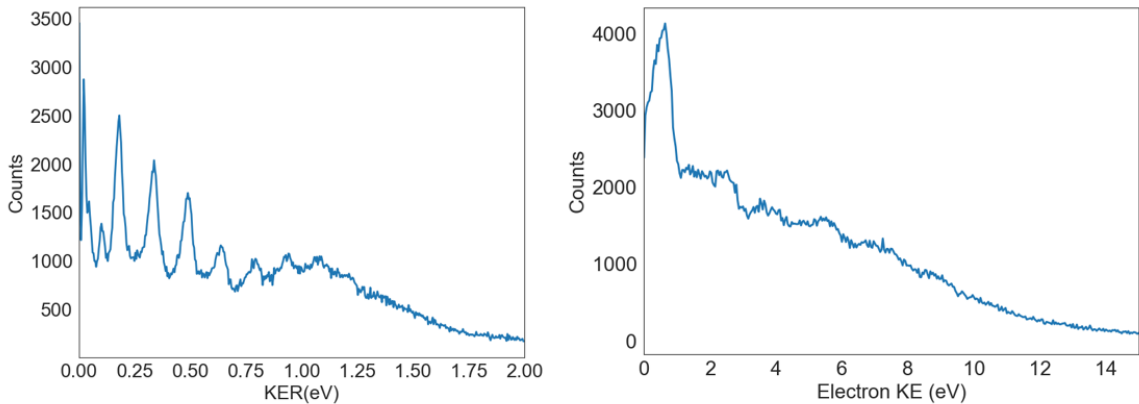


Figure 7.7: Left: KER distribution for N^+ ions, Right: Electron Kinetic energy distribution of electrons detected in coincidence with N^+ ions.

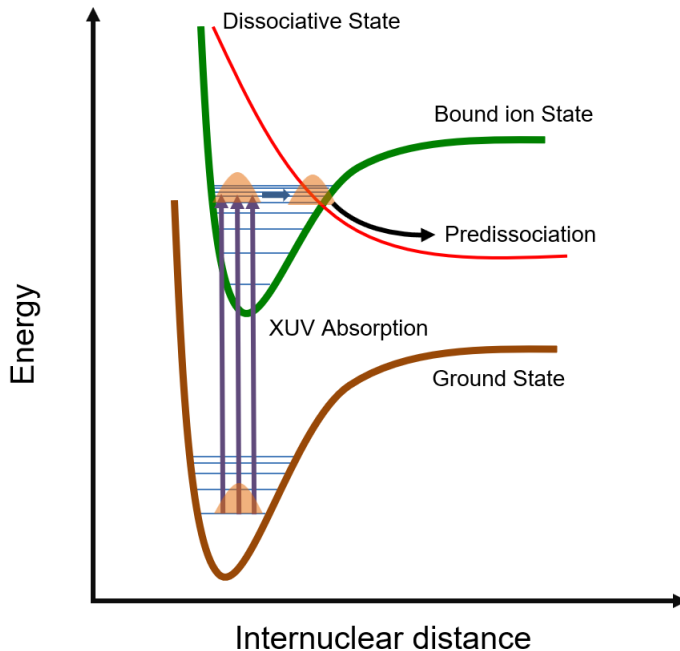


Figure 7.8: Schematic of the predissociation process

The KER distribution is usually very broad if a dissociative PEC is directly populated from the ground state, since the lifetime of these states is extremely short.

However, the presence of peaks in the KER distribution indicate that dissociation happens through an intermediate state that is long-lived. Comparing previous measurements and calculations provided in references [157, 158, 159], it can be concluded that these peaks in the KER are due to a process known as *Predissociation*[160]. Predissociation occurs, when there is a crossing between a bound PEC and a dissociating PEC (Fig.7.8). In this process, a nuclear wavepacket in a bound vibrational state dissociates when the vibrational wavefunction is in the proximity of such a crossing. In molecular nitrogen, this process has a lifetime ranging between a few nanoseconds to a few hundred nanoseconds [157]. Due to their relatively long lifetime, distinct peaks are seen in the KER spectrum coming from each of the vibrational levels that are in the proximity of a dissociating curve. To get a clearer understanding of the PECs that contribute to the peaks in the KER,

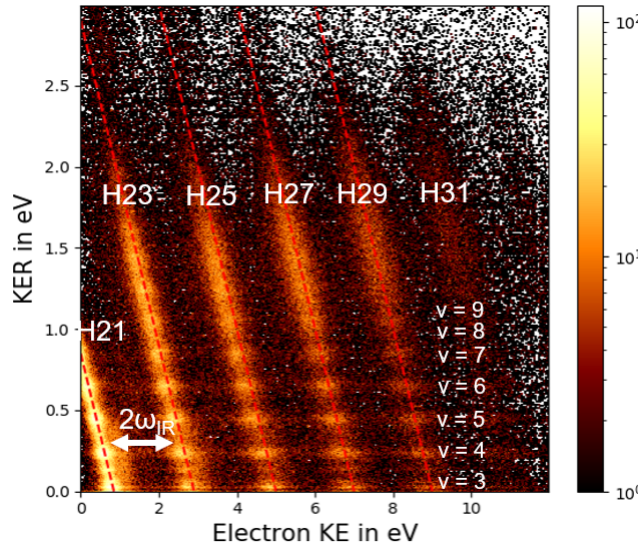


Figure 7.9: Joint energy spectrum for the dissociation of Nitrogen by XUV

we generate a joint energy spectrum(JES) as seen in Fig.7.9. This is a plot of the KER versus electron kinetic energies for all the $N^+ + N + e^-$ coincidences. There are two features that stand out in the join energy spectrum. First, there are events that fall along diagonal lines which have an energy spacing of $2\omega_{IR}$ and a slope of -1 (indicated by dashed lines). These lines are also called the harmonics and correspond to events from the dissociation of nitrogen by each XUV harmonic. The energy shared between the N^+ ions and electrons upon dissociation by 1 XUV harmonic is a constant value. This value is determined by the difference between the photon energy and the corresponding dissociation threshold. By momentum conservation, the sum of the KER and electron kinetic energies for each event in the diagonal is a constant. Hence all the events from one harmonic fall on a line with slope of -1 . The slope has a negative value since the ion and electron momenta have opposite signs.

Second, there are horizontal lines in joint energy spectrum that have energy

spacings resembling a vibrational progression of a PEC. Upon closer comparison with synchrotron data[157], these horizontal lines have the same spacing as the vibrational levels $v = 3, 4, 5, 6\dots$ in the PEC $C^2\Sigma_u^+$. This indicates that the peaks that appear in the KER are from the predissociation of the C state. The horizontal lines in the JES indicate also show that the predissociation of one vibrational level always results in the same KER and is independent of the incident XUV photon energy. The dissociation threshold L1 is closest to the vibrational levels of the C state. Since the L1 is threshold is below the vibrational levels $v \geq 3$, the progression in the JES can be assigned to these levels.

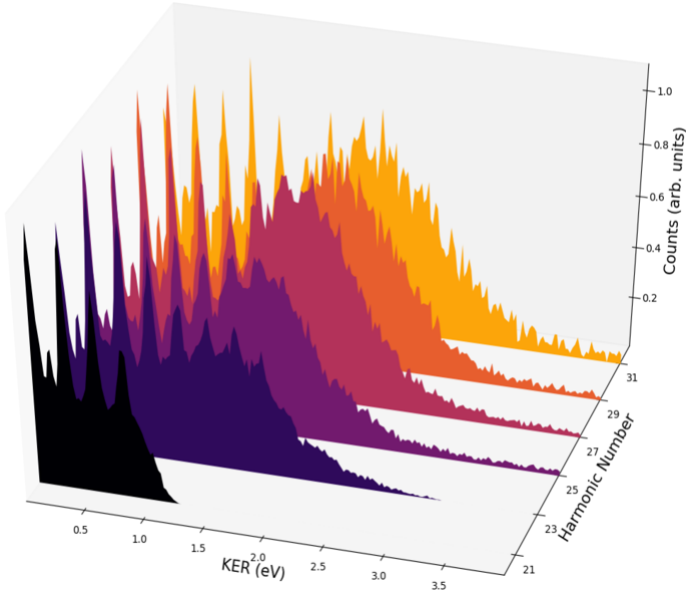


Figure 7.10: KER distributions for ionization by each XUV harmonic. The distribution for each harmonic is normalized to its respective maximum.

The exact pathways and the PECs through which the C-State predissociates is discussed in detail in references [159, 158, 157]. To briefly summarize, there are two PECs that could contribute to the predissociation of the C-state. One way is through the $^2\Pi_u$ PEC in Fig.7.3, which is a purely dissociating curve that crosses the C state to reach the dissociation threshold L1. The other is through a non-adiabatic exchange[161] with $B^2\Sigma_u^+$ state, which also reaches the L1 threshold.

At KERs above 1 eV, the horizontal lines are no longer clearly visible and merge into a broader distribution. As can be seen in the JES as well, the XUV photon energy increase leads to larger number of events with KER greater than 1 eV. This is because, with increasing photon energy, the $F^2\Sigma_g^+$ PEC is also populated[162]. In addition, the L2 and L3 threshold are also accessible from Harmonic 23 onwards. Since the F and C states cross each other, there is a population transfer from the F to the C state, which in turn dissociates through L1 threshold, resulting in KER values greater than 1 eV. with photon energies greater than 30 eV, the dissociation

happens directly through the L3 threshold. The increasing contribution of the F state with XUV photon energy can be seen with the help of a projection of the KERs for each harmonic. By applying a constant energy sum condition, all ions and electrons belonging to ionization by one harmonic can be chosen. From this, the KER distributions for each harmonic can be extracted, as shown in Fig.7.10. The distribution becomes broader and stronger with KERs greater than 1 eV, as the XUV photon energy increases, indicating stronger contributions from the L2 and L3 thresholds.

By choosing the electrons belonging to selected KERs, we obtain a photoelectron spectrum with discrete peaks with a spacing of $2\omega_{IR}$, similar to atomic photoionization (Fig. 7.11). This indicates that in the presence of a phase-locked IR pulse, sidebands can be formed, just as in the atomic case. By varying the XUV-IR delay, RABBIT spectra for electrons from each vibrational level can in principle be obtained.

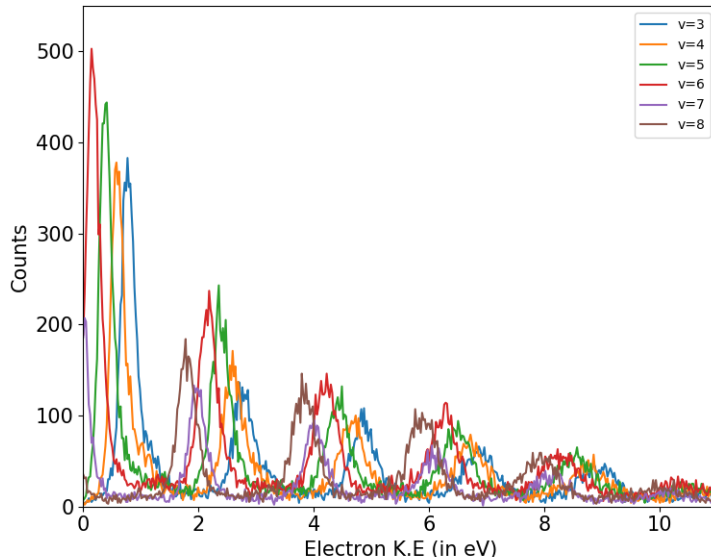


Figure 7.11: Electron kinetic energy spectrum upon ionization by XUV alone, obtained by choosing KER windows for the vibrational levels $v=3$ to $v=8$

7.2 Ionization of Nitrogen by XUV+IR

In this section, only the results of RABBIT measurements on the dissociation channel of nitrogen will be discussed. As mentioned in the previous section, for the direct ionization channel, no sideband oscillations are visible. This is due to an extremely strong overlap between the harmonics and sidebands, which cancel out

the sideband oscillations.

In the presence of an additional IR pulse after dissociation by XUV, the electrons undergo a $\Delta l = \pm 1$ transition similar to the atomic case and reach a sideband state. Provided that the electronic and nuclear dynamics are independent of each other, the sideband strength oscillates in when the delay between XUV and IR pulses is varied. The probe IR pulse also interacts with the nucleus before dissociation and induces transitions between the various PECs. Since neither the electron kinetic energy spectrum nor the KER distributions directly help us resolve any of the sidebands, we once again use the JES (Fig.7.12).

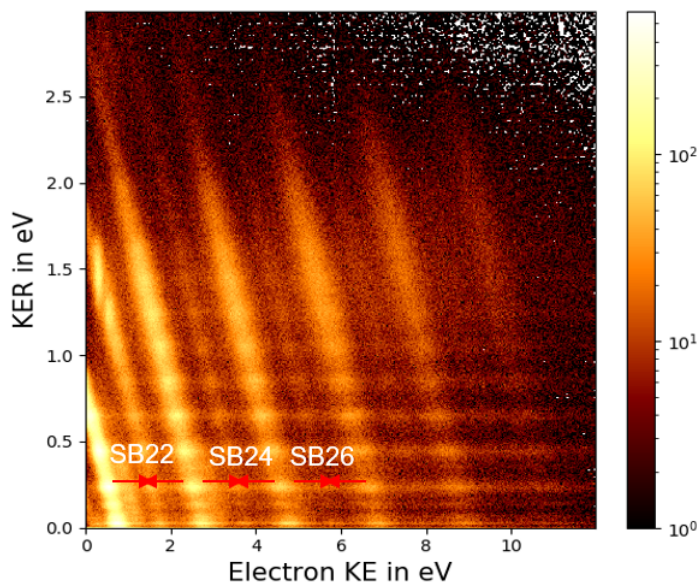


Figure 7.12: Joint energy spectrum for the dissociation of Nitrogen by XUV+IR

In the JES the sidebands appear in between the harmonics, on the diagonal lines which are separated by an energy of $1\omega_{IR}$ from the harmonics. There are four sidebands that are visible (SB 22-28) in this measurement. For KERs below 1 eV, the sidebands mimic the structure of harmonics. For KERs greater than 1eV, sidebands 24,26 and 28 continue to resemble the vibrational progression seen in the harmonics. Sideband 22 however shows a significant enhancement at KERs above 1 eV and no longer resembles the vibrational progression. By taking a closer look at the KER projections for each sideband (Fig. 7.13), it can be seen that the distribution peaks between 1.2 to 1.4 eV.

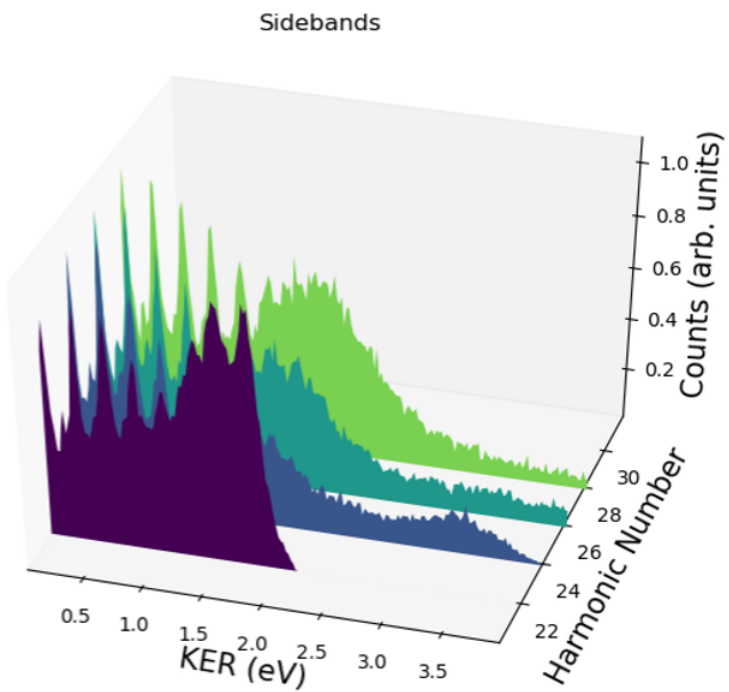


Figure 7.13: KER distributions for the sidebands. The distribution for each sideband is normalized to its respective maximum

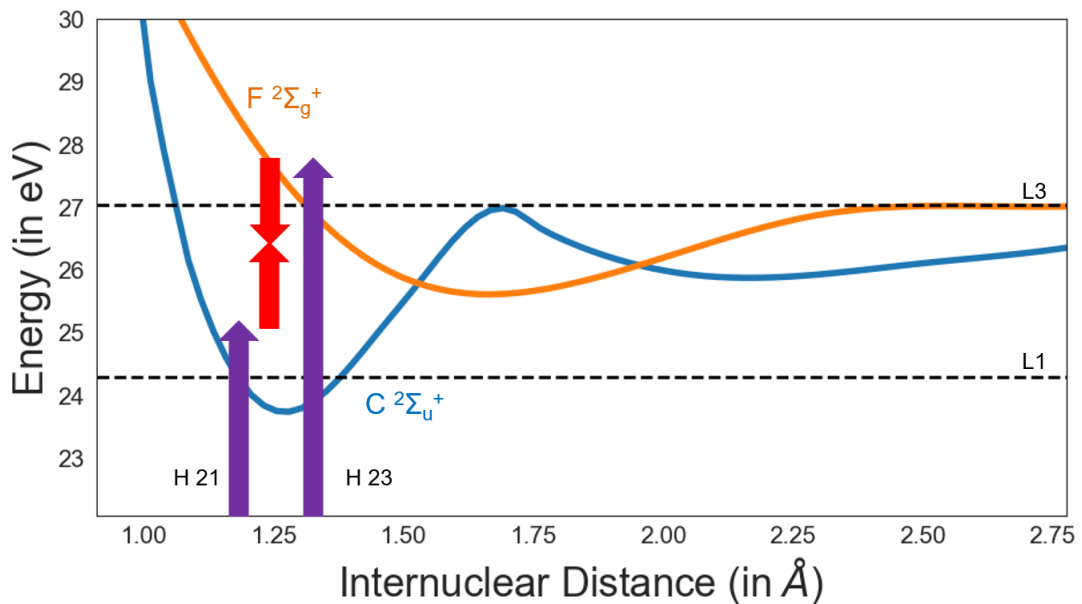


Figure 7.14: The two dissociation pathways associated with sideband 22.

The enhancement in KER at around 1.3 eV is due to an IR induced transition between the C and F states in the molecular ion. This can be visualized as shown

in Fig.7.14. Sideband 22 can be reached by absorbing harmonic 21 and an additional IR photon. Alternatively, it could also be reached by absorbing harmonic 23 to reach the F state and through the emission of an IR photon and a subsequent transition to the C state. The final state reached by the two pathways dissociate through the L1 limit. The energy difference between the final state reached by the two reaction paths and the L1 limit gets distributed in the KER. There are no enhancements of the KER for sidebands 24 to 28 since the F state dominates from harmonic 23 onwards.

To get the variation of the sideband amplitudes as a function of the XUV-IR delay, electrons corresponding to each vibrational level is chosen. The electron kinetic energies are then plotted as a function of the XUV-IR delay. Figure 7.15 shows the delay-dependent photoelectron spectrum for the vibrational levels 3,4 and 5 of the $C^2\Sigma_u^+$ state. Since the signal for the sidebands is very weak, a logarithmic colormap is used to visualize the data. The analysis however is done with a linear scale. By taking a projection of the sideband oscillations and carrying out the analysis as described in chapter 2, a Wigner like photoionization delay for molecular nitrogen could be measured. This method has also been used to measure attosecond delays in the dissociation of molecular hydrogen[32, 163].

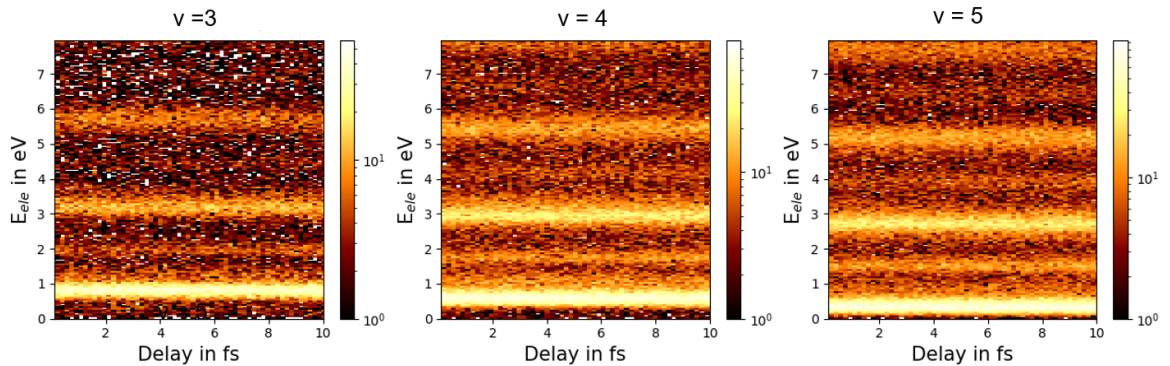


Figure 7.15: Photoelectron spectrum as a function of XUV-IR delay for the electrons from vibrational levels $v=3,4$ and 5

Upon analyzing the delay dependent spectra as described above, contrary to the atomic case and even the case of molecular hydrogen, there are no sideband oscillations that are visible for electrons from the levels 3,4 and 5. The same situation persists for all sidebands and all the vibrational levels and KERs above 1 eV. A Fourier analysis of the delay dependent spectra did not provide any clear evidence of the $2\omega_{IR}$ or $4\omega_{IR}$ oscillations as well.

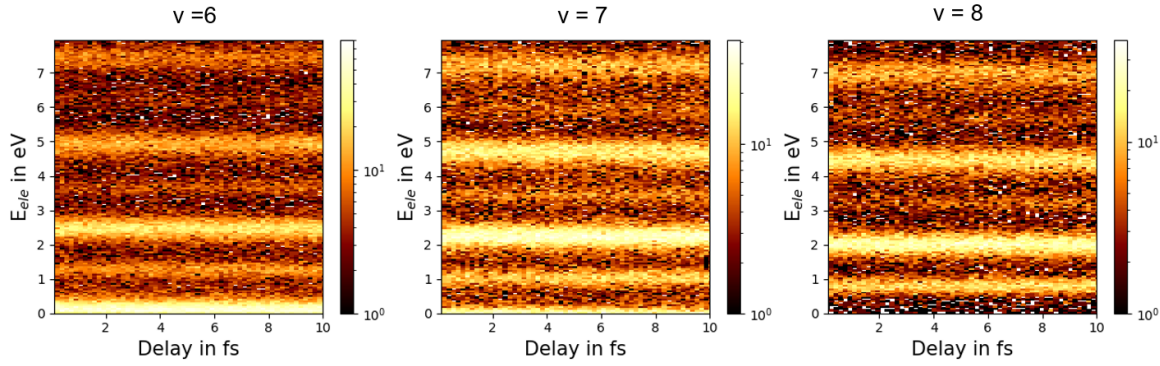


Figure 7.16: Photoelectron spectrum as a function of XUV-IR delay for the electrons from vibrational levels $v=6,7$ and 8

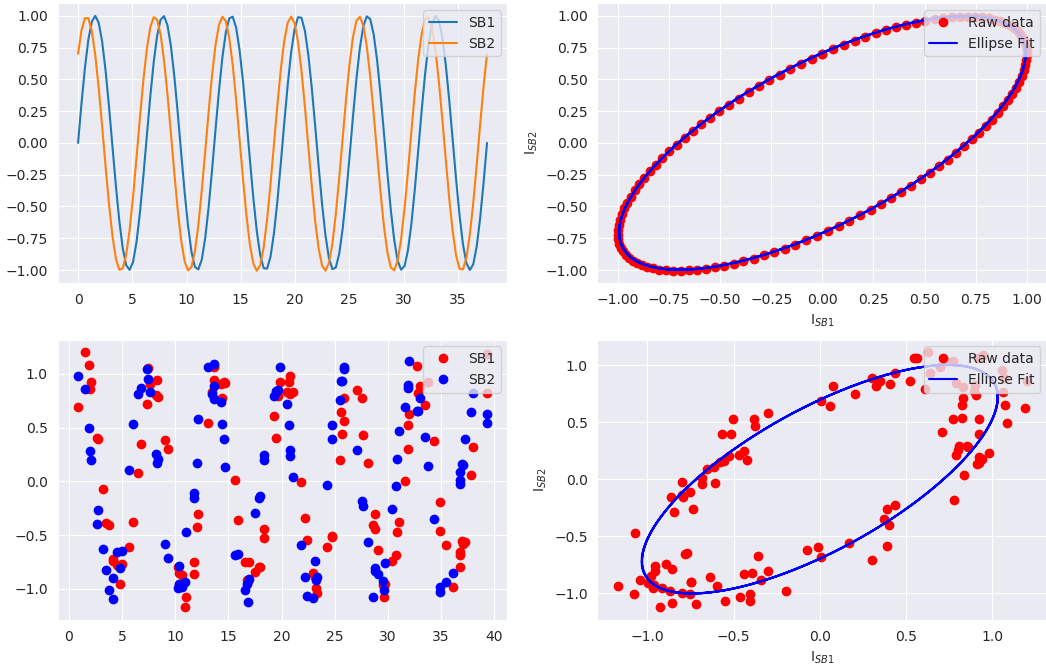


Figure 7.17: Top: Left: two ideal sinewaves with a constant phase shift, Right: Amplitudes of the two waves plotted and fitted with an ellipse. Bottom: Left: Projections of sideband oscillations from a RABBIT measurement on argon, Right: Map of the amplitudes and the ellipse fit.

The first reason that could be thought to cause this problem is a systematic error in the measurement. Although drift stabilization was used for this experiment, the long acquisition time could result in an abnormally large drift of the interferometer. To account for this possibility, a method proposed in Ref.[164] to extract

sideband oscillation phases where the interferometer drift is large, was used. The method basically utilizes the same principle used to generate the *Lissajous* figures. According to this method, the amplitudes of two noisy sine waves generated by the same source when plotted together lie on an ellipse, since the common mode noise cancels out. By fitting an ellipse to this distribution, the phase between the two sine waves can be obtained. This concept is visualized in Fig.7.17.

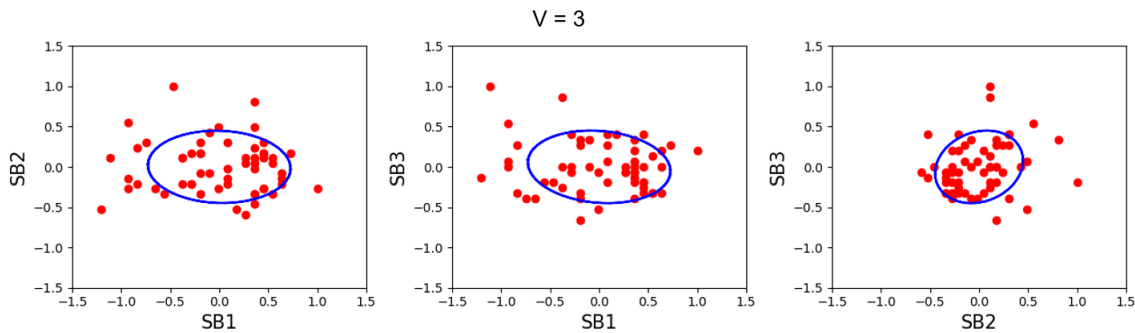


Figure 7.18: Amplitudes of the three possible pairs of sidebands for electrons from the $v=3$ state plotted and fitted with an ellipse

After testing the fit routine on atomic RABBIT datasets where there was a strong drift (see AppendixB), the fit was extended to retrieve the phases for the electrons from the various vibrational levels in nitrogen. As an example, the case for the vibrational level $v=3$ is shown in Fig.7.18. There are three sidebands that are visible in the XUV-IR delay spectrum for the $v=3$ state, as seen in Fig.7.15, taken as SB1, SB2 and SB3 in the order of increasing electron kinetic energy. The amplitudes for pairs of sidebands are plotted after ensuring they all have the same scaling.

Surprisingly, the points do not lie on an ellipse. An ellipse can be force fitted, but the phases so extracted would have very large error bars. With this, it is very clear that a systematic measurement error is perhaps not the reason for the lack of clear oscillations. The underlying reason hence must be related to the dissociation process itself.

As seen earlier, there are more than two PECs that contribute to the dissociation for KERs above 1 eV. At the instant of ionization, the electron wavepacket that leaves the molecule experiences a phase shift that depends on the final state of the molecular ion. During dissociation, since multiple PECs could result in the same KER, the electrons extracted for a given KER could have very different phases.

One way to separate the influences of various PECs on the outgoing electron's phase is to work in the molecular frame and selectively choose electrons that are emitted parallel and perpendicular to the molecular axis. This helps us to use the dipole selection rules for molecules effectively and separate the contributions from each transition. By using the simple formula $\vec{P}_{MF}^{N^+} = \vec{P}_{LF}^{N^+} + \frac{1}{2}\vec{P}_{LF}^{e^-}$, the ion momenta can be converted from the from the lab frame to the molecular frame. From this,

the angle of emission with respect to the molecular axis can be calculated[32]. When the polarization axis of the XUV and the molecular axis are parallel, the transitions are termed parallel and likewise, when the two axes are perpendicular, the transitions are termed perpendicular.

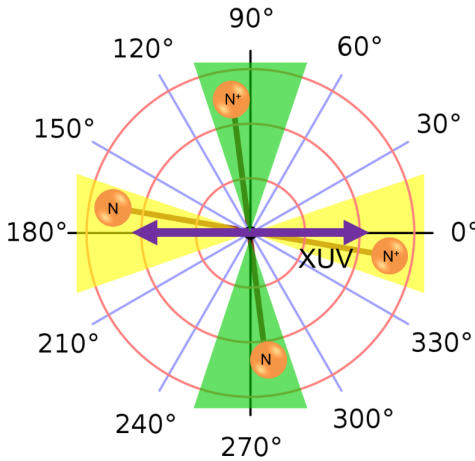


Figure 7.19: Schematic of the parallel(yellow) and perpendicular(green) transitions

From the joint energy spectra obtained for these transitions (Fig. 7.20) it is clear that the transitions that result in KERs above 1.2 eV are predominantly along the parallel direction. The vibrational progression from the predissociation process is however present in both transitions and cannot be completely isolated. The reason for this is the long lifetime associated with predissociation (several nanoseconds). The lifetime of predissociation is significantly larger than the rotational period for molecular nitrogen, which is in the picosecond timescale. Hence, the molecular orientation at the instant of predissociation can no longer be uniquely identified. From this it can be concluded that the signal from the predissociation process will always stay as a strong background.

In references [165, 166, 153], the KERs exhibit strong sub-femtosecond dynamics associated with the dissociation of nitrogen. This indicates that the electronic and nuclear wavefunctions evolve on a comparable timescale and the two processes can no-longer be thought of as independent of each other. Moreover, since a non-adiabatic pathway is anyway involved in predissociation, the electronic motion may not be decoupled from the nuclear motion after all. In other words, the nuclear outgoing electron wavepacket's phase is dependent on the nuclear wavepacket.

Therefore, with the information available so far, the concept of Wigner delays that are applicable generally to atoms and even diatomic molecules such as H_2 , D_2 and even CO can no longer be directly extended to the dissociation of molecular nitrogen. Clearly, theoretical calculations are needed to further investigate this

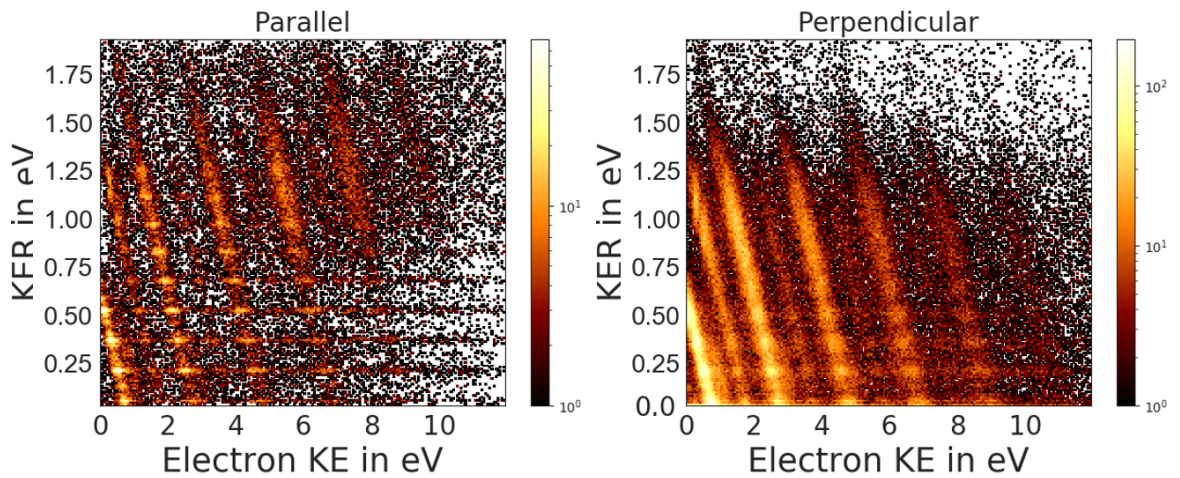


Figure 7.20: Joint energy spectra for the parallel and perpendicular transitions

complex interplay between the electron and nuclear dynamics. In addition, the phase retrieval for the sideband oscillations would also require a more elaborate method.

Conclusion and Outlook

To summarize and conclude, XUV-IR pump-probe measurements were successfully performed with a high-repetition rate laser and a Reaction Microscope. The drift of the Mach-Zehnder interferometer, which was a key technical challenge towards acquiring high-quality data has been successfully reduced with the help of active stabilization.

With a high temporal stability, XUV-IR pump-probe measurements on atomic krypton, argon dimers and molecular nitrogen were performed to get insights into atomic and molecular dynamics at the attosecond timescale. By measuring over an atom, dimer and a diatomic molecule, a variety of phenomena related to photoionization have been covered.

The angle-resolved measurements on Krypton complements previous measurements, and clearly indicates that the spin-orbit interactions play a significant role in photoionization delays. The results from these measurement can serve as a reference for theoretical calculations, particularly around the $4snp$ resonances, where there are no Wigner delay calculations published till date. Measurements on argon dimers reveal the role of Van der Waals forces in the photoionization of dimers and reveal the possibility of observing two-center interferences in molecular photoionization. In addition, the presence of a noticeable contribution from the Interatomic Coulomb decay of argon dimers indicates great potential to observe this process with attosecond time resolution.

The measurements on nitrogen reveal the role of an intriguing process called predissociation on the dynamics of the outgoing electron wavepacket. While there is still ambiguity about the absence of sideband oscillations in the dissociation channel, the experiment reveals a complex interplay of electron-nuclear dynamics and goes on to show that a simple Wigner like delay for molecular electrons is not applicable here.

To further expand on the results presented here, additional work is being carried out on both the theoretical and experimental fronts. At the time of writing this thesis, a RABBIT measurement on a mix N₂ and Argon at the 150 KHz repetition rate is being planned. The switch to a higher repetition rate involves significant changes to the data acquisition system and hence was not attempted earlier. Also, by using a gas mixture, it would now be possible to look for sideband oscillations in electrons from both argon and nitrogen simultaneously. With such a measurement, the effects of any possible interferometer drift over long acquisition times can be eliminated.

The planned measurement on nitrogen will be done with significant changes to the beamline. The second harmonic of the laser would be used to generate the XUV harmonics as well as the probe pulse. Doing this would make it possible to perform RABBIT measurements with a large spacing between each harmonic in the XUV comb. Since the second harmonic is used for HHG, each XUV harmonic will be about 4.8 eV apart. This would therefore make it possible to observe sideband oscillations in the direct ionization channel of nitrogen and perhaps study phenomena such as shape resonances[154] with attosecond precision.

The optics used in the beamline for RABBIT measurements with the IR laser pulses cannot be used for the experiments with the second harmonic of the laser. Hence, all the mirrors in the Mach-Zehnder interferometer need to be replaced. As a first step however, only the HHG arm of the interferometer was adapted to include a BBO crystal and thereby create XUV with the second harmonic (Fig. 7.21). The probe arm of the interferometer was left unmodified and a RABBIT measurement was performed on argon and neon. Such a configuration results in 3 sidebands instead of just one and is a very effective tool to study continuum-continuum transitions. The results of this work are published in Ref. [167].

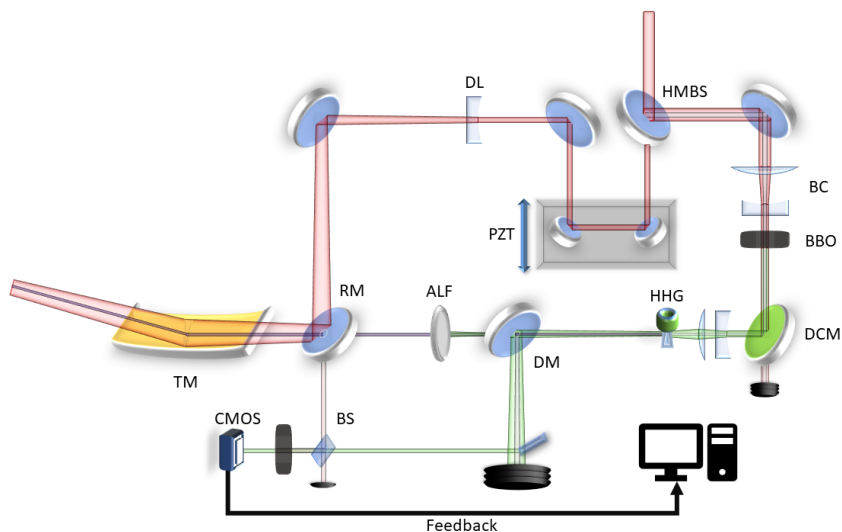


Figure 7.21: Schematic of the modified beamline to perform "3-Sideband RABBIT" measurements, BBO - Beta Barium Borate crystal, BC - Beam collimator, DCM - Dichroic mirror. The rest of the labels have the same meaning as in Fig. 4.2

Finally, new HHG target designs are being tested at the moment which can help increase the cutoff energy of the XUV harmonics. This is aimed towards obtaining a stronger signal from the ICD dissociation channel of argon dimers.

A Beta parameter estimation

The angular distribution of electrons can be fitted with a *Legendre* polynomial to obtain the beta parameters. The fits were tested using Legendre polynomials simulated with noise, as shown below.

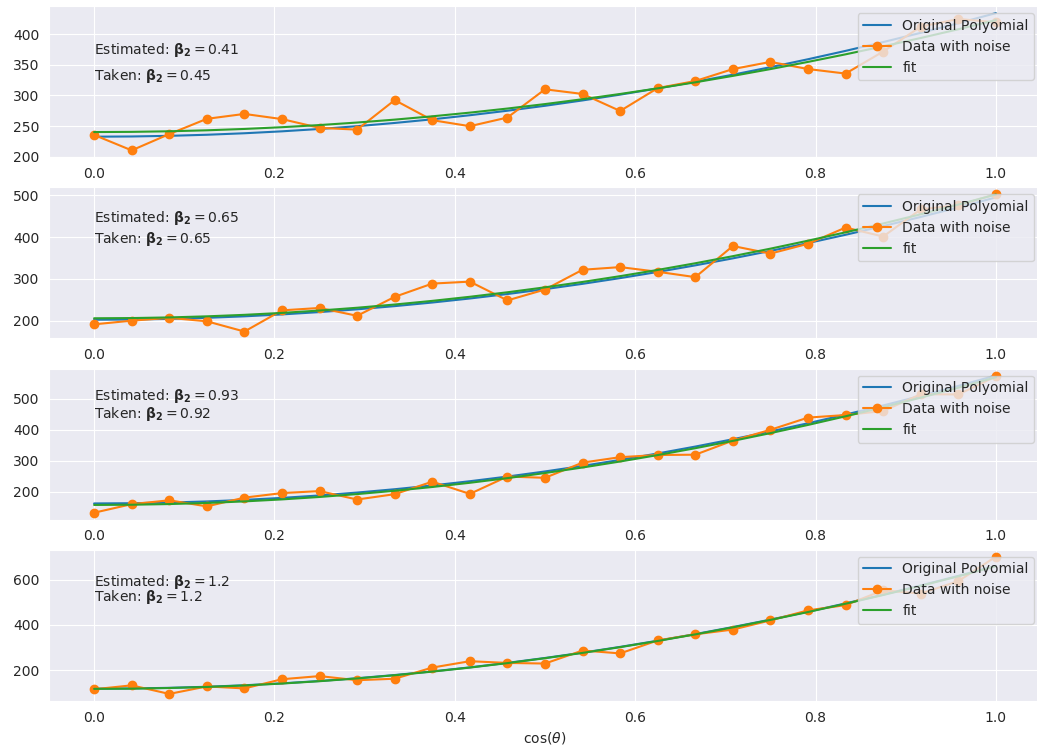


Figure A.1: Simulated data to test the Legendre Polynomial fit

APPENDIX A. BETA PARAMETER ESTIMATION

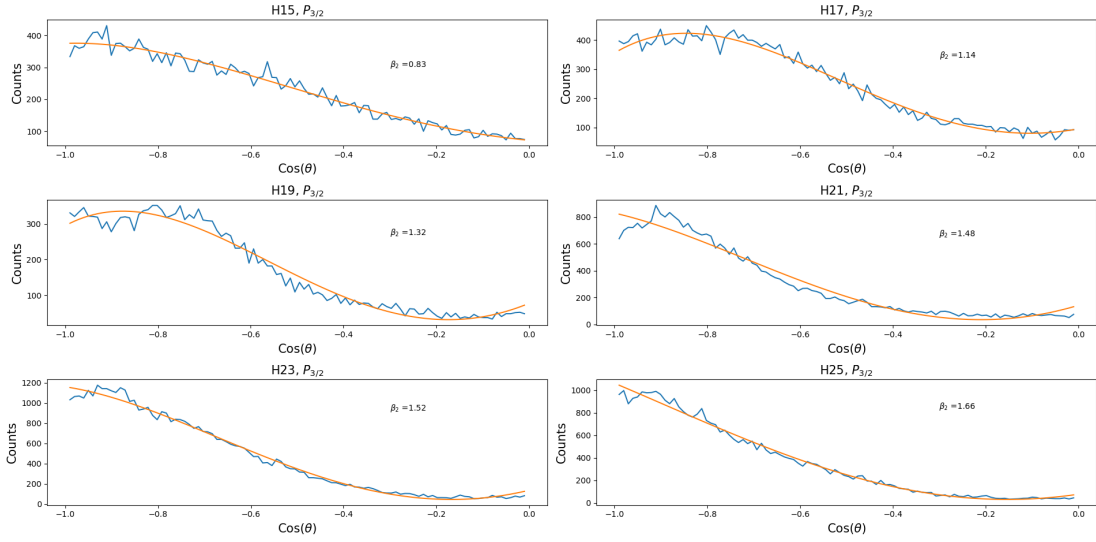


Figure A.2: Beta Parameter fits for the $P_{3/2}$ electrons obtained by XUV ionization

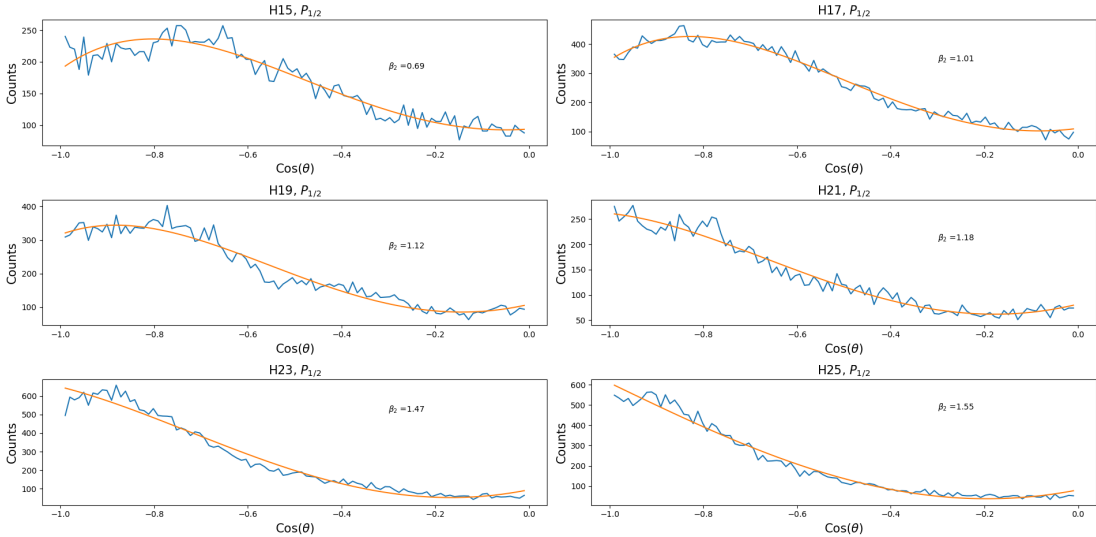


Figure A.3: Beta Parameter fits for the $P_{1/2}$ electrons obtained by XUV ionization

B Ellipse Fit test data

In order to retrieve the sideband oscillation phases from RABBIT measurements where the interferometer drift was very large, the TURTLE method [164] was used. This method uses an ellipse fit to determine the phase difference between two sine waves. The fit routine was tested using a RABBIT measurement on helium, where during the course of the measurement, the interferometer drift was so strong that it smeared out the oscillations.

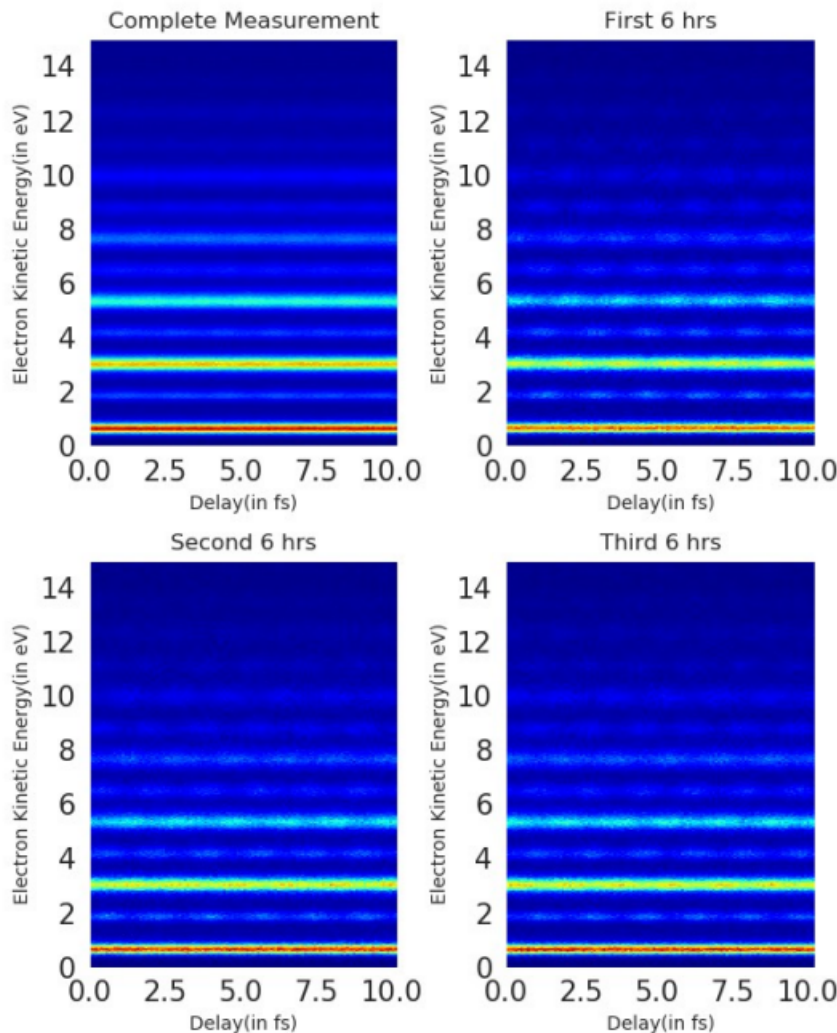


Figure B.1: RABBIT measurement on Helium lasting about 18 hours. When divided over every 6 hours is taken separately, the oscillations are visible. When put together, the oscillations are smeared out.

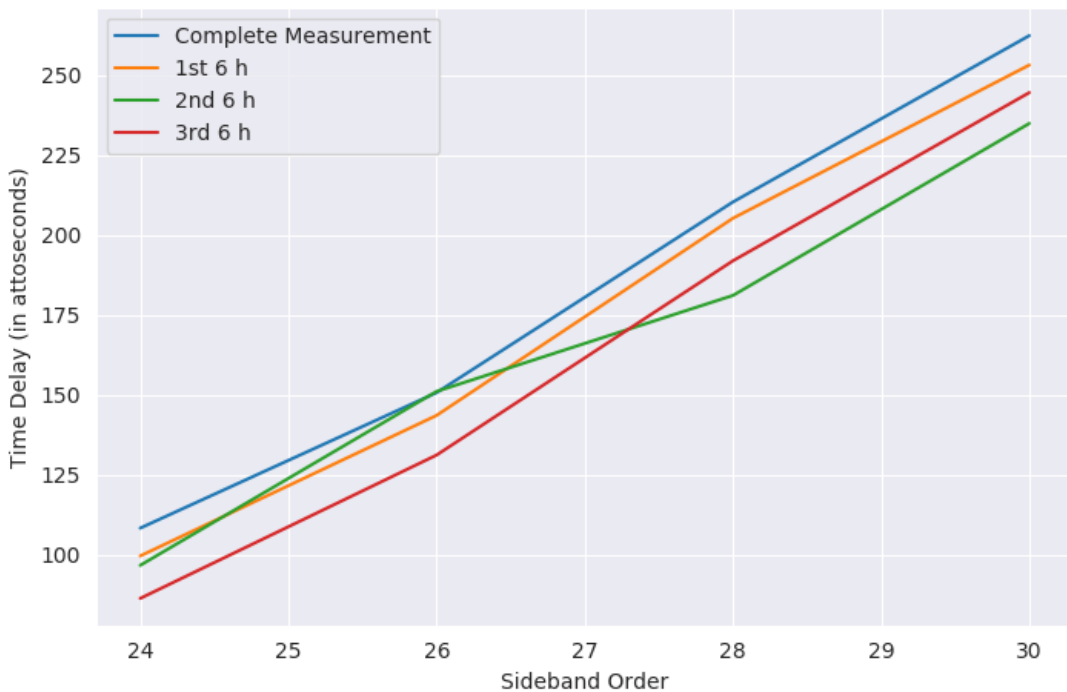


Figure B.2: Time delays extracted using the ellipse fit method

C Atomic Units

For simplicity, the constants in the electronic Schrödinger Equation can be set equal to one atomic unit. Therefore $\hbar = m_e = e = 4\pi\epsilon_0 = 1a.u$ The other units can be calculated as:

Quantity	Definition	SI Value
Time	$a_0(\alpha c)^{-1}$	$2.41888433 \times 10^{-17}\text{s}$
Energy	$m_e(\alpha c)^2$	$44.3593 \times 10^{-34}\text{ J}$
Mass	m_e	$9.1093897 \times 10^{-31}\text{kg}$
Charge	e	$1.6021773 \times 10^{-19}\text{C}$
Length	Bohr Radius a_0	$5.29177249 \times 10^{-11}\text{m}$
Momentum	p	$1.9929.10^{-24}\text{Kg m/s}$
Angular Momentum	\hbar	$1.0545887 \times 10^{-34}\text{Js}$
Velocity	αc	$2.18769142 \times 10^8\text{m/s}$

Table adapted from [32]

D Lists

D.1 List of Figures

0.1	Schematic of a pump-probe measurement. Figure adapted from [3]	8
1.1	Left : Schematic of the removal of a valence electron by absorbing a single XUV photon, Right: Schematic of Multi-Photon Ionization, by absorption of multiple IR photons	13
1.2	Experimentally measured ATI Photoelectron spectrum obtained by ionizing Argon with femtosecond IR pulses	14
1.3	Schematic of tunnel ionization	14
1.4	Schematic of the Three-Step model for high-harmonic generation. The three steps are: tunneling, acceleration and recollision	15
1.5	Top: A Train of attosecond pulses produced in the time domain by a long IR pulse. Bottom : XUV Frequency comb obtained from the Fourier transform of an attosecond pulse train. Figure taken from [19]	16
1.6	Classical trajectories for the electron in an oscillating field, calculated using eq. 1.21	17
1.7	A visualization of the XUV emission at the focus of an intense laser beam. Left : Improper phase matching ($\Delta K \neq 0$) of the XUV from single atom emitters, Right : Optimal phase matching ($\Delta K = 0$) between the various XUV photons emitted from each atomic emitter.	18
1.8	A photograph of the plasma created while generating XUV by focusing femtosecond IR pulses onto a gas cell.	19
1.9	Experimentally measured electron spectrum obtained by the XUV ionization of noble gases. The double peak structure seen in Krypton is due to the spin-orbit splitting (discussed in Chapter 5). The dashed vertical lines indicate the respective ionization thresholds. .	20
1.10	Reconstructed photon spectrum obtained from the photoelectron spectrum of Argon	21
1.11	Coordinate system for a diatomic molecule	22
1.12	Visualization of the rotation and vibration degrees of freedom for a diatomic molecule	22
1.13	Schematic of a molecular potential as a function of internuclear distance. Figure adapted from [30]	23

1.14 Table of dipole transitions in homonuclear diatomic molecules. and \perp show allowed parallel and perpendicular transitions, while x indicates forbidden transitions. Adapted from [32, 20]	25
1.15 Left: Schematic of transitions between molecular vibrational levels, governed by the Franck-Condon principle. Figure adapted from [35]. Right : The bold line shows the strongest transition allowed by the Franck-Condon principle. Figure adapted from [30].	26
1.16 Left: Calculated potential energy curves for molecular nitrogen, with a vertical bar showing the Franck-Condon allowed region. Data for PECs taken from [36]. Right : Experimentally obtained photoelectron spectrum after ionizing N ₂ by a XUV harmonic.	27
2.1 Schematic of the formation of sidebands and the corresponding photoelectron spectrum obtained from an experiment	29
2.2 Variation of sideband intensity as a function of the phase between XUV and IR pulses	30
2.3 Experimentally recorded RABBIT trace for electrons from the ionization of helium atoms	30
2.4 Examples of long and short trajectories in HHG	31
2.5 Propagation of electron wavepackets with various kinetic energies in the vicinity of a Coulomb potential (black lines) in comparison to a freely propagating electron having the same kinetic energy (gray lines). Figure taken from [52].	32
2.6 Projection of Sideband 24 in Helium (integrated over electron KE 4.0 - 4.5 eV in Fig.2.3) and the cosine fit for the oscillations	34
2.7 Left: RABBIT trace from Fig. 2.3, Center : Linewise FFT showing the presence of only $2\omega_{IR}$ component in the sideband oscillations, Right: Phase retrieved from the FFT for each energy bin. The harmonics and sidebands oscillate almost π radians out of phase w.r.t each other.	35
2.8 Example of a linewise Fourier transform for a RABBIT measurement performed on Argon with a very high probe IR intensity. Multi-photon transitions in the continuum due to the high IR resulted in a noticeable contribution of the $4\omega_{IR}$ oscillation in the RABBIT trace.	36
2.9 Left: Projections of sideband oscillations seen in Fig. 2.3. The yellow line tracks the relative phase between the oscillations. Right: The phases converted to time delays(red points) along with the linear fit (dashed blue line).	36
2.10 Left : Experimental RABBIT trace from a measurement on Argon, Right: Top - The XUV group delays extracted from the RABBIT trace, Bottom - XUV photon spectrum obtained from the photo-electron spectrum. The area shaded green denotes the harmonics chosen for pulse reconstruction	38

2.11 Top : Attosecond pulse train retrieved using the XUV spectrum and group-delays from the RABBIT trace, Bottom : The envelope of the retrieved pulse with chirp in comparison to the Fourier Limited pulses for the bandwidth	39
3.1 The laser's seed and amplification stage. Figure taken from [73]	41
3.2 A schematic of the Hollow Core Fiber compressor stage of the laser. Figure taken from [77]	41
3.3 Schematic of the beamline. Figure taken from [32]	42
3.4 Zoomed in view of the interferometer, containing the HHG and recombination chambers. Legend: HMBS - Holey Mirror Beam Splitter, FL - Focusing Lens, NZ - Gas Nozzle, PC- Differential pumping cone, DM - Dump Mirror, IR- Iris, ALF - Aluminium Filter, RM - Recombination Mirror, PZT - Piezo Stage, DL - Diverging Lens	43
3.5 Schematic of the toroidal mirror. Axes A, B and C refer to the Pitch, Roll and Yaw axis respectively.	44
3.6 A schematic of the Reaction Microscope. Figure taken from [88]	45
3.7 Schematic of the target gas jet undergoing supersonic expansion	46
3.8 3D CAD drawing of the Spectrometer. Figure taken from [32]	46
3.9 Schematic of the working of the MCPs in conjunction with the Delay line anodes. Figure taken from [88]	47
3.10 Schematic of the Delay Line Anode (figure taken from [88]). Based on the time taken for the signals to reach the end of the grid, the position of the hit on the detector is determined.	48
3.11 Exemplary images of the electron(left) and ion(right) detectors. The concentric rings visible on the electron detector correspond to the electrons coming from ionization by the XUV comb.	51
3.12 Projection of the helical motion on the detector plane. Figure taken from [88]	51
3.13 A plot of the radius of cyclotron motion versus the time of flight for the electrons	52
3.14 Experimental momentum distributions for N_2^+ ions, from the ionization of an N_2 gas jet with XUV. From the gaussian fits, the resolution for each momentum can be determined	53
4.1 Example of a RABBIT trace where the sideband oscillations are smeared out over time, due to thermal drifts.	54
4.2 Modified Interferometer to include Active-Interferometric Stabilization. Note : HMBS - Holey Mirror Beamsplitter, FL- Focusing Lens, HHG - Gas Nozzle, DM - Dump Mirror, ALF - Aluminium Filter, RM - Recombination Mirror, BS - Beam Splitter, PZT - Piezo Translation Stage, DL - Diverging Lens, CMOS - Camera, TM - Toroidal Mirror .	55

4.3	Left: False color representation of the interference fringes as seen on the camera, Center: Integrated signal over the selected region of the image, Right: Absolute value of the Fourier transform	56
4.4	Imaging the focus inside the REMI with the help of a focusing lens, placed at 2f from the interaction region.	57
4.5	Tracking the interference signal from the extended interferometer and the actual interferometer	58
4.6	A schematic of the drift stabilization mechanism	59
4.7	Left : Input voltage to the ADC as a function of time, Right : ADC readout	60
4.8	Left: Drifts from the unstabilized interferometer, Right: Drifts after locking the interferometer	61
4.9	Delay Scan performed with the active stabilization	61
4.10	Left : Input voltage to the ADC as a function of time. The same signal was used to drive the piezo stage earlier, without active stabilization. Right : ADC readout over several scans.	62
4.11	Comparison of RABBIT Spectrograms obtained with and without active stabilization	63
4.12	Quantifying the drift in sideband oscillation phases in a RABBIT measurement over 1 hour with and without stabilization. Top: Projections of the sideband oscillations (SB 22) for each 15 minute slice of the dataset. Bottom: Temporal drift with respect to the data from first 15 minutes.	64
4.13	Bottom: RABBIT spectrum for photoionization of Argon, Top: Photoelectron spectrum integrated over all time delays and the respective sideband oscillation phases. The data was recorded over 13 hours.	65
4.14	Top: Projections of SB22 from each 1 hour slice, Bottom: Drift of the sideband oscillations in SB20 - SB24 over 12 hours	66
4.15	Top: Build-up of signal in sideband 22 over 13 hours, obtained by adding the sideband oscillations, Bottom : Change in sideband oscillation contrast upon adding data over time	66
5.1	Pictorial representation of the Spin-orbit coupling. Left - electron in a classical orbit around the nucleus, Right - Vector addition of the orbital angular momentum and spin.	69
5.2	Photoelectron Spectrum of Krypton ionized by XUV radiation. The spectrum is obtained by integrating the photoelectron signal for electron emission angles between $0 - 65^\circ$ w.r.t respect to spectrometer axis.	70
5.3	Formation of Sidebands in Krypton. The $P_{\frac{3}{2}}$ levels from neighbouring harmonics lead to the formation of corresponding sidebands. The same happens with the $P_{\frac{1}{2}}$ levels as well.	71

5.4 Left : Experimental RABBIT trace for Krypton, Right: Spectrum for the electrons coming from the ionization of XUV alone v/s Delay	72
5.5 Left : Spectrogram obtained by performing a linewise Fast Fourier transform along the delay axis for each kinetic energy bin, Right : Phases estimated from the Fourier Transform	73
5.6 Projections of the sideband oscillations for SB 18. These projections were obtained by choosing the energy windows 7.2 – 7.6 eV and 6.6 – 6.9 eV in Fig.5.5 for the $P_{3/2}$ and $P_{1/2}$ electrons respectively.	73
5.7 Left: Phases of sideband oscillations. Right: Difference in time delays for the electrons from the $P_{3/2}$ and $P_{1/2}$ levels	74
5.8 Theoretically calculated τ_{Wigner} values for the $4p_{3/2}$ and $4p_{1/2}$ electrons. There are no data points calculated between 24 to 32 eV photon energy, due to the presence of $4s4p^6np$ resonances. Figure taken from [111].	75
5.9 Left : Delay differences for the $P_{3/2}$ and $P_{1/2}$ electrons. Green lines indicate $4s4p^6np$ (n=5,6,7,8) resonances. The data for resonances is taken from [117]. Right: Experimentally observed $4s4p^6np$ resonances. Figure taken from [118].	75
5.10 Transitions arising from XUV ionization, from a bound np state to $\epsilon d, \epsilon s$ states in the continuum for the $P_{3/2}$ and $P_{1/2}$ ionic states.	76
5.11 Left : Momentum distribution of the electrons along the longitudinal and transversal direction, upon ionization by XUV. Right : Electron kinetic energy v/s cosine of the angle of emission.	76
5.12 Blue: Angular distribution of the $P_{3/2}$ electrons ionized by harmonic 15, Red: Legendre polynomial fit. The details of the fit and the individual plots for each harmonic are provided in Appendix A.	78
5.13 Experimentally obtained β_2 parameters for Krypton. Blue points: XUV ionization of Krypton. Red points: Synchrotron measurements reported in [123]	78
5.14 Left: Theoretically calculated variation of the asymmetry parameter in Krypton, for single photon ionization around the $4s4p^55p$ resonances. Figure taken from [118]. Right: Top: Theoretically calculated total ionization cross section variation, Bottom : Experimentally measured variation of β_2 values around the n=5 resonance. Figure taken from [114]	79
5.15 Left : Angular distribution of electrons from a RABBIT measurement on Krypton, integrated over all delays, Right : Top : RABBIT traces for electrons emitted at 0 to 10 and 30 to 40 degrees respectively, Bottom : Sideband phases as a function of emission angle for SB 16.	80
5.16 Difference in photoionization delays between the $P_{3/2}$ and $P_{1/2}$ levels as a function of angle of emission, for the various sidebands.	81

6.1	$\ln P - \ln T$ diagram for a gas which condenses upon expansion. Figure adapted from [133].	83
6.2	Potential energy curve for the Ar_2 ground state along with the first few vibrational levels. The data for the potential energy curve and the vibrational levels is taken from references [136, 137, 138] . . .	84
6.3	Time-of-flight spectrum for ions, from the ionization of an argon gas target by XUV and IR	84
6.4	Left: Photoelectron spectrum integrated over all delays for electrons detected in coincidence with monomers and dimers respectively. Right: An inset showing an almost 0.2 eV spacing between the kinetic energies of electrons.	85
6.5	Calculated potential energy curves(PECs) of the neutral argon dimer and the argon dimer ion. The data for the PECs is taken from Ref.[141, 142]	86
6.6	Left : Visualization of the superposition of <i>gerade</i> and <i>ungerade</i> states of the Ar_2^+ ion and the charge localized on one side, Right : The brown colored wave is a freely propagating wavepacket with kinetic energy E and the blue colored wave is the phase shifted wavepacket of the same kinetic energy, experiencing scattering by the dimer potential	87
6.7	(A): RABBIT trace for electrons detected in coincidence with the monomer ions (Ar^+), (B): RABBIT trace for electrons detected along with the dimer ions (Ar_2^+), (C): Top - Projection of Sideband 22 from (A) , Bottom - Projection of Sideband 22 from (B)	88
6.8	Sideband oscillation phases for the electrons detected in coincidence with Argon dimer and monomer ions respectively, Right : Time delay differences for the each sideband	89
6.9	Time delay differences for each sideband	89
6.10	Angular distribution of the low energy electrons detected in coincidence with the monomer and dimer ions respectively.	90
6.11	Formation of SB 14, through under-threshold excitation of Argon by Harmonic 13 and subsequent ionization by IR	90
6.12	Schematic of the "direct" dissociation pathway	91
6.13	Schematic of the "indirect" dissociation pathway	92
6.14	KER Distribution of Argon ions. The region shaded red corresponds to ions from the "direct dissociation" while the region shaded green corresponds to "indirect" dissociation	92
6.15	A plot of the time of flight of the ions versus the X coordinate of the hits on the ion detector	93
6.16	Angular distribution of the electrons corresponding to the direct and indirect dissociation channels	93

6.17 Left: Potential energy curves showing the decay of various excited states of Ar_2^+ ions. Of particular interest here is the transition that results in ICD (red curve). PECs taken from [145]. Right : ICD in Ar_2 . (A) $3s$ ionization by XUV, (B) $3p \rightarrow 3s$ decay and $3p$ ionization through a virtual photon, (C) Dissociation via Coulomb explosion.. .	94
6.18 Photoion-Photoion Coincidence Spectrum (PiPiCo) ToF1 of the first particle reaching the detector plotted versus the ToF2 of the second particle for photoionization of Ar_2	95
7.1 Time of flight of ions detected after ionizing N_2 as a target in the REMI	98
7.2 A 2D histogram mapping the ion time of flights with the X coordinate of the ion positions on the detector. The rings are formed by dissociation from various vibrational levels in the PEC.	98
7.3 Potential energy curves for neutral N_2 and the ionic ground state N_2^+ . Figure taken from [36]	99
7.4 Left: XUV photon spectrum used for ionizing molecular N_2 , Right: the three lowest ionic bound PECs X, A and B respectively. The purple bar indicates the Franck-Condon overlap region	100
7.5 Experimentally measured photoelectron spectra (Blue line) overlaid with a calculated photoelectron spectrum for direct ionization of N_2 by XUV radiation.	101
7.6 Potential energy curves relevant to the dissociation of N_2^+ ions.	101
7.7 Left: KER distribution for N^+ ions, Right: Electron Kinetic energy distribution of electrons detected in coincidence with N^+ ions.	102
7.8 Schematic of the predissociation process	102
7.9 Joint energy spectrum for the dissociation of Nitrogen by XUV	103
7.10 KER distributions for ionization by each XUV harmonic. The distribution for each harmonic is normalized to its respective maximum.	104
7.11 Electron kinetic energy spectrum upon ionization by XUV alone, obtained by choosing KER windows for the vibrational levels v=3 to v=8	105
7.12 Joint energy spectrum for the dissociation of Nitrogen by XUV+IR	106
7.13 KER distributions for the sidebands. The distribution for each sideband is normalized to its respective maximum	107
7.14 The two dissociation pathways associated with sideband 22.	107
7.15 Photoelectron spectrum as a function of XUV-IR delay for the electrons from vibrational levels v=3,4 and 5	108
7.16 Photoelectron spectrum as a function of XUV-IR delay for the electrons from vibrational levels v=6,7 and 8	109

7.17 Top: Left: two ideal sinewaves with a constant phase shift, Right: Amplitudes of the two waves plotted and fitted with an ellipse. Bot- tom: Left: Projections of sideband oscillations from a RABBIT mea- surement on argon, Right: Map of the amplitudes and the ellipse fit.	109
7.18 Amplitudes of the three possible pairs of sidebands for electrons from the $v=3$ state plotted and fitted with an ellipse	110
7.19 Schematic of the parallel(yellow) and perpendicular(green) transi- tions	111
7.20 Joint energy spectra for the parallel and perpendicular transitions .	112
7.21 Schematic of the modified beamline to perform "3-Sideband RAB- BIT" measurements, BBO - Beta Barium Borate crystal, BC - Beam collimator, DCM - Dichroic mirror. The rest of the labels have the same meaning as in Fig. 4.2	114
A.1 Simulated data to test the Legendre Polynomial fit	115
A.2 Beta Parameter fits for the $P_{3/2}$ electrons obtained by XUV ionization	116
A.3 Beta Parameter fits for the $P_{1/2}$ electrons obtained by XUV ionization	116
B.1 RABBIT measurement on Helium lasting about 18 hours. When divided over every 6 hours is taken separately, the oscillations are visible. When put together, the oscillations are smeared out.	117
B.2 Time delays extracted using the ellipse fit method	118
C.1 Table adapted from [32]	119

E Bibliography

- [1] Albert Einstein. Über einen die Erzeugung und Verwandlung des Lichtes betreffenden heuristischen Gesichtspunkt. (German) (On the production and transformation of light from a heuristic viewpoint). 322(6):132–148, 1905.
- [2] Ahmed H. Zewail. Laser femtochemistry. *Science*, 242(4886):1645–1653, 1988.
- [3] Jannika Lauth, Sachin Kinge, and Laurens D.A. Siebbeles. Ultrafast transient absorption and terahertz spectroscopy as tools to probe photoexcited states and dynamics in colloidal 2d nanostructures. *Zeitschrift für Physikalische Chemie*, 231(1):107–119, 2017.
- [4] Ferenc Krausz and Misha Ivanov. Attosecond physics. *Rev. Mod. Phys.*, 81:163–234, Feb 2009.
- [5] P. Hariharan and P. Hariharan. 3 - two-beam interferometers. In P. Hariharan and P. Hariharan, editors, *Basics of Interferometry (Second Edition)*, pages 13 – 22. Academic Press, Burlington, second edition edition, 2007.
- [6] M. Hentschel, R. Kienberger, Ch. Spielmann, G. A. Reider, N. Milosevic, T. Brabec, P. Corkum, U. Heinzmann, M. Drescher, and F. Krausz. Attosecond metrology. *Nature*, 414(6863):509–513, Nov 2001.
- [7] Edwin M. McMillan. A history of the synchrotron. *Physics Today*, 37(2):31–37, 1984.
- [8] G. Margaritondo and Primoz Rebernik Ribic. A simplified description of X-ray free-electron lasers. *Journal of Synchrotron Radiation*, 18(2):101–108, Mar 2011.
- [9] B.H. Bransden and C.J. Joachain. *Physics of Atoms and Molecules*. Prentice Hall, 2003.
- [10] Howard R. Reiss. *Foundations of the Strong-Field Approximation*, pages 1–31. Springer Berlin Heidelberg, Berlin, Heidelberg, 2008.
- [11] M. Lewenstein, Ph. Balcou, M. Yu. Ivanov, Anne L’Huillier, and P. B. Corkum. Theory of high-harmonic generation by low-frequency laser fields. *Phys. Rev. A*, 49:2117–2132, Mar 1994.

- [12] Howard R. Reiss. *Foundations of the Strong-Field Approximation*, pages 1–31. Springer Berlin Heidelberg, Berlin, Heidelberg, 2008.
- [13] G Mainfray and G Manus. Multiphoton ionization of atoms. *Reports on Progress in Physics*, 54(10):1333–1372, oct 1991.
- [14] P. Agostini, F. Fabre, G. Mainfray, G. Petite, and N. K. Rahman. Free-free transitions following six-photon ionization of xenon atoms. *Phys. Rev. Lett.*, 42:1127–1130, Apr 1979.
- [15] L.V. Keldysh. Ionization in the field of a strong electromagnetic wave. *Soviet Physics JETP*, 20.
- [16] P. B. Corkum. Plasma perspective on strong field multiphoton ionization. *Phys. Rev. Lett.*, 71:1994–1997, Sep 1993.
- [17] Mark J. Abel, Thomas Pfeifer, Phillip M. Nagel, Willem Boutu, M. Justine Bell, Colby P. Steiner, Daniel M. Neumark, and Stephen R. Leone. Isolated attosecond pulses from ionization gating of high-harmonic emission. *Chemical Physics*, 366(1):9–14, 2009. Attosecond Molecular Dynamics.
- [18] G. Sansone, E. Benedetti, F. Calegari, C. Vozzi, L. Avaldi, R. Flammini, L. Poletto, P. Villaresi, C. Altucci, R. Velotta, S. Stagira, S. De Silvestri, and M. Nisoli. Isolated single-cycle attosecond pulses. *Science*, 314(5798):443–446, 2006.
- [19] S. Eich, A. Stange, A.V. Carr, J. Urbancic, T. Popmintchev, M. Wiesemayer, K. Jansen, A. Ruffing, S. Jakobs, T. Rohwer, S. Hellmann, C. Chen, P. Matyba, L. Kipp, K. Rossnagel, M. Bauer, M.M. Murnane, H.C. Kapteyn, S. Mathias, and M. Aeschlimann. Time- and angle-resolved photoemission spectroscopy with optimized high-harmonic pulses using frequency-doubled ti:sapphire lasers. *Journal of Electron Spectroscopy and Related Phenomena*, 195:231–236, 2014.
- [20] Ram Gopal. *Electron Wave Packet Interferences in Ionization with Few-Cycle Laser Pulses and the Dissociative Photoionization of D2 with Ultrashort Extreme Ultraviolet Pulses*. PhD thesis, Ruprecht-Karls-Universität, Heidelberg, 2010.
- [21] P. B. Corkum. Plasma perspective on strong field multiphoton ionization. *Phys. Rev. Lett.*, 71:1994–1997, Sep 1993.
- [22] Jie Li, Jian Lu, Andrew Chew, Seunghwoi Han, Jialin Li, Yi Wu, He Wang, Shambhu Ghimire, and Zenghu Chang. Attosecond science based on high harmonic generation from gases and solids. *Nature Communications*, 11(1):2748, Jun 2020.

- [23] Jan Metje, Mario Borgwardt, Alexandre Mogilevski, Alexander Kothe, Nicholas Engel, Martin Wilke, Ruba Al-Obaidi, Daniel Tolksdorf, Alexander Firsov, Maria Brzhezinskaya, Alexei Erko, Igor Yu. Kiyan, and Emad F. Aziz. Monochromatization of femtosecond xuv light pulses with the use of reflection zone plates. *Opt. Express*, 22(9):10747–10760, May 2014.
- [24] Fabio Frassetto, Cephise Cacho, Chris A. Froud, I.C. Edmund Turcu, Paolo Villoresi, Will A. Bryan, Emma Springate, and Luca Poletto. Single-grating monochromator for extreme-ultraviolet ultrashort pulses. *Opt. Express*, 19(20):19169–19181, Sep 2011.
- [25] Tenio Popmintchev, Ming-Chang Chen, Alon Bahabad, Michael Gerrity, Pavel Sidorenko, Oren Cohen, Ivan P. Christov, Margaret M. Murnane, and Henry C. Kapteyn. Phase matching of high harmonic generation in the soft and hard x-ray regions of the spectrum. *Proceedings of the National Academy of Sciences*, 106(26):10516–10521, 2009.
- [26] Ph. Balcou and Anne L’Huillier. Phase-matching effects in strong-field harmonic generation. *Phys. Rev. A*, 47:1447–1459, Feb 1993.
- [27] A. Rubinowicz. On the anomalous propagation of phase in the focus. *Phys. Rev.*, 54:931–936, Dec 1938.
- [28] Jan Rothhardt, Steffen Hädrich, Stefan Demmler, Manuel Krebs, Stephan Fritzsche, Jens Limpert, and Andreas Tünnermann. Enhancing the macroscopic yield of narrow-band high-order harmonic generation by fano resonances. *Phys. Rev. Lett.*, 112:233002, Jun 2014.
- [29] M. Born and R. Oppenheimer. Zur quantentheorie der moleküle. *Annalen der Physik*, 389(20):457–484, 1927.
- [30] Ingolf V. Hertel and Claus-Peter Schulz. *Diatom Molecules*, pages 135–229. Springer Berlin Heidelberg, Berlin, Heidelberg, 2015.
- [31] Gordon H. Dunn. Anisotropies in angular distributions of molecular dissociation products. *Phys. Rev. Lett.*, 8:62–64, Jan 1962.
- [32] Farshad Shobeiry. *Attosecond Electron-Nuclear Dynamics in Photodissociation of H₂ and D₂*. PhD thesis, Ruprecht-Karls-Universität, Heidelberg, 2021.
- [33] J. Franck and E. G. Dymond. Elementary processes of photochemical reactions. *Trans. Faraday Soc.*, 21:536–542, 1926.
- [34] Edward Condon. A theory of intensity distribution in band systems. *Phys. Rev.*, 28:1182–1201, Dec 1926.

- [35] Franck-condon principle in vibronic transitions. <http://demonstrations.wolfram.com/FranckCondonPrincipleInVibronicTransitions/>. Accessed: 2010-09-30.
- [36] Ingolf V. Hertel and Claus-Peter Schulz. *Diatom Molecules*, pages 135–229. Springer Berlin Heidelberg, Berlin, Heidelberg, 2015.
- [37] J. A. Armstrong. Measurement of picosecond laser pulse widths. *Applied Physics Letters*, 10(1):16–18, 1967.
- [38] Franco Quercioli, Bruno Tiribilli, Massimo Vassalli, and Francesca Sbrana. Autocorrelator designs for nonlinear optical microscopy. *Optical Engineering*, 45(6):064303, 2006.
- [39] Miguel Miranda, Cord L. Arnold, Thomas Fordell, Francisco Silva, Benjamín Alonso, Rosa Weigand, Anne L’Huillier, and Helder Crespo. Characterization of broadband few-cycle laser pulses with the d-scan technique. *Opt. Express*, 20(17):18732–18743, Aug 2012.
- [40] Rick Trebino, Kenneth W. DeLong, David N. Fittinghoff, John N. Sweetser, Marco A. Krumbügel, Bruce A. Richman, and Daniel J. Kane. Measuring ultrashort laser pulses in the time-frequency domain using frequency-resolved optical gating. *Review of Scientific Instruments*, 68(9):3277–3295, 1997.
- [41] C. Iaconis and I.A. Walmsley. Self-referencing spectral interferometry for measuring ultrashort optical pulses. *IEEE Journal of Quantum Electronics*, 35(4):501–509, 1999.
- [42] Peter Baum and Eberhard Riedle. Design and calibration of zero-additional-phase spider. *J. Opt. Soc. Am. B*, 22(9):1875–1883, Sep 2005.
- [43] P. M. Paul, E. S. Toma, P. Breger, G. Mullot, F. Augé, Ph. Balcou, H. G. Muller, and P. Agostini. Observation of a train of attosecond pulses from high harmonic generation. *Science*, 292(5522):1689–1692, 2001.
- [44] Vladislav S. Yakovlev, Ferdinand Bammer, and Armin Scrinzi. Attosecond streaking measurements. *Journal of Modern Optics*, 52(2-3):395–410, 2005.
- [45] L. Cattaneo, J. Vos, M. Lucchini, L. Gallmann, C. Cirelli, and U. Keller. Comparison of attosecond streaking and rabbitt. *Opt. Express*, 24(25):29060–29076, Dec 2016.
- [46] Álvaro Jiménez Galán, Luca Argenti, and Fernando Martín. The soft-photon approximation in infrared-laser-assisted atomic ionization by extreme-ultraviolet attosecond-pulse trains. *New Journal of Physics*, 15(11):113009, nov 2013.

- [47] K. Varjú, Y. Mairesse, P. Agostini, P. Breger, B. Carré, L. J. Frasinski, E. Gustafsson, P. Johnsson, J. Mauritsson, H. Merdji, P. Monchicourt, A. L’Huillier, and P. Salières. Reconstruction of attosecond pulse trains using an adiabatic phase expansion. *Phys. Rev. Lett.*, 95:243901, Dec 2005.
- [48] D. Guénöt, K. Klünder, C. L. Arnold, D. Kroon, J. M. Dahlström, M. Miranda, T. Fordell, M. Gisselbrecht, P. Johnsson, J. Mauritsson, E. Lindroth, A. Maquet, R. Taïeb, A. L’Huillier, and A. S. Kheifets. Photoemission-time-delay measurements and calculations close to the 3s-ionization-cross-section minimum in ar. *Phys. Rev. A*, 85:053424, May 2012.
- [49] M. Isinger, R. J. Squibb, D. Busto, S. Zhong, A. Harth, D. Kroon, S. Nandi, C. L. Arnold, M. Miranda, J. M. Dahlström, E. Lindroth, R. Feifel, M. Gisselbrecht, and A. L’Huillier. Photoionization in the time and frequency domain. *Science*, 358(6365):893–896, 2017.
- [50] L. Cattaneo, J. Vos, R. Y. Bello, A. Palacios, S. Heuser, L. Pedrelli, M. Lucchini, C. Cirelli, F. Martín, and U. Keller. Attosecond coupled electron and nuclear dynamics in dissociative ionization of h₂. *Nature Physics*, 14(7):733–738, Jul 2018.
- [51] J. Vos, L. Cattaneo, S. Patchkovskii, T. Zimmermann, C. Cirelli, M. Lucchini, A. Kheifets, A. S. Landsman, and U. Keller. Orientation-dependent stereo wigner time delay and electron localization in a small molecule. *Science*, 360(6395):1326–1330, 2018.
- [52] J M Dahlström, A L’Huillier, and A Maquet. Introduction to attosecond delays in photoionization. *Journal of Physics B: Atomic, Molecular and Optical Physics*, 45(18):183001, aug 2012.
- [53] S. Kazamias and Ph. Balcou. Intrinsic chirp of attosecond pulses: Single-atom model versus experiment. *Phys. Rev. A*, 69:063416, Jun 2004.
- [54] Eugene P. Wigner. Lower limit for the energy derivative of the scattering phase shift. *Phys. Rev.*, 98:145–147, Apr 1955.
- [55] P. C. Deshmukh and Sourav Banerjee. Time delay in atomic and molecular collisions and photoionisation/photodetachment. *International Reviews in Physical Chemistry*, 40(1):127–153, 2021.
- [56] Kenneth. Levenberg. A method for the solution of certain non-linear problems in least squares. *Quart. Appl. Math.*, 2:164–168, 1944.
- [57] Donald W. Marquardt. An algorithm for least-squares estimation of nonlinear parameters. *Journal of the Society for Industrial and Applied Mathematics*, 11(2):431–441, 1963.

- [58] M. Swoboda, J. M. Dahlström, T. Ruchon, P. Johnsson, J. Mauritsson, A. L’Huillier, and K. J. Schafer. Intensity dependence of laser-assisted attosecond photoionization spectra. *Laser Physics*, 19(8):1591–1599, Aug 2009.
- [59] Martin Huppert. *Actively-Stabilized Attosecond Beamline and Its Application to Attosecond Dynamics in Atoms, Molecules, and Liquids*. Doctoral thesis, ETH Zurich, Zürich, 2016.
- [60] D Busto, L Barreau, M Isinger, M Turconi, C Alexandridi, A Harth, S Zhong, R J Squibb, D Kroon, S Plogmaker, M Miranda, Á Jiménez-Galán, L Argenti, C L Arnold, R Feifel, F Martín, M Gisselbrecht, A L’Huillier, and P Salières. 51(4):044002, jan 2018.
- [61] B. Carré, Y. Mairesse, P. Agostini, P. Breger, H. Merdji, P. Monchicourt, P. Salières, K. Varjú, P. Johnsson, J. Mauritsson, A. L’Huillier, E. Gustafsson, and L. J. Frasinski. *Characterization of Attosecond Pulse Trains*, pages 45–56. Springer New York, New York, NY, 2007.
- [62] L. Cattaneo, J. Vos, M. Lucchini, L. Gallmann, C. Cirelli, and U. Keller. Comparison of attosecond streaking and rabbitt. *Opt. Express*, 24(25):29060–29076, Dec 2016.
- [63] Caryn Palatchi, J M Dahlström, A S Kheifets, I A Ivanov, D M Canaday, P Agostini, and L F DiMauro. Atomic delay in helium, neon, argon and krypton. *Journal of Physics B: Atomic, Molecular and Optical Physics*, 47(24):245003, dec 2014.
- [64] K. Klünder, J. M. Dahlström, M. Gisselbrecht, T. Fordell, M. Swoboda, D. Guénot, P. Johnsson, J. Caillat, J. Mauritsson, A. Maquet, R. Taïeb, and A. L’Huillier. Probing single-photon ionization on the attosecond time scale. *Phys. Rev. Lett.*, 106:143002, Apr 2011.
- [65] Sebastian Heuser, Álvaro Jiménez Galán, Claudio Cirelli, Carlos Marante, Mazyar Sabbar, Robert Boge, Matteo Lucchini, Lukas Gallmann, Igor Ivanov, Anatoli S. Kheifets, J. Marcus Dahlström, Eva Lindroth, Luca Argenti, Fernando Martín, and Ursula Keller. Angular dependence of photoemission time delay in helium. *Phys. Rev. A*, 94:063409, Dec 2016.
- [66] Claudio Cirelli, Carlos Marante, Sebastian Heuser, C. L. M. Petersson, Álvaro Jiménez Galán, Luca Argenti, Shiyang Zhong, David Busto, Marcus Isinger, Saikat Nandi, Sylvain Maclot, Linnea Rading, Per Johnsson, Mathieu Gisselbrecht, Matteo Lucchini, Lukas Gallmann, J. Marcus Dahlström, Eva Lindroth, Anne L’Huillier, Fernando Martín, and Ursula Keller. Anisotropic photoemission time delays close to a fano resonance. *Nature Communications*, 9(1):955, Mar 2018.

- [67] Anne Harth, Nicolas Douguet, Klaus Bartschat, Robert Moshammer, and Thomas Pfeifer. Extracting phase information on continuum-continuum couplings. *Phys. Rev. A*, 99:023410, Feb 2019.
- [68] Divya Bharti, David Atri-Schuller, Gavin Menning, Kathryn R. Hamilton, Robert Moshammer, Thomas Pfeifer, Nicolas Douguet, Klaus Bartschat, and Anne Harth. Decomposition of the transition phase in multi-sideband schemes for reconstruction of attosecond beating by interference of two-photon transitions. *Phys. Rev. A*, 103:022834, Feb 2021.
- [69] Katalin Varjú, Per Johnsson, Rodrigo Lopez-Martens, Thomas Remetter, E. Gustafsson, Johan Mauritsson, Mette Gaarde, Kenneth Schafer, Christian Erny, I. Sola, Amelle Zair, Eric Constant, Eric Cormier, E. Mevel, and Anne L’Huillier. Experimental studies of attosecond pulse trains. *Laser Physics*, 15, 06 2005.
- [70] I. Orfanos, I. Makos, I. Lontos, E. Skantzakis, B. Förg, D. Charalambidis, and P. Tzallas. Attosecond pulse metrology. *APL Photonics*, 4(8):080901, 2019.
- [71] Mikhail Osolodkov, Federico J Furch, Felix Schell, Peter Šušnjar, Fabio Cavalcante, Carmen S Menoni, Claus P Schulz, Tobias Witting, and Marc J J Vrakking. Generation and characterisation of few-pulse attosecond pulse trains at 100 kHz repetition rate. *Journal of Physics B: Atomic, Molecular and Optical Physics*, 53(19):194003, sep 2020.
- [72] Michael Müller, Marco Kienel, Arno Klenke, Thomas Gottschall, Evgeny Shestaev, Marco Plötner, Jens Limpert, and Andreas Tünnermann. 1 kw 1 mj eight-channel ultrafast fiber laser. *Opt. Lett.*, 41(15):3439–3442, Aug 2016.
- [73] J. Limpert, A. Klenke, M. Kienel, S. Breitkopf, T. Eidam, S. Hädrich, C. Jau-regui, and A. Tünnermann. Performance scaling of ultrafast laser systems by coherent addition of femtosecond pulses. *IEEE Journal of Selected Topics in Quantum Electronics*, 20(5):268–277, Sep. 2014.
- [74] Steffen Hädrich, Arno Klenke, Armin Hoffmann, Tino Eidam, Thomas Gottschall, Jan Rothhardt, Jens Limpert, and Andreas Tünnermann. Non-linear compression to sub-30-fs, 0.5 mj pulses at 135 w of average power. *Opt. Lett.*, 38(19):3866–3869, Oct 2013.
- [75] H. A. Haus. Mode-locking of lasers. *IEEE Journal of Selected Topics in Quantum Electronics*, 6(6):1173–1185, 2000.
- [76] J. D. Kafka, T. Baer, and D. W. Hall. Mode-locked erbium-doped fiber laser with soliton pulse shaping. *Opt. Lett.*, 14(22):1269–1271, Nov 1989.

- [77] Steffen Hädrich, Marco Kienel, Michael Müller, Arno Klenke, Jan Rothhardt, Robert Klas, Thomas Gottschall, Tino Eidam, András Drozdy, Péter Jójárt, Zoltán Várallyay, Eric Cormier, Károly Osvay, Andreas Tünnermann, and Jens Limpert. Energetic sub-2-cycle laser with 216w average power. *Opt. Lett.*, 41(18):4332–4335, Sep 2016.
- [78] R. F. Cregan, B. J. Mangan, J. C. Knight, T. A. Birks, P. St. J. Russell, P. J. Roberts, and D. C. Allan. Single-mode photonic band gap guidance of light in air. *Science*, 285(5433):1537–1539, 1999.
- [79] R. R. Alfano and S. L. Shapiro. Observation of self-phase modulation and small-scale filaments in crystals and glasses. *Phys. Rev. Lett.*, 24:592–594, Mar 1970.
- [80] Robert Szipöcs, Kárpát Ferencz, Christian Spielmann, and Ferenc Krausz. Chirped multilayer coatings for broadband dispersion control in femtosecond lasers. *Opt. Lett.*, 19(3):201–203, Feb 1994.
- [81] N. Matuschek, F. X. Kartner, and U. Keller. Theory of double-chirped mirrors. *IEEE Journal of Selected Topics in Quantum Electronics*, 4(2):197–208, 1998.
- [82] F. W. Helbing, G. Steinmeyer, and U. Keller. Carrier-envelope offset phase-locking with attosecond timing jitter. *IEEE Journal of Selected Topics in Quantum Electronics*, 9(4):1030–1040, 2003.
- [83] G. Taubin. 3d rotations. *IEEE Computer Graphics and Applications*, 31(6):84–89, 2011.
- [84] Paul Kirkpatrick and A. V. Baez. Formation of optical images by x-rays. *J. Opt. Soc. Am.*, 38(9):766–774, Sep 1948.
- [85] Tim Salditt and Markus Osterhoff. *X-ray Focusing and Optics*, pages 71–124. Springer International Publishing, Cham, 2020.
- [86] J Ullrich, R Moshammer, R Dörner, O Jagutzki, V Mergel, H Schmidt-Böcking, and L Spielberger. Recoil-ion momentum spectroscopy. *Journal of Physics B: Atomic, Molecular and Optical Physics*, 30(13):2917–2974, jul 1997.
- [87] R. Moshammer, D. Fischer, and H. Kollmus. *Recoil-Ion Momentum Spectroscopy and “Reaction Microscopes”*, pages 33–58. Springer Berlin Heidelberg, Berlin, Heidelberg, 2003.
- [88] Philipp Cörlin. *Tracing ultra-fast molecular dynamics in O_2^+ and N_2^+ with XUV-IR pump-probe experiments*. PhD thesis, 2015.

- [89] J.H. PARRY. Helmholtz coils and coil design. In D.W. COLLINSON, K.M. CREER, and S.K. RUNCORN, editors, *Methods in Palaeomagnetism*, volume 3 of *Developments in Solid Earth Geophysics*, pages 551 – 567. Elsevier, 2013.
- [90] R.A. Cassanova and W.B. Stephenson. Expansion of a jet into a vacuum. *Symposium (International) on Combustion*, 11(1):577 – 587, 1967.
- [91] W. C. Wiley and I. H. McLaren. Time-of-flight mass spectrometer with improved resolution. *Review of Scientific Instruments*, 26(12):1150–1157, 1955.
- [92] Joseph Ladislas Wiza. Microchannel plate detectors. *Nuclear Instruments and Methods*, 162(1):587 – 601, 1979.
- [93] Arne Senftleben. *Kinematically complete study on electron impact ionisation of aligned hydrogen molecules*. PhD thesis, 2009.
- [94] David Kroon. *Attosecond interferometry: techniques and spectroscopy*. PhD thesis, Atomic Physics, Lund University, 2016.
- [95] Michael Chini, Hiroki Mashiko, He Wang, Shouyuan Chen, Chenxia Yun, Shane Scott, Steve Gilbertson, and Zenghu Chang. Delay control in attosecond pump-probe experiments. *Opt. Express*, 17(24):21459–21464, Nov 2009.
- [96] Mitsuo Takeda, Hideki Ina, and Seiji Kobayashi. Fourier-transform method of fringe-pattern analysis for computer-based topography and interferometry. *J. Opt. Soc. Am.*, 72(1):156–160, Jan 1982.
- [97] Kenneth H. Womack. Interferometric Phase Measurement Using Spatial Synchronous Detection. In James C. Wyant, editor, *Precision Surface Metrology*, volume 0429, pages 8 – 15. International Society for Optics and Photonics, SPIE, 1983.
- [98] Mitsuo Takeda, Hideki Ina, and Seiji Kobayashi. Fourier-transform method of fringe-pattern analysis for computer-based topography and interferometry. *J. Opt. Soc. Am.*, 72(1):156–160, Jan 1982.
- [99] J. Cooley, P. Lewis, and P. Welch. The finite fourier transform. *IEEE Transactions on Audio and Electroacoustics*, 17(2):77–85, 1969.
- [100] M. Isinger, D. Bustos, S. Mikaelsson, S. Zhong, C. Guo, P. Salières, C. L. Arnold, A. L’Huillier, and M. Gisselbrecht. Accuracy and precision of the rabbit technique. *Philosophical Transactions of the Royal Society A: Mathematical, Physical and Engineering Sciences*, 377(2145):20170475, 2019.

- [101] D. Kroon, D. Guénot, M. Kotur, E. Balogh, E. W. Larsen, C. M. Heyl, M. Miranda, M. Gisselbrecht, J. Mauritsson, P. Johnsson, K. Varjú, A. L'Huillier, and C. L. Arnold. Attosecond pulse walk-off in high-order harmonic generation. *Opt. Lett.*, 39(7):2218–2221, Apr 2014.
- [102] Robert W. Boyd. Intuitive explanation of the phase anomaly of focused light beams. *J. Opt. Soc. Am.*, 70(7):877–880, Jul 1980.
- [103] F. Schlaepfer, A. Ludwig, M. Lucchini, L. Kasmi, M. Volkov, L. Gallmann, and U. Keller. Gouy phase shift for annular beam profiles in attosecond experiments. *Opt. Express*, 25(4):3646–3655, Feb 2017.
- [104] D Bharti, H Srinivas, F Shobeyri, K R Hamilton, R Moshammer, T Pfeifer, K Bartschat, and A Harth. Multi-sideband rabbit in argon, 2022.
- [105] M. Baggash and H. Rottke. Phase differences in the photoemission from krypton in the fine-structure-split ionization channels $^2p_{3/2}$ and $^2p_{1/2}$. *Phys. Rev. A*, 92:013424, Jul 2015.
- [106] I. Jordan, M. Huppert, S. Pabst, A. S. Kheifets, D. Baykusheva, and H. J. Wörner. Spin-orbit delays in photoemission. *Phys. Rev. A*, 95:013404, Jan 2017.
- [107] Benjamin Doughty, Louis H. Haber, Christina Hackett, and Stephen R. Leone. Photoelectron angular distributions from autoionizing 4s14p66p1 states in atomic krypton probed with femtosecond time resolution. *The Journal of Chemical Physics*, 134(9):094307, 2011.
- [108] V. Loriot, L. Quintard, G. Karras, A. Marciniak, F. Catoire, M. Hervé, I. Compagnon, G. Renois-Predelus, B. Schindler, B. Concina, G. Celep, R. Brédy, C. Bordas, F. Lépine, and E. Constant. Time-resolved and spectrally resolved ionization with a single ultrashort xuv-ir beamline. *J. Opt. Soc. Am. B*, 35(4):A67–A74, Apr 2018.
- [109] André T. J. B. Eppink and David H. Parker. Velocity map imaging of ions and electrons using electrostatic lenses: Application in photoelectron and photofragment ion imaging of molecular oxygen. *Review of Scientific Instruments*, 68(9):3477–3484, 1997.
- [110] K. Codling and R. P. Madden. The absorption spectra of krypton and xenon in the wavelength range 330-600 Å. *Journal of research of the National Bureau of Standards. Section A, Physics and chemistry*, 76A(1):1–12, 1972.
- [111] Anatoli Kheifets, Ankur Mandal, Pranawa C. Deshmukh, Valeriy K. Dolmatov, David A. Keating, and Steven T. Manson. Relativistic calculations of angle-dependent photoemission time delay. *Phys. Rev. A*, 94:013423, Jul 2016.

- [112] Henke LBL. Filter transmission. https://henke.lbl.gov/optical_constants/filter2.html.
- [113] K. Codling and R. P. Madden. The absorption spectra of krypton and xenon in the wavelength range 330-600 Å. *Journal of research of the National Bureau of Standards. Section A, Physics and chemistry*, 76A(1):1–12, 1972. 34565834[pmid].
- [114] David L. Ederer. Cross-section profiles of resonances in the photoionization continuum of krypton and xenon (600-400 Å). *Phys. Rev. A*, 4:2263–2270, Dec 1971.
- [115] D. L. Ederer, A. C. Parr, J. B. West, D. Holland, and J. L. Dehmer. Measurement of the spin-orbit branching ratios and the angular asymmetry parameter in the region of the $4s4p^65p$ resonances in krypton and the $5s5p^66p$ resonances in xenon. *Phys. Rev. A*, 25:2006–2011, Apr 1982.
- [116] M Turconi, L Barreau, D Busto, M Isinger, C Alexandridi, A Harth, R J Squibb, D Kroon, C L Arnold, R Feifel, M Gisselbrecht, L Argenti, F Martín, A L ’Huillier, and P Salières. 53(18):184003, jul 2020.
- [117] K Codling and R P Madden. The absorption spectra of krypton and xenon in the wavelength range 330-600 Å. *J Res Natl Bur Stand A Phys Chem*, 76A(1):1–12, January 1972.
- [118] M Stener, P Decleva, and A Lisini. Density functional-time-dependent local density approximation calculations of autoionization resonances in noble gases. *Journal of Physics B: Atomic, Molecular and Optical Physics*, 28(23):4973, dec 1995.
- [119] Sebastian Heuser, Álvaro Jiménez Galán, Claudio Cirelli, Carlos Marante, Mazyar Sabbar, Robert Boge, Matteo Lucchini, Lukas Gallmann, Igor Ivanov, Anatoli S. Kheifets, J. Marcus Dahlström, Eva Lindroth, Luca Argenti, Fernando Martín, and Ursula Keller. Angular dependence of photoemission time delay in helium. *Phys. Rev. A*, 94:063409, Dec 2016.
- [120] J. A. R. Samson. Angular distributions of photoelectrons and partial photoionization cross-sections. *Philosophical Transactions of the Royal Society of London. Series A, Mathematical and Physical Sciences*, 268(1184):141–146, 1970.
- [121] J. Cooper and R. N. Zare. Angular distribution of photoelectrons. *The Journal of Chemical Physics*, 48(2):942–943, 1968.
- [122] Katharine L. Reid. Photoelectron angular distributions. *Annual Review of Physical Chemistry*, 54(1):397–424, 2003. PMID: 12574491.

- [123] D L Miller, J D Dow, R G Houlgate, G V Marr, and J B West. The photoionisation of krypton atoms: a comparison of pseudopotential calculations with experimental data for the 4p asymmetry parameter and cross section as a function of the energy of the ejected photoelectrons. *Journal of Physics B: Atomic and Molecular Physics*, 10(16):3205, nov 1977.
- [124] James A. R. Samson and J. L. Gardner. Resonances in the angular distribution of xenon photoelectrons. *Phys. Rev. Lett.*, 31:1327–1330, Nov 1973.
- [125] Dan Dill. Resonances in photoelectron angular distributions. *Phys. Rev. A*, 7:1976–1987, Jun 1973.
- [126] Jaco Fuchs, Nicolas Douguet, Stefan Donsa, Fernando Martin, Joachim Burgdörfer, Luca Argenti, Laura Cattaneo, and Ursula Keller. Time delays from one-photon transitions in the continuum. *Optica*, 7(2):154–161, Feb 2020.
- [127] Wenyu Jiang, Gregory S. J. Armstrong, Jihong Tong, Yidan Xu, Zitan Zuo, Junjie Qiang, Peifen Lu, Daniel D. A. Clarke, Jakub Benda, Avner Fleischer, Hongcheng Ni, Kiyoshi Ueda, Hugo W. van der Hart, Andrew C. Brown, Xiaochun Gong, and Jian Wu. Atomic partial wave meter by attosecond coincidence metrology. *Nature Communications*, 13(1):5072, Aug 2022.
- [128] E. Keshavarz, H. Farrokhpour, H. Sabzyan, Z. Noorisafa, A. Kivimäki, and R. Richter. Core photoionization of the argon dimer in the photon-energy range of 255–340 ev studied by a photoelectron-photoion-photoion coincidence technique. *Phys. Rev. A*, 89:053409, May 2014.
- [129] P. M. Dehmer. Photoionization of ar₂ at high resolution. *The Journal of Chemical Physics*, 76(3):1263–1272, 1982.
- [130] Tomoya Mizuno, Philipp Cörlin, Tsveta Miteva, Kirill Gokhberg, Alexander Kuleff, Lorenz S. Cederbaum, Thomas Pfeifer, Andreas Fischer, and Robert Moshammer. Time-resolved observation of interatomic excitation-energy transfer in argon dimers. *The Journal of Chemical Physics*, 146(10):104305, 2017.
- [131] Georg Schmid, Kirsten Schnorr, Sven Augustin, Severin Meister, Hannes Lindenblatt, Florian Trost, Yifan Liu, Tsveta Miteva, Mathieu Gisselbrecht, Stefan Düsterer, Harald Redlin, Rolf Treusch, Kirill Gokhberg, Alexander I. Kuleff, Lorenz S. Cederbaum, Claus Dieter Schröter, Thomas Pfeifer, and Robert Moshammer. Tracing charge transfer in argon dimers by xuv-pump ir-probe experiments at flash. *The Journal of Chemical Physics*, 151(8):084314, 2019.

- [132] Rafael Tadmor. The london-van der waals interaction energy between objects of various geometries. *Journal of Physics: Condensed Matter*, 13(9):L195, mar 2001.
- [133] Giovanni Sanna and Giuseppe Tomassetti. *Introduction to Molecular Beams Gas Dynamics*. PUBLISHED BY IMPERIAL COLLEGE PRESS AND DISTRIBUTED BY WORLD SCIENTIFIC PUBLISHING CO., 2005.
- [134] F. London. Zur theorie und systematik der molekularkräfte. *Zeitschrift für Physik*, 63(3):245–279, Mar 1930.
- [135] J E Lennard-Jones. Cohesion. *Proceedings of the Physical Society*, 43(5):461–482, sep 1931.
- [136] Petr Slaviček, René Kalus, Petr Paška, Iva Odváriková, Pavel Hobza, and Anatol Malijevský. State-of-the-art correlated ab initio potential energy curves for heavy rare gas dimers: Ar₂, kr₂, and xe₂. *The Journal of Chemical Physics*, 119(4):2102–2119, 2003.
- [137] Z Ansari, M Böttcher, B Manschwartus, H Rottke, W Sandner, A Verhoef, M Lezius, G G Paulus, A Saenz, and D B Milošević. Interference in strong-field ionization of a two-centre atomic system. *New Journal of Physics*, 10(9):093027, sep 2008.
- [138] Anton von Veltheim. *Noble gas dimers in strong laser fields*. Doctoral thesis, Technische Universität Berlin, Fakultät II - Mathematik und Naturwissenschaften, Berlin, 2015.
- [139] P. M. Dehmer and J. L. Dehmer. Photoelectron spectra of ar₂ and kr₂ and dissociation energies of the rare gas dimer ions. *The Journal of Chemical Physics*, 69(1):125–133, 1978.
- [140] T. Pradeep, B. Niu, and D. A. Shirley. Photoelectron spectroscopy of rare gas dimers revisited: vibrationally resolved photoelectron spectrum of argon dimer. *The Journal of Chemical Physics*, 98(7):5269–5275, 1993.
- [141] T.-K. HA, P. RUPPER, A. WÜEST, and F. MERKT. The lowest electronic states of ne₂ +, ar₂ + and kr₂ +: comparison of theory and experiment. *Molecular Physics*, 101(6):827–838, 2003.
- [142] Willard R. Wadt. The electronic states of ar+2, kr+2, xe+2. i. potential curves with and without spin-orbit coupling. *The Journal of Chemical Physics*, 68(2):402–414, 1978.
- [143] Saijoscha Heck, Meng Han, Denis Jelovina, Jia-Bao Ji, Conaill Perry, Xiaochun Gong, Robert Lucchese, Kiyoshi Ueda, and Hans Jakob Wörner. Two-center interference in the photoionization delays of kr₂. *Phys. Rev. Lett.*, 129:133002, Sep 2022.

- [144] Eugen Illenberger and Jacques Momigny. *Energy Balance in the Dissociation Processes of Molecular Ions*, pages 141–169. Steinkopff, Heidelberg, 1992.
- [145] Thomas Pfluger. *Electron Impact Ionization Studies of Small Rare Gas Clusters*. PhD thesis, Ruprecht-Karls-Universität, Heidelberg, 2012.
- [146] L. S. Cederbaum, J. Zobeley, and F. Tarantelli. Giant intermolecular decay and fragmentation of clusters. *Phys. Rev. Lett.*, 79:4778–4781, Dec 1997.
- [147] Olivier Hardouin Duparc. Pierre auger – lise meitner: Comparative contributions to the auger effect. *International Journal of Materials Research*, 100(9):1162–1166, 2009.
- [148] F. Légaré, Kevin F. Lee, I. V. Litvinyuk, P. W. Dooley, S. S. Wesolowski, P. R. Bunker, P. Dombi, F. Krausz, A. D. Bandrauk, D. M. Villeneuve, and P. B. Corkum. Laser coulomb-explosion imaging of small molecules. *Phys. Rev. A*, 71:013415, Jan 2005.
- [149] Kirsten Schnorr. *Data Analysis*, pages 83–97. Springer International Publishing, Cham, 2015.
- [150] Maksim Kunitski, Nicolas Eicke, Pia Huber, Jonas Köhler, Stefan Zeller, Jörg Voigtsberger, Nikolai Schlott, Kevin Henrichs, Hendrik Sann, Florian Trinter, Lothar Ph. H. Schmidt, Anton Kalinin, Markus S. Schöffler, Till Jahnke, Manfred Lein, and Reinhard Dörner. Double-slit photoelectron interference in strong-field ionization of the neon dimer. *Nature Communications*, 10(1):1, Jan 2019.
- [151] A. Trabattoni, M. Klinker, J. González-Vázquez, C. Liu, G. Sansone, R. Linguerri, M. Hochlaf, J. Klei, M. J. J. Vrakking, F. Martín, M. Nisoli, and F. Calegari. Mapping the dissociative ionization dynamics of molecular nitrogen with attosecond time resolution. *Phys. Rev. X*, 5:041053, Dec 2015.
- [152] Daniel Strasser, Louis H. Haber, Benjamin Doughty, and Stephen R. Leone. Ultrafast predissociation of superexcited nitrogen molecules. *Molecular Physics*, 106(2-4):275–280, 2008.
- [153] A. Trabattoni, M. Klinker, J. González-Vázquez, C. Liu, G. Sansone, R. Linguerri, M. Hochlaf, J. Klei, M. J. J. Vrakking, F. Martín, M. Nisoli, and F. Calegari. Mapping the dissociative ionization dynamics of molecular nitrogen with attosecond time resolution. *Phys. Rev. X*, 5:041053, Dec 2015.
- [154] S. Nandi, E. Plésiat, S. Zhong, A. Palacios, D. Busto, M. Isinger, L. Neorićić, C. L. Arnold, R. J. Squibb, R. Feifel, P. Decleva, A. L’Huillier, F. Martín, and M. Gisselbrecht. Attosecond timing of electron emission from a molecular shape resonance. *Science Advances*, 6(31):eaba7762, 2020.

- [155] Pamela R. Woodruff, G. V. Marr, and George William Series. The photoelectron spectrum of n₂, and partial cross sections as a function of photon energy from 16 to 40 ev. *Proceedings of the Royal Society of London. A. Mathematical and Physical Sciences*, 358(1692):87–103, 1977.
- [156] Tomohiro Aoto, Kenji Ito, Yasumasa Hikosaka, Akihiro Shibasaki, Ryo Hirayama, Norifumi Yamamono, and Eisaku Miyoshi. Inner-valence states of n₂⁺ and the dissociation dynamics studied by threshold photoelectron spectroscopy and configuration interaction calculation. *The Journal of Chemical Physics*, 124(23):234306, 2006.
- [157] T. Ayari, M. Desouter-Lecomte, R. Linguerri, G. A. Garcia, L. Nahon, A. Ben Houria, H. Ghalila, R. Ben Said, and M. Hochlaf. State-to-state dissociative photoionization of molecular nitrogen: the full story. *Advances in Physics: X*, 5(1):1831955, 2020.
- [158] P. Baltzer, M. Larsson, L. Karlsson, B. Wannberg, and M. Carlsson Göthe. Inner-valence states of n₂⁺ studied by uv photoelectron spectroscopy and configuration-interaction calculations. *Phys. Rev. A*, 46:5545–5553, Nov 1992.
- [159] A.L. Roche and Joel Tellinghuisen. Predissociation and perturbations in the c2 u + state of n₂ + from interaction with the b2 u + state. *Molecular Physics*, 38(1):129–143, 1979.
- [160] Michael D. Morse. Predissociation measurements of bond dissociation energies. *Accounts of Chemical Research*, 52(1):119–126, 2019.
- [161] R.M. Herman and A. Asgharian. Theory of energy shifts associated with deviations from born-oppenheimer behavior in 1-state diatomic molecules. *Journal of Molecular Spectroscopy*, 19(1):305–324, 1966.
- [162] Martin Eckstein. *Investigation of Ultrafast Electronic and Nuclear Dynamics in Molecular Nitrogen using an XUV Time Delay Compensating Monochromator*. Dissertation, 2015.
- [163] L. Cattaneo, J. Vos, R. Y. Bello, A. Palacios, S. Heuser, L. Pedrelli, M. Lucchini, C. Cirelli, F. Martín, and U. Keller. Attosecond coupled electron and nuclear dynamics in dissociative ionization of h₂. *Nature Physics*, 14(7):733–738, Jul 2018.
- [164] Constantin Krüger, Jaco Fuchs, Laura Cattaneo, and Ursula Keller. Attosecond resolution from free running interferometric measurements. *Opt. Express*, 28(9):12862–12871, Apr 2020.
- [165] Christian Neidel. *Attosecond time-resolved experiments - towards biomolecules*. Dissertation, 2017.

- [166] Tomoya Okino, Yusuke Furukawa, Yasuo Nabekawa, Shungo Miyabe, A. Amani Eilanlou, Eiji J. Takahashi, Kaoru Yamanouchi, and Katsumi Midorikawa. Direct observation of an attosecond electron wave packet in a nitrogen molecule. *Science Advances*, 1(8):e1500356, 2015.
- [167] D. Bharti, H. Srinivas, F. Shobeyri, K. R. Hamilton, R. Moshammer, T. Pfeifer, K. Bartschat, and A. Harth. Multisideband interference structures observed via high-order photon-induced continuum-continuum transitions in argon. *Phys. Rev. A*, 107:022801, Feb 2023.

- First and foremost - Robert and Thomas for supervising my work as well as supporting me in every project with extremely valuable inputs.
- Anne - for being a pillar of support and encouraging me to always try solving challenging problems and for the many mini-lectures on laser physics.
- Siva - for introducing me to the exciting world of experimental atomic physics and helping me join the group at MPIK for a PhD as well as being a scientific and a personal mentor.
- Prof. Andre Butz and Prof. Maurits Havercort - for kindly agreeing to be a part of the examination committee
- Farshad - for teaching and training me with the laboratory methods and the design and assembly of the attosecond beamline.
- Divya - for the great time working together in the lab and discussions on the theory behind the RABBIT technique as well proof-reading parts of this thesis.
- Denhi and Deepthy for being great friends and giving good company during outings and not to mention proofreading parts of the thesis.
-

Erklärung:

Ich versichere, dass ich diese Arbeit selbstständig verfasst habe und keine anderen als die angegebenen Quellen und Hilfsmittel benutzt habe.

I hereby certify, that this thesis is entirely my own original work except where indicated otherwise.

Heidelberg, den (Datum)